## NATIONAL & INTERNATIONAL SCIENTIFIC EVENTS

8th World Congress on Engineering and Technology (CET 2021)

Venue: The Grand Dynasty Culture Hotel
Location: Xi'an, China

Begins: October 22, 2021
Ends: October 24, 2021

42nd Ibero-Latin-American Congress on Computational Methods in Engineering (XLII CILAMCE)

Venue: Virtual Environment
Location: Rio de Janeiro, Brazil

Begins: November 09, 2021
Ends: November 12, 2021

IEEE 40th International Conference on Consumer Electronics

Venue: Tuscany Suites and Casino
Location: Las Vegas, USA

Begins: January 07, 2022
Ends: January 09, 2022

The 35th International Conference on Micro Electro Mechanical Systems

Venue: Tokyo International Forum
Location: Tokyo, Japan

Begins: January 09, 2022
Ends: January 13, 2022

12nd International Conference on Power Energy and Electrical Engineering (CPEEE 2022)

Venue: Biwako-Kusatsu Campus of Ritsumeikan University
Location: Shiga, Japan

Begins: February 25, 2022
Ends: February 27, 2022

16th International Conference on Martensitic Transformation (ICOMAT 2022)

Venue: Ramada Plaza Jeju Hotel
Location: Jeju, Korea

Begins: March 13, 2022
Ends: March 18, 2022

16th European Conference on Antennas and Propagation (EuCAP 2022)

Venue: IFEMA Palacio Municipal
Location: Madrid, Spain

Begins: March 27, 2022
Ends: April 01, 2022

27th International Conference on Database Systems for Advanced Applications (DASFAA-2022)

Venue: Online Conference
Location: Hyderabad, India

Begins: April 11, 2022
Ends: April 14, 2022

20th International Conference on Soil Mechanics and Geotechnical Engineering (ICSMGE 2022)

Venue: International Convention Centre Sydney
Location: Sydney, Australia

Begins: May 01, 2022
Ends: May 05, 2022

The 31st IEEE International Symposium on Industrial Electronics (IEEE ISIE 2022)

Venue: Dena'ina Center/Egan Center
Location: Alaska, USA

Begins: June 01, 2022
Ends: June 03, 2022

8th European Congress on Computational Methods in Applied Sciences and Engineering

Venue: Norway Convention Center
Location: Oslo, Norway

Begins: June 05, 2022
Ends: June 09, 2022

39th IAHR World Congress

Venue: IAHR World Congress
Location: Granada, Spain

Begins: June 19, 2022
Ends: June 24, 2022

Abstracted & Indexed in:
TR Dizin Mühendislik ve Temel Bilimler Veri Tabanı | CrossRef | Google Scholar | MIP Database | StuartxChange | ResearchBib | Scientific Indexing Services (SIS)

HITTITE

HJSE Official Journal of Hitit University Volume 8, Issue 3, 2021 dergipark.org.tr/en/pub/hjse

HİTİT UNIVERSITY

ISSN 2148-4171

# JOURNAL OF SCIENCE & ENGINEERING
# HITTITE

Volume 8, Issue 3, 2021

dergipark.org.tr/en/pub/hjse

HJSE Official Journal of Hitit University Volume 8, Issue 3, 2021 dergipark.org.tr/en/pub/hjse

*Elderly Fall Detection and Fall Direction Detection via Various Machine Learning Algorithms Using Wearable Sensors* 197-205

Sitki Kocaoglu and Yilmaz Guven

In this study, a two-step fall detection and fall direction detection system has been developed by using a public dataset and by testing 5 different machine learning algorithms comparatively.

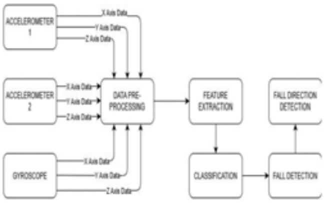

*A Review and Classification of Most Used MPPT Algorithms for Photovoltaic Systems* 207-220

Omer Faruk Tozlu and Huseyin Calik

In this study, the most used MPPT algorithms have been examined and compared by considering many parameters such as tracking speed, stability, and cost etc. and a new classification of these algorithms is proposed.

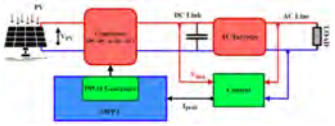

*An Experimental and Numerical Evaluation of Seal Strictness on Ball Bearing Performance* 221-231

Zafer Ozdemir, Osman Selim Turkbas and Kaan Sarigoz

Effect of rolling bearing seal strictness value on bearing performance was investigated experimentally and numerically in this study.

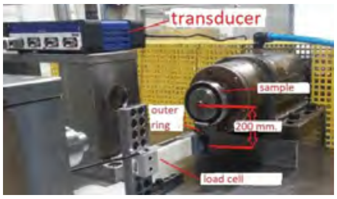

*Investigation of Shale Gas Reserves in The World and A Case Study for Electricity Production from Shale Gas in Turkey* 233-240

Erman Kadir Oztekin and Alperen Tozlu

In this study, global underground shale gas amount and recent discoveries as well as the potential shale gas areas in Turkey are presented.

*Influence of Stem-cell Size and Culture Media Flowing Modality on Cell's Fate within a Microchannel; a Numerical Analysis* 241-246

Daver Ali

In this study, the movement of stem cells through a microchannel was theoretically analysed using discrete phase computational fluid dynamics.

*Caffeic Acid Phenethyl Ester Alleviates Cryodamage To Lung Cancer Cells During Cryopreservation* 247-253

Ezgi Avsar Abdik

In the current study was to investigate the cryoprotective effects of CAPE on human lung cancer cell line, A549.

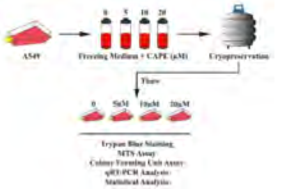

JOURNAL OF SCIENCE & ENGINEERING
HITTITE

*Evaluation of controlled hydroxychloroquine releasing performance from calcium-alginate beads* 255-263

Canan Armutcu and Sena Piskin

The aim of this study was to develop an effective controlled drug delivery system based on alginate beads for the treatment of autoimmune diseases such as Rheumatoid Arthritis (RA) and Systemic Lupus Erythematosus (SLE).

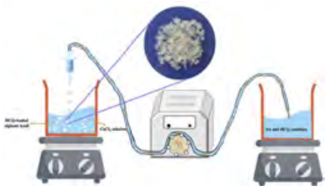

*Erratum to: Some Serum Oxidative Parameters in Normoglycemic Rats: Vascular Endothelial Growth Factor (VEGF) Application* 265-265

Kaan Kaltalioglu and Sule Coskun Cevher

After publication of this work [E1], it has come to our attention that there is a typographical error in the section of Material and Methods.

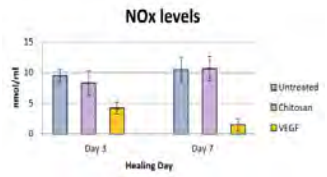

*Anti-helmintic Activity of Myrtus communis L. Fruit Ethanol Extract on Nematodes of Caenorhabditis elegans and The Determination of Possible Active Ingredients* 267-272

Hulya Ozpinar

In our study, C. elegans nematodes were used as an anti-helminthic model and by determining the anti-helmintic effect of Myrtus communis L. fruit, it was aimed to find the active ingredients with possible anti-helmintic effects by GC-MS analysis.

*Protection of Copper From Corrosion With Nicotinamide Inhibitor* 273-277

GuldenAsan

In this study, the environmentally friendly nicotinamide compound was used as an inhibitor to protect copper from corrosion.

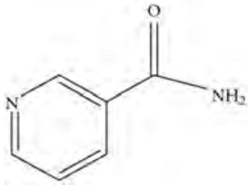

**Owner**
Prof. Dr. Ali Osman ÖZTÜRK on
behalf of Hitit University

**Editor-in-chief**
Prof. Dr. Ali KILIÇARSLAN

**Associate Editors**
Prof. Dr. D. Ali KÖSE
Assoc. Prof. Dr. Öncü AKYILDIZ

**Production**
Assoc. Prof. Dr. Kazım KÖSE
Res. Asst. Dr. Erhan ÇETİN
Res. Asst. Mustafa Reşit HABOĞLU
Res. Asst. Harun Emre KIRAN
Res. Asst. Ömer Faruk TOZLU
Lect. Tugrul YILDIRIM

**Editor's Office**
Tel: +90 364 227 45 33 / 12 36
Fax: +90 364 227 45 35
Email: alikilicarslan@hitit.edu.tr

**Subscription Service:**
Tel: +90 364 227 45 33 / 12 82
Fax: +90 364 227 45 35
Email: hjse@hitit.edu.tr

## EDITORIAL BOARD

| | |
|---|---|
| Prof. Dr. Iftikhar AHMAD | University of Malakand, Chakdara, Pakistan |
| Prof. Dr. Mike BECKETT | Bangor University, Bangor, United Kingdom |
| Prof. Dr. İbrahim DİNÇER | Uoit Ontario University, Ontario, Canada |
| Prof. Dr. Ali ELKAMEL | University of Waterloo, Ontario, Canada |
| Prof. Dr. Mohamad S QATU | Central Michigan University, Michigan, United States |
| Prof. Dr. Saffa RIFFAT | The University of Nottingham, United Kingdom |
| Prof. Dr. Thanos SALIFOGLOU | Aristotle University of Thessaloniki, Thessaloniki, Greece |
| Assoc. Prof. Dr. Yuehong SU | The University of Nottingham, United Kingdom |
| Dr. Wojciech NOGALA | Polish Academy of Sciences, Poland |
| Prof. Dr. Yusuf AYVAZ | Suleyman Demirel University, Turkey |
| Prof. Dr. Adil DENİZLİ | Hacettepe University, Turkey |
| Prof. Dr. Ali GENCER | Ankara University, Turkey |
| Prof. Dr. Metin GÜRÜ | Gazi University, Turkey |
| Prof. Dr. Murat HOŞÖZ | Kocaeli University, Turkey |
| Prof. Dr. Sadık KAKAÇ | TOBB University, Turkey |
| Prof. Dr. Tarık Ömer OĞURTANI | Middle East Technical University, Turkey |
| Prof. Dr. Ender SUVACI | Anadolu University, Turkey |
| Assoc. Prof. Dr. Ali TOPÇU | Hacettepe University, Turkey |
| Prof. Dr. Kazım Savaş BAHÇECİ | Hitit University, Turkey |
| Assoc. Prof. Dr. Cengiz BAYKASOĞLU | Hitit University, Turkey |
| Prof. Dr. Naki ÇOLAK | Hitit University, Turkey |
| Prof. Dr. Vedat DENİZ | Hitit University, Turkey |
| Prof. Dr. Hakan GÜNGÜNEŞ | Hitit University, Turkey |
| Prof. Dr. Bülent KABAK | Hitit University, Turkey |
| Prof. Dr. Ali KILIÇARSLAN | Hitit University, Turkey |
| Prof. Dr. Dursun Ali KÖSE | Hitit University, Turkey |
| Prof. Dr. İrfan KURTBAŞ | Hitit University, Turkey |
| Prof. Dr. İbrahim SÖNMEZ | Hitit University, Turkey |
| Assoc. Prof. Dr. Seyfi ŞEVİK | Hitit University, Turkey |
| Prof. Dr. Dilber Esra YILDIZ | Hitit University, Turkey |

# MASTHEAD

Journal Name : HITTITE JOURNAL OF SCIENCE AND ENGINEERING
Year : 2021
Managing Editor : Prof. Dr. Ali KILIÇARSLAN
Managing Office : Hitit University Faculty of Engineering
Managing Office Tel : +90 364 227 45 33 / 12 36
Publication Language : English
Publication Type : Peer Reviewed, Open Access, International Journal
Delivery Format : 4 times a year (quarterly)
Print ISSN : 2149-2123
Online ISSN : 2148-4171
Publisher Address : Hitit Üniversitesi Kuzey Kampüsü Çevre Yolu Bulvarı
19030 Çorum / TÜRKİYE
Publisher Tel : +90 364 227 45 33/1236

# EDITORIAL

*This new issue of Hittite Journal of Science and Engineering contains ten manuscripts from the disciplines of chemistry, molecular biology and genetics, bioengineering, medical engineering, mechanical engineering, electrical and electronics engineering. These manuscripts was first screened by Section Editors using plagiarism prevention software and then reviewed and corrected according to the reviewer's comments.*

*I would like to express my gratitude to all our authors and contributing reviewers of this issue. I would like to thank to the new President of Hitit University, Prof. Dr. Ali Osman Öztürk, for his support and interest in HJSE and also to the Section Editors of HJSE, namely Prof. Dr. Dursun Ali Kose and Assoc. Prof. Dr. Oncu Akyildiz, as well as our Production Editors Assoc. Prof. Dr. Kazim Kose, Mustafa Reşit Haboğlu, Dr. Erhan Çetin, Tugrul Yıldırım, Harun Emre Kıran and Ömer Faruk Tozlu for their invaluable efforts in making of the journal.*

*It's my pleasure to invite the researchers and scientists from all branches of science and engineering to join us by sending their best papers for publication in Hittite Journal of Science and Engineering.*

*Prof. Dr. Ali Kilicarslan*

*Editor-in-Chief*

Hittite Journal of Science and Engineering, 2021, 8 (3) 197–205
ISSN NUMBER: 2148–4171
DOI: 10.17350/HJSE19030000230

# Elderly Fall Detection and Fall Direction Detection via Various Machine Learning Algorithms Using Wearable Sensors

**Sıtkı Kocaoğlu**[1] **Yılmaz Güven**[2]
[1]Ankara Yildirim Beyazit University, Department of Biomedical Engineering, Ankara, Turkey
[2]Kirklareli University, Department of Electronic & Automation, Kirklareli, Turkey

***Article History:***
*Received: 2021/02/02*
*Accepted: 2021/07/02*
*Online: 2021/09/29*

***Correspondence to**: Sıtkı Kocaoğlu*
*Department of Biomedical Engineering,*
*Ankara Yıldırım Beyazıt University, Ankara, Turkey*
*Tel: +90 3129062309*
*E-Mail:sitki.kocaoglu@hotmail.com*

## ABSTRACT

The world population is aging rapidly. Some of elderly person live alone and it is observed that the elderly who live with their families frequently have to stay at home alone. Especially during the working hours of adult members of the family, elderly member stays alone. Falling while alone at home often results in fatal injuries and even death in elderly individuals. Fall detection systems can detect falls and provide emergency healthcare services in a short time. In this study, a two-step fall detection and fall direction detection system has been developed by using a public dataset with 5 different machine learning algorithms comparatively. If a fall is detected in the first stage, the second stage is started to determine the direction of the fall. In this way, the direction of fall can be determined for elderly individual to be used in future researches, and an early warning system that enables necessary measures such as opening an airbag in the direction of the fall can be developed. Thus, a gradual fall and its direction detection system has been developed by determining the best classifying algorithms. As a result, it has been determined that Ensemble Subspace k-Nearest Neighbor (ES k-NN) classifier performs a little more successful classification compared to other classifiers. The classification by using the test data which is corresponding to 30% of the total data that was never used during the training phase, has been performed 99.4% accuracy for fall detection, and 97.2% success has been achieved in determining the direction of falling.

**Keywords:**
Fall detection; Falling direction detection; Machine learning; Wearable sensors

## INTRODUCTION

As a result of the developments in the field of medicine, human life has been prolonged. For this reason, the ratio of elderly individuals to other individuals in the society is increasing day by day. According to the United Nations' World Population Ageing 2019 report, the world population is estimated to increase by 2 billion people and reach 9.7 billion by 2050(United Nations, 2019). According to the expectations of the World Health Organization (WHO), the number of individuals over 60 is estimated to exceed 2 billion in 2050 and the rate of deaths due to falls is estimated to increase from 28% to 42% (WHO, 2007; Chelli and Patzold, 2019). While falls of elderly people sometimes result in severe damage such as bone fracture, some falls do not cause any significant injury. The elderly person's health condition worsens as a result of the inability to get up without support after a long stay on the floor. For this reason, it is vital that the falls of elderly individuals must be detected while alone at home to provide necessary medical support. Fall detection systems are subjects of great interest for researchers since 2010. Fall detection systems can be examined in 3 main groups as; (i) Wearable Sensor Based Fall Detection Systems, (ii) Ambient Sensor and Image Processing Based Fall Detection Systems and (iii) Multimodal Fall Detection Systems (Kocaoglu, 2020). Wearable Sensor Based systems generally include accelerometers and gyroscopes in their structures. These wearables, which are connected to various parts of the elderly person's body, measure acceleration and angular velocity. Acceleration and angular velocity information collected within a certain period is processed by using various methods and it is determined whether the individual's instantaneous movement is a fall or Activity of Daily Living (ADL).

There are many studies in the literature that use the SisFall dataset to detect a fall. While some of these studies try to specifically determine the type of fall, some of them make a determination of whether there is a fall or no fall in binary. However, the important thing in daily life is to quickly detect a fall and to determine the direction of the fall and to take precautions against hitting the hard floor if possible. The main goal here is to perform fall detection and fall direction detection quickly and with high accuracy. In this study, first fall detection is performed, then the fall direction is determined if a fall is detected in first stage. This is first in the literature by using the SisFall dataset. Thus, protective measures such as deploying an airbag in the direction of fall can be developed in future studies.

The following parts of the article are structured as follows. In Chapter 2, previous studies using the SisFall dataset are reviewed. In Chapter 3, the dataset is introduced and the method used in this study is explained. In Chapter 4, the results of the study are examined. In Chapter 5, a conclusion is made.

## RELATED WORK

It appears that there are many Wearable Sensor Based Fall Detection Systems in the literature (Chen et al., 2005; Kang, Yoo and Kim, 2006; Srinivasan et al., 2007; Li et al., 2009; Delgado-Escaño et al., 2020; Kerdjidj et al., 2020; Nho, Lim and Kwon, 2020). Most of the studies in this group perform fall detection with very high accuracy. Studies in the Ambient Sensor and Image Processing Based Fall Detection Systems group usually detect falls by placing a camera in the elderly individual's room (Wu, 2000; Nait-Charif and McKenna, 2004; Han et al., 2013; Mastorakis and Makris, 2014; Daga, Ghatol and Thakare, 2018; Adhikari, 2019; Gupta et al., 2020). However, it is known that systems working with this method are rejected by elderly individuals. The reason for this is the violation of privacy and the fact that these systems can only work within a certain area and cannot detect falls that occur outside the building or in another room of the house. On the other hand, Multimodal Fall Detection Systems are methods that aim to increase accuracy by using information from both wearable sensors and cameras. (Nyan et al., 2006; de Assis Neto et al., 2019; Martinez-Villasenor, Ponce and Perez-Daniel, 2019). Fig. 1 shows the working structure of fall detection systems in general.

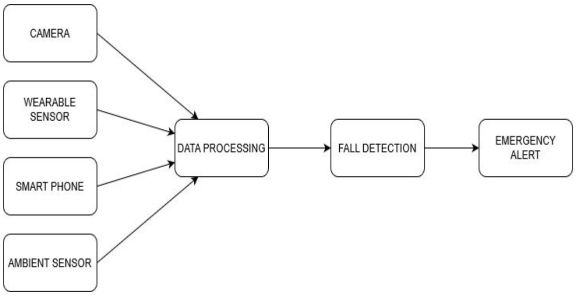

**Figure 1.** General block diagram of fall detection systems

To develop a fall detection system, collected data during past falls are needed. Since falls are very rare cases compared to ADLs, it is not possible to wait for real falls and record at the time of the fall. For this reason, data of artificial falls performed by the subjects are used during the development of fall detection systems. Although it is not possible to imitate real falls by the subjects, it is possible to obtain realistic results with this method. Most of the researchers present the fall data they collect during their studies for the use of other researchers as a public dataset. These public datasets differ in terms of the number of subjects, the number and variety of falling movements and ADLs, the number of repetitions of the movements and the sensor types. What is common to all of this dataset is that the fall experiments performed only by adult subjects. Since it is risky to perform a fall test with elderly subjects, there is no study that collects and shares fall data from individuals over the age of 65. Although there are differences between the fall dynamics of young people and elderly people, it is thought that this does not significantly affect the success of the system. The SisFall dataset shared publicly in 2017 is one of the most detailed datasets in the literature (Sucerquia, López and Vargas-Bonilla, 2017). This dataset was created with data from 2 accelerometers and 1 gyroscope. Most of the studies using this dataset do the fall recognition process as binary (fall/ADL) (Putra and Vesilo, 2018; Putra et al., 2018; Saleh and Le Bouquin Jeannès, 2018; Sucerquia, López and Vargas-Bonilla, 2018; Cho and Yoon, 2019; Saleh and Jeannes, 2019; Casilari, Lora- rivera and García-lagos, 2020; Han et al., 2020). Most studies used only accelerometer data. Among them, Yacchirema et al. used only 3 falling activities and 9 ADLs and made the classification in a way to determine the type of fall. In the study using Decision Tree (DT), an accuracy of about 92% was obtained (Yacchirema et al., 2018). In Liu et al.'s study, the effect of sampling rate on success was investigated and classification was made as binary fall/non-fall (Liu et al., 2018). Hussain et al. first classified the movements as binary fall/ADL, and if the result was fall, they tried to find out which type of fall it was. All fall types were included in this study, and the effects of sensor types were investigated by using them individually or together. As a result, the highest classification success was obtained using the Random Forest (RF) classifier when all sensors were used (Hussain et al., 2019). Some researchers used multiple datasets, trained using one dataset and tested by using the other one (Kruptizer et al., 2018; Delgado-Escaño et al., 2020).

In this study, 34 types of ADLs and falls are classified as binary using SisFall dataset. Then the direction of the fall is determined for the movements identified as falling. Thus, an approach suitable for obtaining information about how the elderly individual made falls and what their movements are before and after the fall is developed. Thus, a classifier is created that can be used in studies such as preventing falls, taking precautions and giving a warning in case of a fall possibility based on previous activities. The classification is performed with 5 different machine learning algorithms and the most successful classification results are obtained with ES k-NN classifier in both stages. In the classification using the 30% (testing) part of the data, which is not used in the training phase, the fall detection is performed with 99.4% accuracy, while the direction of the falls is detected correctly at a rate of 97.2%. These results coincide with the results of studies in the literature that detect falling binarily. As far as we know, this study is the first study in the literature that aims to determine the direction of falling and it does this with a high accuracy rate.

## METHODS

The proposed method in this study is a two-step method. First step is determining whether the activity is a falling or not. When the real-time application is started, the information received from the sensors will be processed in short window intervals and if it indicates a fall, the direction of the rapid fall will be determined. Thus, it will be possible to take a precaution for the falling elderly person. The block diagram of the method is given in Fig. 2.

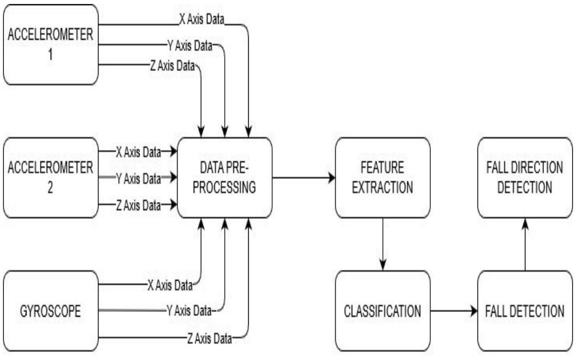

**Figure 2.** Block diagram of the system

### Dataset

In the literature, there are public datasets containing various sensor and camera data prepared by different researchers. It is seen that almost all of these datasets consist of artificial falls and ADLs performed by young subjects (Casilari, Santoyo-Ramón, & Cano-García, 2017; Riquelme, Espinoza, Rodenas, Minonzio, & Taramasco, 2019). The body dynamics of the elderly and young individuals show great differences during the activities. However, it is not possible to perform the fall experiments by elderly subjects. So, it is a necessity to use the data obtained from the younger subjects. Likewise, there are serious dynamic differences between the real falls that occur in daily life and the artificial falls performed by the subject who knows that he fakes a falling movement. However, it seems impossible to create a dataset consisting of spontaneous falls, as the frequency of falling spontaneously in daily life is not high. In the evaluation of a dataset to be used in the detection of falls under these conditions, it is necessary to pay attention to the following.

- Possible movements should be done by elderly people. The extremity movement speeds of the elderly and young people show great differences while doing their daily living activities. If the dataset is created with young subjects and the system is used on elderly individuals, the accuracy of fall detection will decrease.

- The type of movements should be diverse in a way that matches the daily life as much as possible. while creating the dataset, if the selected movements are not frequently used in daily life, the algorithm that gives good results in the computer environment may result erroneous inferences for real-life.

- The number of repetitions for the movements in the dataset should be high. As a result, the success of the created system is directly proportional to the quality of the dataset. The more diverse and multiple trials the dataset contains, the higher the classification success of the movements will be.

- In order to increase the success in terms of classification, the dataset should be balanced both as ADL/Fall and for each ADL and fall. Because a well-balanced training set eliminates bias of the classifier toward particular class due to over-representation or under-representation of input patterns belonging to those classes (Nath & Subbiah, 2018).

- The movements should be done by using various individuals in terms of gender, height and weight. Because the physiological structure of a person significantly affects the speed and acceleration of movement.

- It should be ensured that the subject is not affected of the negative physiological effects that may occur as a result of the fall, especially when falling movements are made, but to ensure this, the measures to be taken in the experimental area must be in a way that does not disturb the characteristics of the fall.

When the public datasets are examined under these conditions, it is seen that SisFall dataset is one of the most comprehensive datasets available in the literature. Sucerquia et al. introduced SisFall dataset with their publication in 2017 (Sucerquia, López and Vargas-Bonilla, 2017).

**Table 1.** Activities

| Code | Activity | Duration (s) |
|---|---|---|
| F01 | Fall forward while walking, caused by a slip | 15 |
| F02 | Fall backward while walking, caused by a slip | 15 |
| F03 | Lateral fall while walking, caused by a slip | 15 |
| F04 | Fall forward while walking, caused by a trip | 15 |
| F05 | Fall forward while jogging, caused by a trip | 15 |
| F06 | Vertical fall while walking, caused by fainting | 15 |
| F07 | Fall while walking with damping, caused by fainting | 15 |
| F08 | Fall forward when trying to get up | 15 |
| F09 | Lateral fall when trying to get up | 15 |
| F10 | Fall forward when trying to sit down | 15 |
| F11 | Fall backward when trying to sit down | 15 |
| F12 | Lateral fall when trying to sit down | 15 |
| F13 | Fall forward while sitting, caused by fainting | 15 |
| F14 | Fall backward while sitting, caused by fainting | 15 |
| F15 | Lateral fall while sitting, caused by fainting | 15 |
| D01 | Walking slowly | 100 |
| D02 | Walking quickly | 100 |
| D03 | Jogging slowly | 100 |
| D04 | Jogging quickly | 100 |
| D05 | Walking upstairs and downstairs slowly | 25 |
| D06 | Walking upstairs and downstairs quickly | 25 |
| D07 | Slowly sit and get up in a half-height chair | 12 |
| D08 | Quickly sit and get up in a half-height chair | 12 |
| D09 | Slowly sit and get up in a low-height chair | 12 |
| D10 | Quickly sit and get up in a low-height chair | 12 |
| D11 | Sitting, trying to get up, and collapse into a chair | 12 |
| D12 | Sitting, lying slowly, wait a moment, and sit again | 12 |
| D13 | Sitting, lying quickly, wait a moment, and sit again | 12 |
| D14 | Changing position while lying (back-lateral-back) | 12 |
| D15 | Standing, slowly bending at knees, and getting up | 12 |
| D16 | Standing, slowly bending w/o knees, and getting up | 12 |
| D17 | Standing, get into and get out of a car | 25 |
| D18 | Stumble while walking | 12 |
| D19 | Gently jump without falling (to reach a high object) | 12 |

A large number of researchers using this dataset have developed various methods and classifiers that detect the fall. Few articles have threshold-based fall detection as in Sucerquia et al. (Sucerquia, López and Vargas-Bonilla, 2018; Jung et al., 2020). In these studies, the fall detection was made binary as fall/ADL.

This dataset contains data from two 3-axis accelerometers and one 3-axis gyroscope. The dataset, which consists of 38 participants, consisting of young and old individuals, includes 15 different falling movements and 19 types of ADLs. It is seen that almost every movement was repeated 5 times by the participants. While creating the dataset, the sensor information was recorded with frequency of 200 Hz. The dataset content is shown in Table 1.

## Pre-processing

Pre-processing is an important step that directly affects the success of the classification. When the SisFall dataset is examined structurally, it is a smooth dataset that does not require much preprocessing. No noisy results were obtained thanks to low frequency data collection. In this study, only the activity duration was equalized in the preprocessing stage. All activities are divided into 12-second windows. Thus, activities such as walking and jogging were divided into parts and 8 separate samples were created from each trial.

## Feature Extraction

In the next step, feature extraction is applied to extract more meaningful data from raw data. Thus, better characterization of each activity is provided. While choosing the features, the literature was examined and, the features that were used more frequently in previous studies during fall detection were determined. By examining the features in terms of computational complexity, the ones with high contribution/computational cost ratio were preferred. In Table 2, these features are given with their explanations. Here, $\mu$ present the mean value, N presents the number of elements, x presents the $i^{th}$ element, $\sigma$ presents the standard deviation, s presents the sum, $g_2$presents the kurtosis, $g_1$presents the skewness and rms presents the root mean square. The features are extracted from each three axes of each three sensors, so that a total of 99 features for each observation are obtained.

Finally, the extracted features are brought to a common scale and normalized between -1 and 1. Thus, it was tried to take into account the small differences in the data depending on the used algorithm.

## Fall Detection

In general, the movement speed of the body of the individual increases suddenly during a fall. This situation makes it possible to detect the fall by creating strong changes on the accelerometer connected to the individual's body. However, there are also movements with velocity changes close to the falling state in ADLs. This confusion is the main shortcoming of fall detection systems that are intended to be made only with accelerometer data. Therefore, in this study, gyroscope sensor is used together with accelerometer in order to detect angular change.

During the fall detection phase, binary classification is made, observations are divided into two groups Fall

**Table 2.** Features

| Feature No | Feature | Equation/Definion | Feature No | Feature | Equation/Definion |
|---|---|---|---|---|---|
| 1 | Mean | $\mu = \frac{1}{N}\sum_{i=1}^{N} x_i$ | 7 | Minimum | Min. term of data |
| 2 | Standart deviation | $\sigma = \sqrt{\frac{1}{N}\sum_{i=1}^{N}(x_i - \mu)^2}$ | 8 | Kurtosis | $g_2 = \frac{\frac{1}{N}\sum_{i=1}^{N}(x_i - \mu)^4}{\frac{1}{N}\sum_{i=1}^{N}(x_i - \mu)^2}$ |
| 3 | Variance | $\sigma^2 = \frac{1}{N}\sum_{i=1}^{N}(x_i - \mu)^2$ | 9 | Skewness | $g_1 = \frac{\frac{1}{N}\sum_{i=1}^{N}(x_i - \mu)^3}{\frac{1}{N}\sum_{i=1}^{N}(x_i - \mu)^2}$ |
| 4 | Sum | $s = \sum_{i=1}^{N} x_i$ | 10 | Band power | Average power of data |
| 5 | Median | Midterm of data | 11 | Root mean square | $rms = \sqrt{\frac{1}{N}\sum_{i=1}^{N} x_i^2}$ |
| 6 | Maximum | Max. term of data | 12 | | |

(Class 1) and ADL (Class 0). Thus, 3271 observations for Class 1 and 2440 observations for Class 0 are obtained. Classification is made using five different machine learning algorithms; Support Vector Machine (SVM), k Nearest Neighbor (k-NN), DT, RF and ES k-NN.

An SVM algorithm tries to obtain the hyperplane that best distinguishes between classes. This hyperplane is achieved by obtaining the largest margin between the classes. SVM is a computer algorithm that learns by example to assign labels to objects. At its core, an SVM is a mathematical entity and an algorithm for maximizing a particular mathematical function relative to a particular collection of data. There are 4 basic concepts at the core of the SVM classification; (i) separating hyperplane, (ii) hyperplane with maximum margin, (iii) soft margin, and (iv) kernel function. The general term for a straight line in a high-dimensional space is a hyperplane, and thus the dividing hyperplane is essentially the line that separates the differently labeled instances. If we define the distance from the separating hyperplane to the nearest expression vector as the margin of the hyperplane, the SVM chooses the maximum margin that separates the hyperplane. Choosing this particular hyperplane maximizes SVM's ability to predict the correct classification of previously unseen samples. Of course, many real data sets cannot be separated so clearly. Intuitively, it is desirable that the SVM could deal with errors in the data by allowing several anomalous expression profiles to fall on the wrong side of the separation hyperplane. To handle such cases, the SVM algorithm needs to be modified by adding a "soft margin". Essentially, this allows some data points to travel along the margin of the separation hyperplane without affecting the final result. The problem is that a single point cannot separate the two classes and adding a soft margin won't help. The kernel function provides a solution to this problem by adding an additional dimension to the data. In essence, the kernel function is a mathematical trick that allows SVM to perform a "two-dimensional" classification of a set of original one-dimensional data. In general, a kernel function projects data from a low-dimensional space to a higher-dimensional space by squaring the sample (Noble, 2006).

K nearest neighbors (kNN) is an efficient lazy learning algorithm and has successfully been developed in real applications. It is an algorithm that classifies according to both the distance measure and the number of neighbors. kNN algorithm computes the distance between each training sample and test samples in the dataset and then returns k closest samples. Its time complexity is linearly and is guaranteed to find exact k nearest neighbors (Deng et al., 2016).

By its simplest description, decision tree analysis is a divide-and-conquer approach to classification and regression. Decision trees can be used to discover features and extract patterns in large databases that are important for discrimination and predictive modeling. A decision tree is constructed by recursively partitioning the feature space of the training set. The first cell of the decision tree is called the root. Each observation is labeled yes or no according to the situation at this root. There are nodes under the roots. The complexity of the model increases as the number of nodes increases. The leaves at the bottom of the decision trees give the classification result. The objective is to find a set of decision rules that naturally partition the feature space to provide an informative and robust hierarchical classification model (Myles et al., 2004).

Random Forest is an ensemble method, which constructs many decision trees that will be used to classify a new instance by the majority vote. Each decision tree node uses a subset of attributes randomly selected from the whole original set of attributes. Additionally, each tree uses a different bootstrap sample data in the same manner as bagging. A Random Tree is a tree drawn at random from a set of possible trees, with m random attributes at each node. The term "at random" means that each tree has an equal chance of being sampled. Random Trees can be efficiently generated, and the combination of large sets of Random Trees generally lead to accurate models (Oshiro et al., 2012).

ES-KNN is also ensemble classifier like RF. Its difference from RF is that it uses KNN as a classifier model. Despite its simplicity, k-NN gives competitive results and even outperforms other complex learning algorithms in some cases. However, k-NN is affected by non-informative features in the data, which are quite common in high-dimensional data. Subspace ensembles have the advantage of using less memory than ensembles with all estimators and can handle missing values. For this reason, it is expected that the classification success of the ES-kNN algorithm will increase, especially as the dataset grows (Psathas et al., 2020).

Undoubtedly, more training data is needed to obtain a classifier model with good performance. Therefore, except for some special cases (limited data set), it is desirable that the training data set be larger than the test dataset. In fact, there is no optimum split ratio. It is generally accepted in the literature to divide the data sets as 70-80% training and 20-30% testing. It was predicted that separating the training set by 60% would reduce the classifier performance by 70%. When we separate the training data set by 80%, the performance of the classifier model will increase, but the test data will not be able to represent a part of the training data. Apart from these, considering the training and evaluation costs, the data set was divided into 70% training and 30% testing.

Standard machine learning metrics are used for evaluation. Learning outcomes are included for each observation in one of the following categories:

True Positive (TP): There is actually a fall and the classifier detect it as a fall

True Negative (TN): Actually, it is not a fall and the classifier detect it as not-fall

False Positive (FP): There is no actual fall and the classifier has a false fall alarm.

False Negative (FN): There is actually a fall and the classifier has incorrectly detected it as a not-fall.

**Table 3.** Model evaluation metrics for machine learning

| *Feature No* | *Equation* |
|---|---|
| *Sensitivity* | $SE = \frac{TP}{TP+FN} x100$ |
| *Specificity* | $SP = \frac{TN}{TN+FP} x100$ |
| *Accuracy* | $ACC = \frac{TP+TN}{TP+TN+FP+FN} x100$ |
| *Precision* | $PRE = \frac{TP}{TP+FP} x100$ |
| *F1-Score* | $F1 = 2\,x \frac{PRE\,x\,SE}{PRE+SE}$ |

In order to measure the classification success of machine learning algorithms, a 2x2 confusion matrix is created and the samples are placed in the relevant section of the matrix by examining their real tags and classified tags. The components of the complexity matrix are the above-mentioned TP, TN, FP and FN. Performance parameters are calculated using these values. In this study, Sensitivity, Specificity, Accuracy, Precision and F1 score were used as performance parameters as in similar previous studies. Sensitivity (SE), which is one of the two most important metrics, is sometimes referred to as recall; It is used to calculate the rate at which the falls can be correctly detected. Another important parameter is Specifity (SP) that measures the success of the system in not giving false alarms. In addition, the value of accuracy (ACC) is the parameter that enables the classification result to be scored overall (Haq et al., 2018). The precision parameter serves to determine reliability of the model by checking whether a fall is existing when the model gives a fall alert. Real success rate of the system is obtained with the F1 score to be obtained from two parameters; precision and recall (Kocaoğlu and Akdoğan, 2019). All parameters used in performance evaluation are given in Table 3.

## Falling Direction Classification

The main purpose of determining the fall of the elderly is to eliminate the negative effects of physiological and mental disorders that may occur after a fall as soon as possible. Therefore, when a fall is detected, the relevant

**Table 4.** Fall direction categories

| *Falling Direction* | *Activity* |
|---|---|
| *Forward* | *F01-F04-F05-F07-F08-F10-F13* |
| *Backward* | *F02-F11-F14* |
| Lateral | *F03-F09-F12F15* |
| *Vertical* | *F06* |

people are immediately informed and urgent medical support is requested. However, another area where fall detection systems can be used is to detect the falling direction of the individual and to eliminate the possibility of contact with the floor or other hard objects in the relevant direction. It is seen that researchers have used airbag systems to eliminate this impact contact in the past (Jung et al., 2020).

15 types of falling activities included in the SisFall dataset are classified as falling forward, backward and sideways (lateral) according to their directions as in Table 4. Only F06 (vertical fall while walking caused by fainting) defines the fainting and clutter drop, which can continue in any direction. Therefore, it is considered as a separate group. Again, classification is made using same machine learning algorithms. Each algorithm has been evaluated using machine learning performance parameters.

### Testing Phase

At the end of the training phase, the most successful classifier model was created separately for both two stages. The system success was measured again by using 30% of the data allocated for testing and never seen by the classifiers. Testing process is carried out by using compact models of classifiers created during training phase. The success of the system is evaluated based on the results obtained at the end of this stage.

## RESULTS AND DISCUSSION

The approach in this study consists of two stages: fall detection and falling direction detection. In k-folds cross validation, the relevant part of the dataset is divided into equal k parts. At each step, k-1 groups are used for training and performance is tested with the last group. This verification process is repeated k times. The performance of the classifier is calculated based on the k results (Haq et al., 2018). Choosing k at different values creates variation in classification performance. In this study, in both stages, 10 folds cross validation is used to re-check the results, since the best result was obtained in the case of k = 10.

## CONCLUSION

Herein, a new method of C. elegans immobilization is demonstrated using a standing surface acoustic wave-based microfluidic device. Thermoacoustically induced rapid temperature rises are applied inside a microfluidic channel to temporarily immobilize worm samples. The time required for immobilization is found to be much smaller compared to the chemical methods. The acoustic method is also more advantages compared to the laser-driven thermal methods due to the high throughput and device simplicity enabled by the surface acoustic wave device. Overall, the method presented in this work can be a valuable tool for worm researchers due to its simplicity, versatility and adoptability into microfluidic platforms.

### Fall Detection Results

At this stage, each observation in the train data is classified as fall or ADL. Table 5 gives the results of all classifiers. At this stage, the classification success of all classifiers gave similar results. Although DT lags behind other classifiers by 4% in terms of accuracy, it approached the classification success of similar studies in the literature with an accurate classification rate of 94,4%. ES k-NN achieved a success rate of 99% and produced a similar F1 score. As such, binary classification in the fall detection stage has a high degree of accuracy.

**Table 5.**Performance comparison of various classifiers during fall detection phase

| *Classifier* | *Type* | *SE* | *SP* | *ACC* | *PRE* | *F1* |
|---|---|---|---|---|---|---|
| *DT* | *Fine* | *94,9* | *93,8* | *94,4* | *95.3* | *95.1* |
| *SVM* | *Cubic* | *98,1* | *98,1* | *98.1* | *98.6* | *98.3* |
| KNN | *Fine* | *98,9* | *98,6* | *98.7* | *98.9* | *98.9* |
| RF |  | *98,8* | *98,3* | *98.6* | *98.7* | *98.7* |
| *Ensemble* | *Subspace k-NN* | *98,9* | *99,0* | *98.9* | *99.2* | *99.1* |

### Falling Direction Detection Results

At this stage, performance parameter results were obtained by testing with each classifier (Table 6). When the fall direction detection results are examined, it is seen that the ES-kNN algorithm is successful against other algorithms, although with a slight difference, as in the previous stage. Again, DT lags slightly behind other classifiers. Although the accuracy value of ES-kNN was 96,8%, the F1 score fell slightly behind this and became 93,8%. This is because the precision value is slightly lower than the accuracy value. This indicates that FPs are lower than FNs. Since the falling direction is being determined at this stage, this is due to the fact that the number of samples entering the random training set for each direction is not exactly equal.

### Testing Results

It is seen that models created in previous studies are ge-

**Table 6.**Performance comparison of various classifiers during fall direction detection phase

| *Classifier* | *Type* | *SE* | *SP* | *ACC* | *PRE* | *F1* |
|---|---|---|---|---|---|---|
| *DT* | *Fine* | *86.4* | *95.0* | *92.7* | *86.1* | *86.1* |
| *SVM* | *Cubic* | *91.8* | *97.2* | *95.8* | *91.8* | *91.8* |
| KNN | *Fine* | *93.9* | *97.2* | *96.3* | *92.3* | *93.1* |
| RF |  | *94.2* | *97.2* | *96.4* | *92.0* | *93.1* |
| *Ensemble* | *Subspace k-NN* | *94.9* | *97.5* | *96.8* | *92.8* | *93.8* |

**Table 7.**The testing results of ES k-NN Model

| *Stage* | *SE* | *SP* | *ACC* | *PRE* | *F1* |
|---|---|---|---|---|---|
| *Fall Detection* | *99.9* | *98.7* | *99.4* | *99.1* | *99.5* |
| *Falling Direction Detection* | *96.4* | *98.1* | *97.2* | *94.6* | *94.6* |

nerally not tested. In order to test the reliability of the classification, the classification was made using the testing data, which was not used before, on the model. The results of this classification also coincide with the results of the training classification (Table 7).

## CONCLUSION

In this study, the fall direction detection system is studied for elderly individuals. Direction detection creates a gap in the literature. It is seen that existing studies either detect falls binarily (fall/ADL) using various methods, or they try to determine exactly what falls and ADLs are. Binary fall detection success is observed to be very high in these studies, but success is low when activity detection is targeted. However, what is important in detecting a fall is not the reasons such as stumbling, fainting or losing balance, or head height during the fall, whether the knees touch the ground or not. The important detail in fall detection is to determine the direction of the fall and to prevent from hitting hard if it is possible. For this purpose, SisFall dataset, a very detailed dataset, was used in this study. Data belonging to two accelerometers and one gyroscope were used to create the processed dataset and a two-stage fall and fall direction detection system was developed. A total of 99 features are obtained with 11 various features extracted for three axes of each sensor and these features are used in both stages. As a result of the experiments made with 5 different machine learning algorithms, it was seen that the most successful classifier in both stages is ES k-NN. This classifier showed 98.9% accuracy in the fall detection stage and 96.8% accuracy in the fall direction detection stage. Similar results were obtained in the classification experiment using testing data corresponding to 30% of the total data, which were never used during the training on the ES k-NN model prepared.

In future studies, it can be tried to increase the classification success by using different techniques. By using different datasets together or using one of them with training and testing the other, a system can be developed that can be surer of its success when it is put into practice. While doing this study, our main goal was to develop a system that can predict the fall direction with high accuracy and take precautions against hitting the ground. We hope that in the next stages, airbags will be deployed in the determined direction and trials will be conducted with volunteers.

## CONFLICT OF INTEREST

Authors approve that to the best of their knowledge, there is not any conflict of interest or common interest with an institution/organization or a person that may affect the review process of the paper.

## AUTHOR CONTRIBUTION

All sections including conceptualisation, methodology, software, analysis, writing, review and editing were equally organised and performed by Sitki Kocaoglu and Yilmaz Guven.

## REFERENCES

1. Adhikari, K. (2019) ‘Computer Vision Based Posture Estimation and Fall Detection’, p. 131.
2. de Assis Neto, S. R. et al. (2019) ‘Detecting Human Activities Based on a Multimodal Sensor Data Set Using a Bidirectional Long Short-Term Memory Model: A Case Study’, in Ponce, H. et al. (eds) Challenges and Trends in Multimodal Fall Detection for Healthcare. Cham, Switzerland: Springer, pp. 31–51. doi: https://doi.org/10.1007/978-3-030-38748-8.
3. Casilari, E., Lora-rivera, R. and García-lagos, F. (2020) ‘A study on the application of convolutional neural networks to fall detection evaluated with multiple public datasets’, Sensors (Switzerland), 20(5). doi: 10.3390/s20051466.
4. Casilari, E., Santoyo-Ramón, J. A., & Cano-García, J. M. (2017). Analysis of public datasets for wearable fall detection systems. Sensors (Switzerland), 17(7). https://doi.org/10.3390/s17071513.
5. Chelli, A. and Patzold, M. (2019) ‘A Machine Learning Approach for Fall Detection and Daily Living Activity Recognition’, IEEE Access, 7, pp. 38670–38687. doi: 10.1109/ACCESS.2019.2906693.
6. Chen, J. et al. (2005) ‘Wearable sensors for reliable fall detection’, Annual International Conference of the IEEE Engineering in Medicine and Biology - Proceedings. IEEE, 7 VOLS, pp. 3551–3554. doi: 10.1109/iembs.2005.1617246.
7. Cho, H. and Yoon, S. M. (2019) ‘Applying singular value decomposition on accelerometer data for 1D convolutional neural network based fall detection’, Electronics Letters, 55(6), pp. 320–322. doi: 10.1049/el.2018.6117.
8. Daga, B. S., Ghatol, A. A. and Thakare, V. M. (2018) ‘Silhouette based human fall detection using multimodal classifiers for content based video retrieval systems’, 2017 International Conference on Intelligent Computing, Instrumentation and Control Technologies, ICICICT 2017, 2018-Janua, pp. 1409–1416. doi: 10.1109/ICICICT1.2017.8342776.
9. Delgado-Escaño, R. et al. (2020) ‘A cross-dataset deep learning-based classifier for people fall detection and identification’, Computer Methods and Programs in Biomedicine, 184. doi: 10.1016/j.cmpb.2019.105265.
10. Deng, Z., Zhu, X., Cheng, D., Zong, M., & Zhang, S. (2016). Efficient kNN classification algorithm for big data. Neurocomputing, 195, 143-148.
11. Gupta, R. et al. (2020) ‘Compressive sensing based privacy for fall detection’, pp. 1–10. Available at: http://arxiv.org/abs/2001.03463.
12. Han, J. et al. (2013) ‘Enhanced computer vision with Microsoft Kinect sensor: A review’, IEEE Transactions on Cybernetics. IEEE, 43(5), pp. 1318–1334. doi: 10.1109/TCYB.2013.2265378.
13. Han, Q. et al. (2020) ‘A Two-Stream Approach to Fall Detection

With MobileVGG', IEEE Access, 8, pp. 17556–17566. doi: 10.1109/access.2019.2962778.

14. Haq, A. U., Li, J. P., Memon, M. H., Nazir, S., & Sun, R. (2018). A hybrid intelligent system framework for the prediction of heart disease using machine learning algorithms. Mobile Information Systems, 2018.
15. Hussain, F., Hussain, F., Ehatisham-ul-Haq, M., & Azam, M. A. (2019). Activity-aware fall detection and recognition based on wearable sensors. IEEE Sensors Journal, 19(12), 4528-4536.
16. Jung, H. et al. (2020) 'Enhanced algorithm for the detection of preimpact fall for wearable airbags', Sensors (Switzerland), 20(5). doi: 10.3390/s20051277.
17. Kang, J. M., Yoo, T. and Kim, H. C. (2006) 'A wrist-worn integrated health monitoring instrument with a tele-reporting device for telemedicine and telecare', IEEE Transactions on Instrumentation and Measurement, 55(5), pp. 1655–1661. doi: 10.1109/TIM.2006.881035.
18. Kerdjidj, O. et al. (2020) 'Fall detection and human activity classification using wearable sensors and compressed sensing', Journal of Ambient Intelligence and Humanized Computing. Springer Berlin Heidelberg, 11(1), pp. 349–361. doi: 10.1007/s12652-019-01214-4.
19. Kocaoğlu, S. (2020). Investigating the Impact of Activity Class Number in Fall Detection Systems, Bilecik Şeyh Edebali University Journal of Science, 7(2), 886-895, DOI: 10.35193/bseufbd.714198.
20. Kocaoğlu, S., & Akdoğan, E. (2019). Design and development of an intelligent biomechatronic tumor prosthesis. Biocybernetics and Biomedical Engineering, 39(2), 561-570.
21. Krupitzer, C., Sztyler, T., Edinger, J., Breitbach, M., Stuckenschmidt, H., & Becker, C. (2018, March). Hips do lie! A position-aware mobile fall detection system. In 2018 IEEE International Conference on Pervasive Computing and Communications (PerCom) (pp. 1-10). IEEE.
22. Li, Q. et al. (2009) 'Accurate, fast fall detection using gyroscopes and accelerometer-derived posture information', Proceedings - 2009 6th International Workshop on Wearable and Implantable Body Sensor Networks, BSN 2009. IEEE, pp. 138–143. doi: 10.1109/BSN.2009.46.
23. Liu, K. C., Hsieh, C. Y., Hsu, S. J. P., & Chan, C. T. (2018). Impact of sampling rate on wearable-based fall detection systems based on machine learning models. IEEE Sensors Journal, 18(23), 9882-9890.
24. Martinez-Villasenor, L., Ponce, H. and Perez-Daniel, K. (2019) 'Deep learning for multimodal fall detection', Conference Proceedings - IEEE International Conference on Systems, Man and Cybernetics, 2019-Octob, pp. 3422–3429. doi: 10.1109/SMC.2019.8914429.
25. Mastorakis, G. and Makris, D. (2014) 'Fall detection system using Kinect's infrared sensor', Journal of Real-Time Image Processing, 9(4), pp. 635–646. doi: 10.1007/s11554-012-0246-9.
26. Myles, A. J., Feudale, R. N., Liu, Y., Woody, N. A., & Brown, S. D. (2004). An introduction to decision tree modeling. Journal of Chemometrics: A Journal of the Chemometrics Society, 18(6), 275-285.
27. Nait-Charif, H. and McKenna, S. J. (2004) 'Activity summarisation and fall detection in a supportive home environment', Proceedings - International Conference on Pattern Recognition. IEEE, 4, pp. 323–326. doi: 10.1109/ICPR.2004.1333768.
28. Nath, A., & Subbiah, K. (2018). The role of pertinently diversified and balanced training as well as testing data sets in achieving the true performance of classifiers in predicting the antifreeze proteins. Neurocomputing, 272, 294-305.
29. Nho, Y.-H., Lim, J. G. and Kwon, D.-S. (2020) 'Cluster-Analysis-based User-Adaptive Fall Detection using Fusion of Heart Rate Sensor and Accelerometer in a Wearable Device', IEEE Access, 4, pp. 1–1. doi: 10.1109/access.2020.2969453.
30. Noble, W. S. (2006). What is a support vector machine?. Nature biotechnology, 24(12), 1565-1567.
31. Nyan, M. N. et al. (2006) 'Distinguishing fall activities from normal activities by angular rate characteristics and high-speed camera characterization', Medical Engineering and Physics, 28(8), pp. 842–849. doi: 10.1016/j.medengphy.2005.11.008.
32. Oshiro, T. M., Perez, P. S., & Baranauskas, J. A. (2012). How many trees in a random forest?. In International workshop on machine learning and data mining in pattern recognition (pp. 154-168). Springer, Berlin, Heidelberg.
33. Psathas, A. P., Papaleonidas, A., Papathanassiou, G., Valkaniotis, S., & Iliadis, L. (2020). Classification of Coseismic Landslides Using Fuzzy and Machine Learning Techniques. In International Conference on Engineering Applications of Neural Networks (pp. 15-31). Springer, Cham.
34. Putra, I. P. E. S. et al. (2018) 'An event-triggered machine learning approach for accelerometer-based fall detection', Sensors (Switzerland), 18(1), pp. 1–18. doi: 10.3390/s18010020.
35. Putra, I. P. E. S. and Vesilo, R. (2018) 'Window-size impact on detection rate of wearable-sensor-based fall detection using supervised machine learning', 2017 IEEE Life Sciences Conference, LSC 2017, 2018-Janua, pp. 21–26. doi: 10.1109/LSC.2017.8268134.
36. Riquelme, F., Espinoza, C., Rodenas, T., Minonzio, J. G., & Taramasco, C. (2019). Ehomeseniors dataset: An infrared thermal sensor dataset for automatic fall detection research. Sensors (Switzerland), 19(20). https://doi.org/10.3390/s19204565
37. Saleh, M. and Le Bouquin Jeannès, R. (2018) 'An efficient machine learning-based fall detection algorithm using local binary features', European Signal Processing Conference. EURASIP, 2018-Septe, pp. 667–671. doi: 10.23919/EUSIPCO.2018.8553340.
38. Saleh, M. and Jeannes, R. L. B. (2019) 'Elderly Fall Detection Using Wearable Sensors: A Low Cost Highly Accurate Algorithm', IEEE Sensors Journal. IEEE, 19(8), pp. 3156–3164. doi: 10.1109/JSEN.2019.2891128.
39. Srinivasan, S. et al. (2007) 'Towards automatic detection of falls using wireless sensors', Annual International Conference of the IEEE Engineering in Medicine and Biology - Proceedings, pp. 1379–1382. doi: 10.1109/IEMBS.2007.4352555.
40. Sucerquia, A., López, J. D. and Vargas-Bonilla, J. F. (2017) 'SisFall: A fall and movement dataset', Sensors (Switzerland), 17(1). doi: 10.3390/s17010198.
41. Sucerquia, A., López, J. D. and Vargas-Bonilla, J. F. (2018) 'Real-life/real-time elderly fall detection with a triaxial accelerometer', Sensors (Switzerland), 18(4), pp. 1–18. doi: 10.3390/s18041101.
42. United Nations (2019) World Population Prospects 2019, Department of Economic and Social Affairs. World Population Prospects 2019. Available at: http://www.ncbi.nlm.nih.gov/pubmed/12283219.
43. WHO (2007) Falls. Available at: https://www.who.int/news-room/fact-sheets/detail/falls (Accessed: 19 February 2020).
44. Wu, G. (2000) 'Distinguishing fall activities from normal activities by velocity characteristics', Journal of Biomechanics, 33(11), pp. 1497–1500. doi: 10.1016/S0021-9290(00)00117-2.
45. Yacchirema, D., de Puga, J. S., Palau, C., & Esteve, M. (2018). Fall detection system for elderly people using IoT and big data. Procedia computer science, 130, 603-610.

Hittite Journal of Science and Engineering, 2021, 8 (3) 207–220
ISSN NUMBER: 2148–4171
DOI: 10.17350/HJSE19030000231

# A Review and Classification of Most Used MPPT Algorithms for Photovoltaic Systems

**Omer Faruk Tozlu**[1] **Huseyin Calik**[2]
[1]Hitit University, Department of Electrical and Electronics Engineering, Corum, Turkey
[2]Giresun University, Department of Electrical and Electronics Engineering, Giresun, Turkey

***Article History:***
*Received: 2021/03/01*
*Accepted: 2021/07/01*
*Online: 2021/09/29*

***Correspondence to**: Ömer Faruk Tozlu, Deparment of Electrical and Electronics Engineering, Hitit University, Çorum, Turkey*
*Tel: +90 3642274533*
*E-Mail:omerfaruktozlu@hitit.edu.tr*

## ABSTRACT

Energy has become an indispensable need to sustain our lives. Approximately 80% of the energy consumed in the world is produced from fossil sources. For the reasons such as the depletion of fossil resources and their damages to the environment, the interest in renewable resources is increasing and the importance of solar systems, which draws attention with unlimited energy resource, is increasing day by day. The biggest disadvantages of solar systems are seen as low production efficiency and high setup cost. A PV cell can convert only 5-20% of the solar energy coming on it to electricity. Based on this, it is very important to provide the power obtained from PV with maximum efficiency and minimum cost. Accordingly, many different maximum power point tracking (MPPT) algorithms have been proposed over the years. Although the purpose of all proposed algorithms is the same, they have many advantages and disadvantages compared to each other. In this study, the most used MPPT algorithms have been examined and compared by considering many parameters such as tracking speed, stability, and cost etc. and a new classification of these algorithms is proposed.

**Keywords:**
MPPT; Photovoltaic; Incremental conductance; Perturb and observe; Intelligent methods; Particle swarm optimization

## INTRODUCTION

Energy, which can be defined as the ability to do work in its basic form, is in an indispensable position to sustain human life, meet their needs, and increase the quality of life. Over time, there is a serious increase in the total energy consumed in the world due to many reasons such as the increase in the human population, changes in people's lifestyle, increase in production, and technological developments. Energy production should be increased in order to meet the energy needs. Approximately 80% of the energy produced in the world is produced in power plants where natural gas and coal are used as the main energy source [1]. It is thought that toxic gases such as carbon, sulfur, heavy metals mixed into the soil and many other wastes released into the atmosphere during energy production from these limited fossil resources on earth will have negative effects on nature and living things over the years. Renewable energy sources, especially solar energy, are seen as an important alternative here. Because the sun sends more than the energy consumed in the world as clean energy every day. Solar energy has gained a place as a serious choice with its advantages such as very low operating and maintenance costs and being the most ecofriendly energy. In addition to all these advantages, it also has disadvantages such as low efficiency, especially in energy conversion, and high setup cost. Numerous studies are carried out in order to obtain maximum efficiency from photovoltaic (PV) panels [2–4].

Solar energy is produced by converting the photon energy carried by the light coming to the surface of the panels formed by the combination of photovoltaic cells, into electric current by p-n junction in these cells. As the wavelength of the light gets shorter, the amount of energy carried by the photon increases. On the other hand, the angle of the light that comes to the panel is also very important. The angle of the sunray comes on the earth constantly changes during the day. Consequently, the amount of radiation absorbed by the solar panel (photovoltaic cells) will also change, so the energy obtained will be different at each time interval. PV cells can basically be compared to a p-n junction diode. The equivalent circuit model of the PV cell was described by Lorenzo in 1994 [5]. This model consists of a current source and a parallel diode connected to it. Here, the series resistance ($R_s$) refers to the internal losses of the

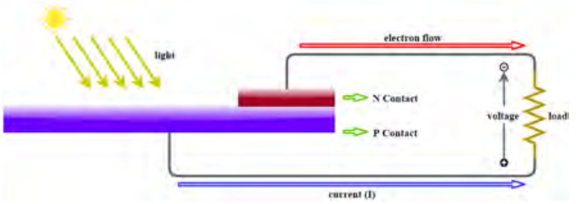

**Figure 1.** Basic structure of the PV cell

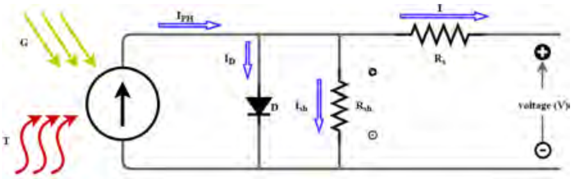

**Figure 2.** Equivalent circuit of PV cell

solar cell caused by the current flow and it is desired to be minimized for maximum power generation. The ($R_{sh}$) resistance connected in parallel to the diode refers to the losses caused by the leakage currents to the ground, it is generally neglected because the current value is too low, and the resistance value is too high. The basic structure of the PV cell is shown in Fig. 1 and its equivalent circuit in Fig. 2.

The equations expressing the current and voltage of the PV cell are given below. Here, the series resistance ($R_s$), ideality factor (n), and parallel resistance ($R_{sh}$) are parameters that vary according to the characteristics of the PV cell. Other parameters are Boltzmann constant (k), electron charge (q), and solar cell temperature (T). IPH refers to the photon current and IS to the saturation current.

$$I = I_{PH} - I_S\left[\exp\left(\frac{q}{n.k.T}(V + R_s.I)\right) - 1\right] - \frac{V + R_s.I}{R_{sh}} \qquad (1)$$

The equation of IPH current based on radiation and temperature is given below. In the atmospheric conditions specified with the standard test condition (STD) here, the ambient temperature is 25 °C, the radiation is 1000 W/m², and the air mass is 1.5. T temperature, G radiation, and $K_I$ represent the temperature coefficient of the $I_{sc}$.

$$I_{PH} = \left(I_{SC\_STD} + K_I\left(T - T_{STD}\right)\right).\frac{G}{G_{STD}} \qquad (2)$$

$$V = \frac{n.k.T}{q}\ln\left(\frac{I_{PH} + I_S - I}{I_S}\right) - R_s.I \qquad (3)$$

When the necessary negligence and simplifications are made, the I-V characteristic of a PV cell, shown in Fig. 3, can be written with the Shockley diode equation below.

$$I_D = I_S.\exp\left(\frac{qV}{kT} - 1\right) \qquad (4)$$

The point where the maximum power is transferred to the load is called the maximum power point (MPP) and this is the point C ($I_{opt}$, $V_{opt}$) in Fig. 3. The suitable value received by the load for this point is $R_{opt}$. The maximum power $P_{max}$ can be written as follows:

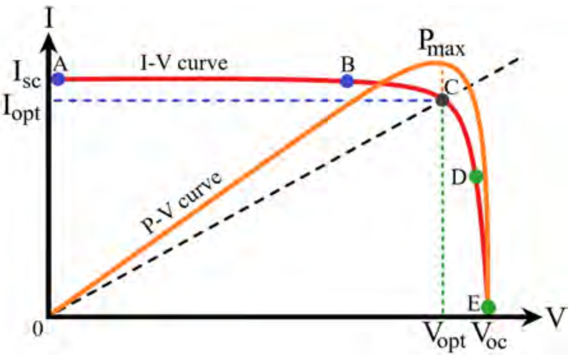

**Figure 3.** Typical current-voltage characteristics of the PV cell

$$P_{max} = V_{opt}.I_{opt} = I_{opt}{}^2.\,R_{opt} = \frac{V_{opt}{}^2}{R_{opt}} \qquad (5)$$

The load characteristic can be found linearly as the slope of $I/V = 1/R$ for an ohmic load. It can be said that the power transferred to the load depends only on the resistance. Accordingly, if the load R is too low, the PV cell will operate close to the $I_{sc}$ as a current source in the A-B range in Fig. 1. If the load R is quite high, then the solar cell will operate at a value close to the $V_{oc}$ as a constant voltage source in the D-E range of the curve [6]. For the system to function correctly, an increasing and decreasing irregular power supply cannot be given directly to the load. These power values need to be made regular and efficient. MPPT is used to perform this process. In other words, the purpose of MPPT is to obtain maximum power from PV panels in all conditions by matching the I-V operating point with the load characteristics [7]. The delivered power can be maximized by regulating the current or voltage of the PV panel to force the converter operate at the MPP [8,9].

PV systems always have a DC-DC converter. MPPT controls the DC-DC converter, forcing the PV system to operate at MPP. Fig. 4 shows the operating scheme of the MPPT system. The MPPT usually measures the input and/or output voltage/current of the PV, and it sends a suitable control signal to the DC-DC converter by processing this data to operate the system in MPP. Here, the measured data is processed with the help of reference values, the error is detected, and the DC-DC converter is controlled with the appropriate PWM signals adjusted by modifying the duty cycle for the point where the maximum power can be obtained.

Over the years, Perturb and Observe (P&O) [7,11–13], Incremental Conductance (IncCond) [14–18], Fuzzy Logic [19–21] etc. many different MPPT algorithms have been proposed. Although the purpose of all proposed algorithms is the same, they have many advantages and disadvantages

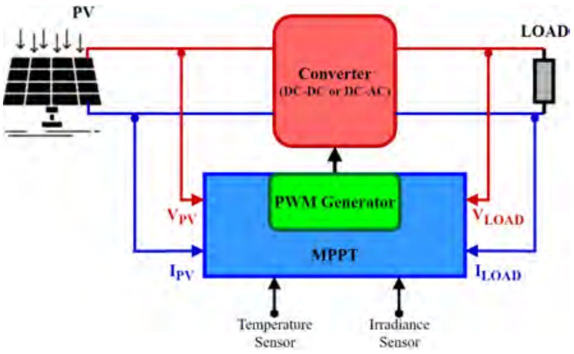

**Figure 4.** Operating scheme of the MPPT system [10]

compared to each other. In this study, MPPT algorithms, accepted in the literature, were examined, and compared considering many parameters such as speed, complexity and cost etc. A new classification of MPPT algorithms is proposed.

## MPPT ALGORITHMS

In order to obtain maximum power and efficiency from the PV panel, many methods are proposed, and each of these methods has different advantages and disadvantages. Therefore, the most appropriate method should be chosen for each system. Here, many parameters such as the atmospheric conditions of the region where the system will be installed, sunshine duration, and the budget allocated to the system should be taken into consideration.

MPPT methods can be classified by different names. There are different approaches in these classifications such as the characteristics of the algorithm and tracking method. Generally, these are divided into classes such as indirect, direct, soft computing, or conventional, inteligent methods depending on the method of application [2,22–24]. MPPT algorithms can be classified under headings such as constant parameters, measurement-and-comparison, mathematical calculation, trial-and-error, and intelligent according to the tracking method [25]. In indirect methods, MPP is calculated with simple assumptions without measuring the power of the PV. In direct methods, parameters such as power, voltage, and current of PV are measured with the help of sensors and MPP is determined with processing these measured values.

The most used classification is divided MPPT algorithms into two class as conventional and intelligent. In this paper, MPPT algorithms are examined according to this classification and a new classification is proposed.

### Conventional Methods

#### *Constant Voltage (CV)*

The simplest MPPT method, CV, is applied by fixing the PV voltage to a value close to the VMPP reference value. The PV voltage is measured, compared with VMPP, an error is found, and the voltage is adjusted according to the error. The flowchart of the method is shown in Fig. 5. In this method, true MPP cannot be achieved because the effect of temperature and radiation are not included in the algorithm. The most important advantage of this method is that it is more efficient than many more expensive methods under low radiation [26]. Due to this feature, it is preferred in some cases.

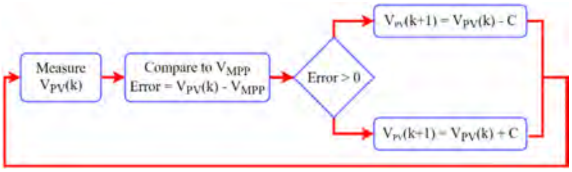

**Figure 5.** Constant voltage method flowchart

#### *Fractional Open-Circuit Voltage (FOCV)*

The $V_{oc}$ shown in Fig. 3 expresses the open circuit voltage of the PV panel. In the FOCV, the $V_{oc}$ at the ends of the PV panel is measured, and multiplied with a certain coefficient to find the Vopt [27]. The equation between $V_{oc}$ and $V_{opt}$ is expressed as follows:

$$V_{opt} = V_{oc}.k_{oc} \quad (0 < k_{oc} < 1) \tag{6}$$

Here, $k_{oc}$ coefficient depends on factors such as the production technology of the panel and atmospheric conditions. The optimum voltage usually corresponds to 76% of the open circuit voltage. Researches have shown that the $k_{oc}$ value is in the range of 0.73-0.80 [28]. The key disadvantage of the method whose flowchart shown in Fig. 6 is that the PV power has to be cut off suddenly to measure the $V_{oc}$ [29]. It is preferred in some cases due to its low cost and simple application.

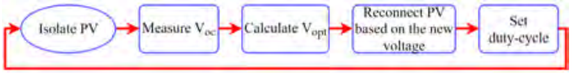

**Figure 6.** Fractional open-circuit voltage method flowchart

#### *Open-Circuit Voltage with Pilot PV Cell (FOCVPVC)*

The method is same as the FOCV. The only difference here is that instead of making the entire panel open circuit, $V_{opt}$ is calculated over the $V_{oc}$ of a single cell, independent of other cells, and named as a pilot. Thus, interruptions during voltage measurement, one of the most important disadvantages of the FOCV, are prevented.

However, it works more inefficiently in cases such as partial shading [26,30].

### *Fractional Short-Circuit Current (FSCC)*

In this method, which is very similar to the FOCV, $I_{opt}$ is calculated by measuring the $I_{sc}$ of the PV [31]. The relationship between short circuit current and optimum current is given below:

$$I_{opt} = I_{sc}.k_{sc} \quad (0 < k_{sc} < 1) \tag{7}$$

Here, $k_{sc}$ coefficient depends on same conditions. The optimum current generally corresponds to 86% of the open circuit current. Researches have shown that the $k_{sc}$ value is in the range of 0.78-0.92 [32]. In FSCC whose flowchart shown in Fig. 7, it is more difficult to determine $I_{sc}$ because of heat dissipation and increase in power loss. It may not always be physically possible to short circuit the system. In addition, additional materials such as switches and current sensors may be needed [33]. This increases the cost and the loss in energy produced. For these reasons, the FOCV is more preferred between these simple two methods.

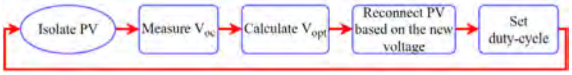

**Figure 7.** Fractional short-circuit current method flowchart

### *Look-up Table (LUT)*

In the LUT whose flowchart is given in Fig. 8, the data of PV under all possible atmospheric conditions is recorded and a table is created. A new $V_{opt}$ value is determined in each round by comparing the actual values with the saved ones. In the LUT, since it is assumed that the actual conditions of the PV are the conditions in which the data in the table is recorded, in some cases the $V_{opt}$ may not be determined correctly enough [12]. As the table expands, the efficiency and the system memory needed increase. Since increasing the system memory will increase the cost, tables with optimum dimensions are preferred and some possible conditions are neglected. This situation negatively affects the capture of MPP [34,35].

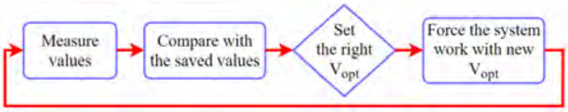

**Figure 8.** Look-up table method flowchart

### *Load Current or Load Voltage Maximization (LCLVM)*

In this method, it is assumed that when the output power is maximized in a lossless converter, the input power will also be maximized. Load voltage or current is maximized depending on the characteristics of the load. Thus, it is assumed that the input power also reaches its maximum. One of the major disadvantages of the method is that the converter is not lossless, so MPP cannot be fully tracked. By increasing the quality of the converter, the loss can be minimized, but this will increase the cost [36,37].

### *PV Output Senseless (POS)*

The flowchart of the method, generally used in large-scaled systems, is shown in Fig. 9. In large-scaled PV systems, the voltage drop at the output is negligible. In this case, the maximum power can be considered directly proportional to the maximum current. In POS, the old and new duty-cycle data are compared, and the load current is taken as a feedback, thus minimizing the error [38]. One of the major advantages of the method, which responds quickly to sudden atmospheric changes and shading, is that the system does not require any measurement from the PV side [39].

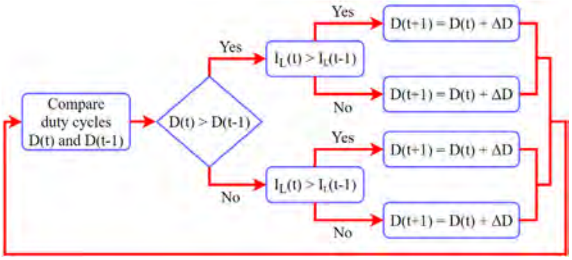

**Figure 9.** PV output senseless flowchart

### *Perturb and Observe (P&O)*

In the P&O, which is one of the most widely used methods among all MPPT algorithms, MPP or the closest point to MPP is found by trial-and-error method. The most important reason for its widespread use is that it can be easily applied to any system regardless of its PV properties and it can find MPP with acceptable accuracy at low cost. The flowchart of the P&O method is shown in Fig. 10. In the method, PV power is calculated with the measured voltage and current of the panel. According to the change in PV power, it is decided what to do next. If an increase in the obtained power is detected, the operating voltage continues to be increased or decreased in the same direction. However, if there is a decrease in the power, the operating voltage is changed in the opposite direction. In this method, although MPP cannot be caught completely, an oscillation is made in a range close to MPP. The most important disadvantage of the method is fast changing atmospheric conditions and shading. Since the power obtained from the PV at the time of shading will decrease, the direction in which the operating voltage will be changed may not be determined correctly [16,40–42].

The major disadvantage of the method based on tracking speed and perturbation step is that it oscillates near the

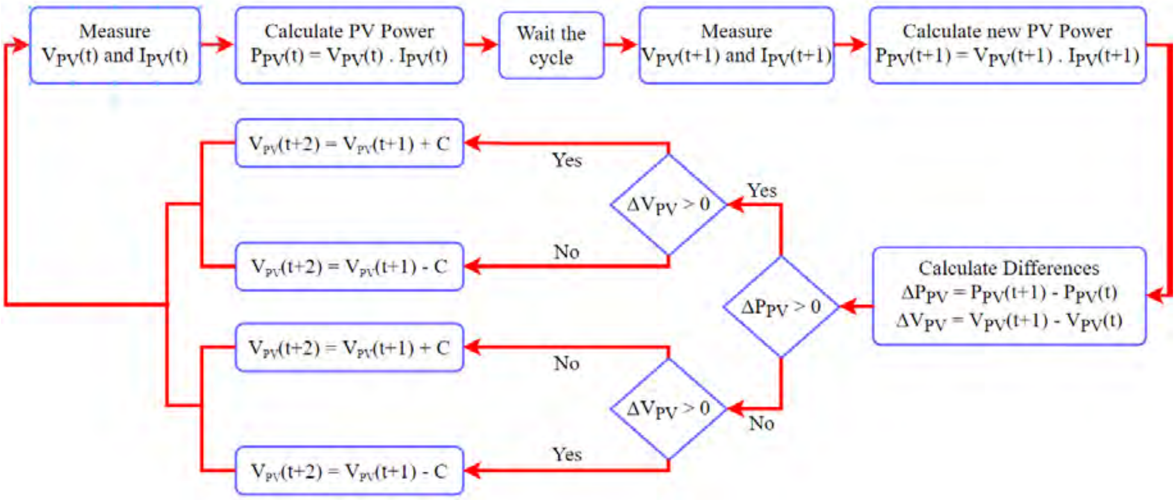

**Figure 10.** Perturb and observe flowchart

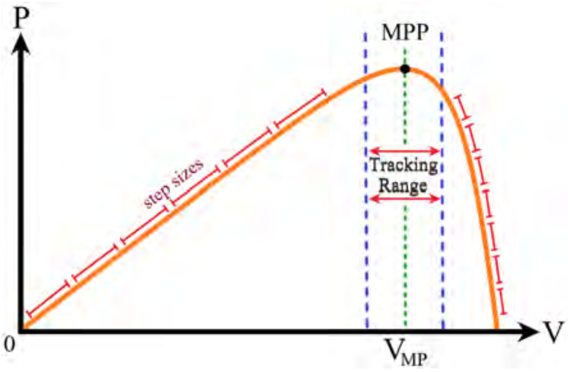

**Figure 11.** P-V curve of perturb and observe algorithm

MPP instead of capturing the true MPP. When the P-V curve seen in Fig. 11 is examined, it is seen that the power increases almost linearly until the certain value of the voltage and decreases very rapidly after the peak point. In the method, the oscillation around the MPP is minimized with a flexible step size. The step size gets smaller as it gets closer to the MPP and gets bigger as it gets further away. In some studies, the step size is estimated with different algorithms. Thus, a more efficient P&O can be obtained [43–45].

### *Three-Point Weight Comparison (TPWC)*

TPWC works similarly to P&O. The power is calculated by comparing the values at two different moments in P&O and three in TPWC. Since the power of one step ahead and one step behind is calculated and decided accordingly in the PV curve, a closer operation is provided to MPP. Where X is the current point, Y is one step ahead and Z is one step behind, a point is considered positive if it has more power than the previous point, and negative if not. The duty-cycle is increased if two of the points are positively weighted, is decreased if negative. The closest point to MPP is reached when the total weight is zero [3]. In Fig. 12, the flowchart of TPWC and possible nine situations for three points are given. Here, the blue, green, and black colored circles represent the X, Y, and Z positions, respectively.,

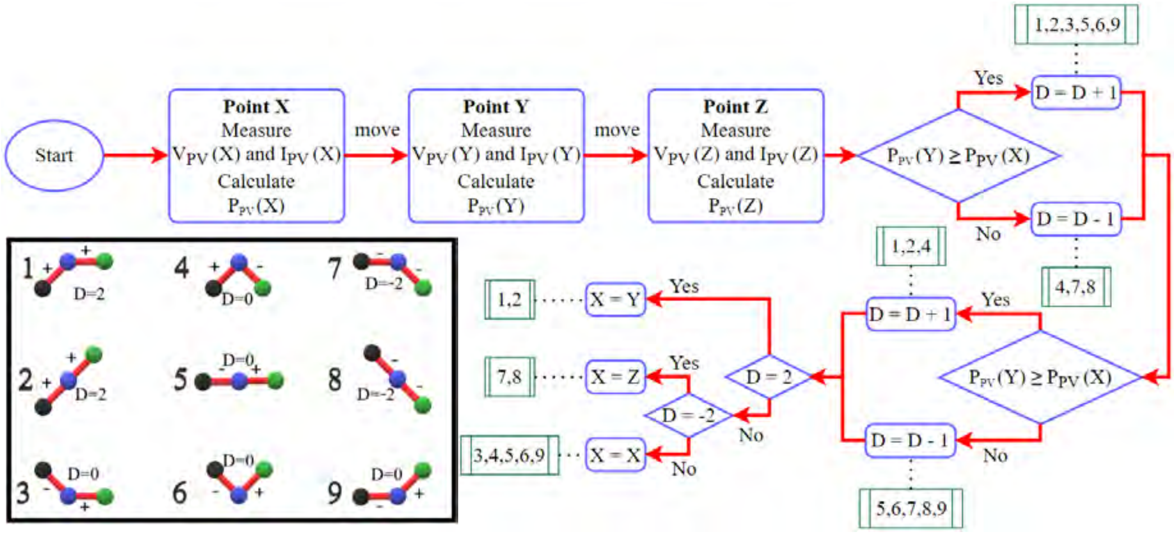

**Figure 12.** Three-point weight comparison flowchart

### *Hill Climbing (HC)*

The flowchart of the HC is shown in Fig. 13. In the HC method, which operates similarly P&O, the duty cycle is changed directly instead of changing the current or voltage as in the P&O. In the HC, the duty cycle D is periodically adjusted with an offset (constant perturbation) with the direction of increase in power. If the power change is negative, the perturbation direction is reversed. Fixed or variable step size can be determined as in P&O. Similarly, not reaching true MPP under partial shading is seen as the major disadvantage [46,47].

**Figure 13.** Hill climbing flowchart

### *On-Line MPP Search (OLMPP)*

In the OLMPP, the maximum power error is found by comparing the instant power with the reference maximum power value, and this error is approached to zero to reach MPP. The method, whose flowchart is given in Fig. 14, has been created based on the operating power of the load. Initial reference values are taken as $P_{ref} = 0$, $I_{ref} = 0$ and $V_{ref} = V_{oc}$. The output voltage is controlled by the load current. Therefore, deviations from MPP occur if the load current or power is low. Additional load connections can be made to prevent this situation, but this causes losses. Another disadvantage of the method is that it adapts slowly to changing atmospheric conditions [48].

### *DC-Link Capacitor (DCLC)*

In this method, a converter (AC) is connected to the PV system. The basic structure of DCLC is shown in Fig. 15, is based on the voltage drop on a capacitor connected to the output of the DC-DC converter. The relationship between the $V_{PV}$ and the $V_{link}$ is expressed in the following equation:

$$D = 1 - \frac{V_{PV}}{V_{link}} \tag{8}$$

where D is the duty ratio of the ideal boost converter.

The output power so the power obtained from the PV, increases if the output current of the boost converter is increased. If the power needed by the converter does not exceed the maximum $P_{PV}$, the output power of the boost converter is kept constant. When the maximum power is exceeded, the voltage on the link capacitor starts to drop. Before this drop, the current $I_{peak}$ of the converter is at the maximum point and the system is operating at MPP. The current (AC) is used as feedback to prevent the $V_{link}$ from falling. The duty cycle D is regulated to keep Ipeak at maximum [49,50].

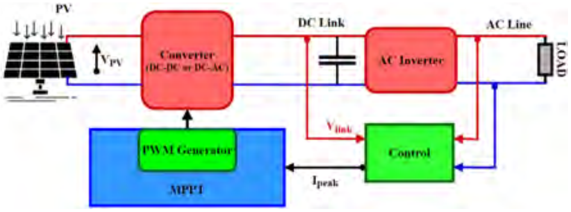

**Figure 15.** DC-Link capacitor scheme

### *Incremental Conductance (IncCond)*

The two main disadvantages of the P&O method are the oscillation around MPP and its slowness to adapt to rapidly changing atmospheric conditions. IncCond method has been developed to avoid these disadvantages [14]. By measuring the output voltage and current of the PV, its power and conductivity are computed, and the duty cycle required to operate the system at MPP is determined [17]. The flowchart of the IncCond is given in Fig. 16.

When the ratio of PV power difference to voltage difference is zero, MPP is captured and it can be expressed with the following equations:

$$\frac{dP_{PV}}{dV_{PV}} = \frac{d\left(V_{PV}.I_{PV}\right)}{dV_{PV}} = I_{PV} + V_{PV}\frac{dI_{PV}}{dV_{PV}} = 0 \tag{9}$$

$$\frac{I_{PV}}{V_{PV}} = -\frac{dV_{PV}}{dI_{PV}} \cong -\frac{\Delta V_{PV}}{\Delta I_{PV}} \tag{10}$$

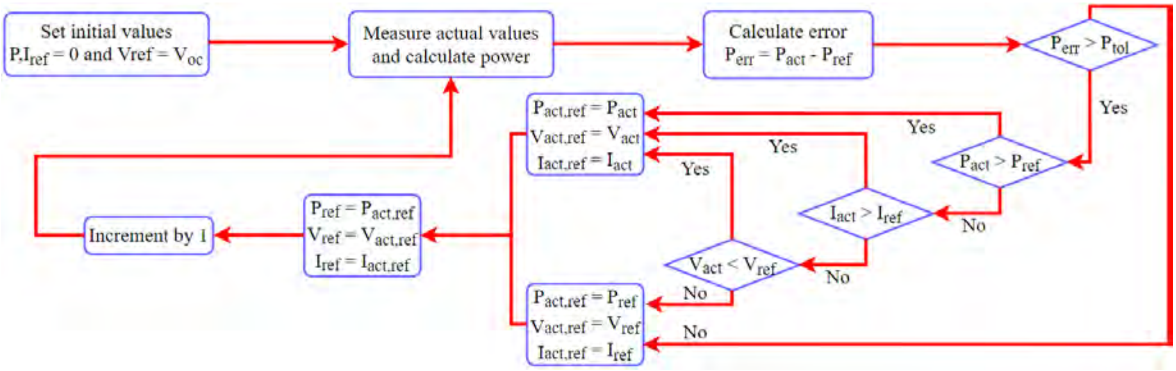

**Figure 14.** On-line search flowchart

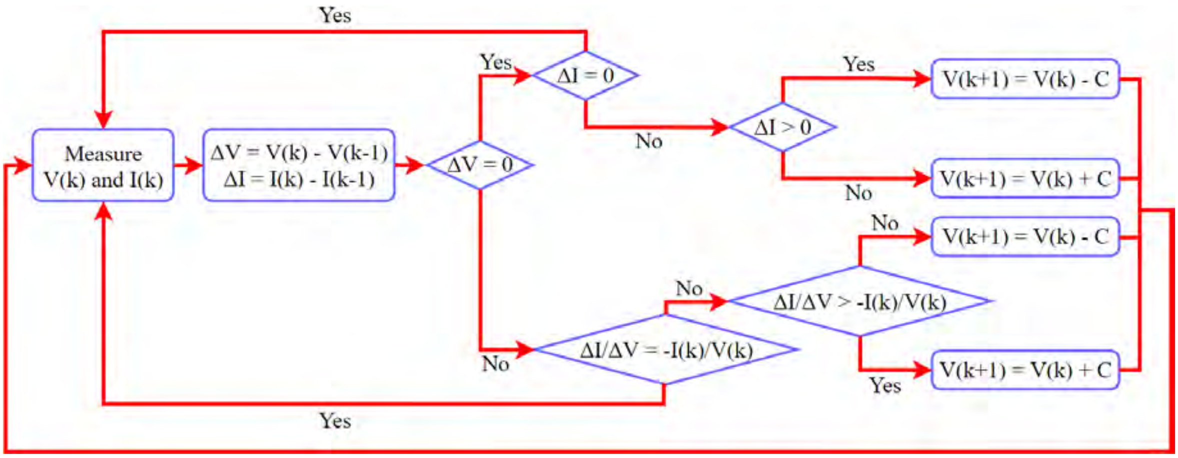

**Figure 16.** Incremental conductance flowchart

In the P-V curve, the slope is zero in MPP, it increases (positive) on the left of the MPP and decreases on the right (negative):

$$\frac{dP_{PV}}{dV_{PV}}=0 \quad \text{if} \quad \frac{dI_{PV}}{dV_{PV}}=-\frac{I_{PV}}{V_{PV}} \quad \text{at MPP} \qquad (11)$$

$$\frac{dP_{PV}}{dV_{PV}}>0 \quad \text{if} \quad \frac{dI_{PV}}{dV_{PV}}>-\frac{I_{PV}}{V_{PV}} \quad \text{left of MPP} \qquad (12)$$

$$\frac{dP_{PV}}{dV_{PV}}<0 \quad \text{if} \quad \frac{dI_{PV}}{dV_{PV}}<-\frac{I_{PV}}{V_{PV}} \quad \text{right of MPP} \qquad (14)$$

The IncCond method shows the ability to adapt more quickly to sudden changes in atmospheric conditions while narrowing the oscillation around MPP, which are the major disadvantages of P&O [13,15]. Although it basically works the same as P&O, more complex control structures are used in the IncCond method [16]. Instead of the voltage based on the method, current can also be chosen. In this case, the new method is called Incremental resistance (IncRes) [51,52].

### *Parasitic Capacitance (PC)*

There are two major reactive parasitic elements in PV cells. These are called parasitic inductance and capacitance. The PC method is very similar to IncCond, but in this method, the parasitic capacitance Cp of the PV cell is also taken into account. Parasitic capacitance is caused by loads in the junction area [53]. If this generally neglected parasitic effect is included in the calculations, the following current equation is obtained:

$$I_{PV}(t)=I_{ph}-I_s\left(e^{\lambda\left(V_{pv}+I_{PV}.R_s\right)}-1\right)+I_c(t) \qquad (14)$$

Here $I_c$ shows the capacitor current and is defined by the following equation:

$$I_c(t)=C_p\frac{dV_{PV}}{dt} \qquad (15)$$

The following power equation is obtained by updating Equation (14):

$$I_{PV}(t)=F\left(V_{PV}(t)\right)+C_p\dot{V}_{PV}(t) \qquad (16)$$

$$P_{PV}(t)=\left[F\left(V_{PV}(t)\right)+C_p\dot{V}_{PV}(t)\right].V_{PV}(t) \qquad (17)$$

Here, if the derivative of PV power to its voltage is taken, the MPP equation is obtained as in the IncCond method. Here the dot represents the degree of the derivative:

$$\frac{dP_{PV}(t)}{dV_{PV}(t)}=\frac{dF\left(V_{PV}(t)\right)}{dV_{PV}(t)}.V_{PV}(t)+F\left(V_{PV}(t)\right)=0 \qquad (18)$$

$$\frac{dF\left(V_{PV}(t)\right)}{dV_{PV}(t)}=-\frac{F\left(V_{PV}(t)\right)}{V_{PV}(t)} \qquad (19)$$

$$\frac{\dot{I}_{PV}(t)}{\dot{V}_{PV}(t)}=-\frac{I_{PV}(t)}{V_{PV}(t)} \qquad (20)$$

In Equation (20), the left side shows incremental conductance, while the right side shows instant conductance. If the second-order derivative is taken, the following maximum power equation is obtained:

$$\frac{dF\left(V_{PV}(t)\right)}{dV_{PV}(t)}+C\left(\frac{\ddot{V}_{PV}(t)}{\dot{V}_{PV}(t)}+\frac{\dot{V}_{PV}(t)}{V_{PV}(t)}\right)+\frac{F\left(V_{PV}(t)\right)}{V_{PV}(t)} \qquad (21)$$

Here, three expressions refer to incremental inductance, the induced ripple from $C_p$, and instantaneous inductance, respectively. If C = 0 is taken in this equation, the equality of the IncCond method is obtained. Parasitic capacitance can be modeled as a parallel capacitor to each PV cell, parallel connection of many modules in large-scale systems increases efficiency due to parasitic capacitance [54,55].

## Intelligent Methods

### *Fuzzy Logic (FL)*

With the development of processor technology, the usage areas of fuzzy logic control have expanded. The use of FL for MPPT provides many advantages. Some of them are to track the MPP with high accuracy, not be affected by the disruption of the inputs, and work independently from the system model, unpredictable, and non-modeling physical data [19,56]. The FL method consists of three stages. In the first stage, fuzzification, numerical data are converted into linguistic values with the help of membership function. There are five levels here: Z (Zero), NS (Negative Small), PS (Positive Small), NB (Negative Big), and PB (Positive Big) [57]. The inputs of the FL algorithm generally consist of functions expressing error (E) and change in error (ΔE), whose equations are given below:

$$E = \frac{P_{PV}(t) - P_{PV}(t-1)}{V_{PV}(t) - V_{PV}(t-1)} \tag{22}$$

$$\Delta E(t) = E(t) - E(t-1) \tag{23}$$

In the second stage, Rule table, entries are processed, and a decision is made. In the last step, defuzzification, linguistic data are transformed into crisp data.

### *Artificial Neural Networks (ANN)*

ANN generally consist of three layers. The first part, input layer, indicates the part where the data is received, the second part, hidden layer, the part where the data is processed in a complex structure, and the last part, output layer, refers to the part where the obtained results are [58,59]. The basic structure of artificial neural networks can be seen in Fig. 17. Input data in neural networks can be PV module parameters such as $I_{sc}$, $V_{oc}$, temperature, radiation, atmospheric measurements, or various combinations of these. Duty cycle data that will drive the DC-DC converter is obtained at the output. In this method, input data are processed with certain weights in the hidden layer and it may take days or years to find the ideal weights. Each network structure is trained on the PV system, so it cannot be directly applied to a different system. However, the network trained for a system enables the system to work in true MPPT without being affected by the change of PV module parameters or environmental factors [20,60,61].

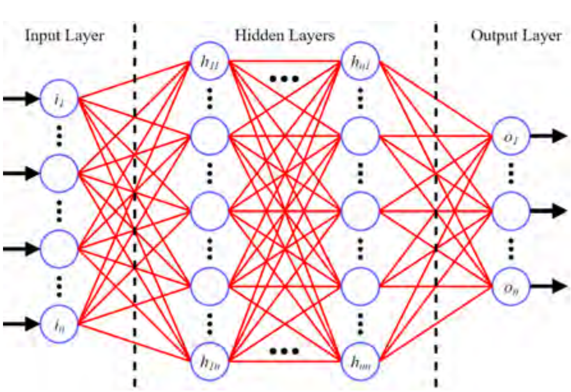

**Figure 17.** Artificial neural network scheme

### *Particle Swarm Optimization (PSO)*

PSO is a population-based stochastic method of optimization. There are many different PSO methods created by examining the social behaviors of flocks. In the PSO method, the elements that are part of a flock are randomly distributed into value ranges for optimum solution and the search continues for generations. All members develop their own solutions by simulating the success of their neighbors [62,63]. The position $x_i$ of an element is calculated by the following equation:

$$x_i^{t+1} = x_i^t + v_i^{t+1} \tag{24}$$

Here $v_i$ is the velocity element showing the step size. If the speed decreases, the control gets slow if the speed increases, the control gets unstable [62]. The next value is calculated with the following equation:

$$v_i^{t+1} = wv_i^t + c_1 r_1 \left(P_{best\_i} - x_i^t\right) + c_2 r_2 \left(G_{best} - x_i^t\right) \tag{25}$$

Here w is the internal weight, $c_{1,2}$ are the coefficients of acceleration, $r_{1,2}$ are the values in the range of 0-1. $P_{best\_i}$ and $G_{best\_i}$ represents the best personal position and the best neighborhood position of the particle i, respectively. The most important disadvantage of the PSO is the adjustment of the parameters.

### *Ant Colony Optimization (ACO)*

The ACO was first introduced in 1990s and applied to some combinational optimization problems sucsesfully [64]. In years, this technique has been more popular for researchers and various applications of ACO have been made [65]. The ACO, probabilistic algorithm, is preferred to find the global optimum paths based on the behavior of foraging ants. Ants move randomly along the paths and explore the area in search of food. While transporting food to the nest, ants leave a trail of chemical pheromones on the way for other ants to reach the food faster. During the action period, the amount of pheromone increases according to the amount of food and this shortens the path to food for the colony [66].

For continuous domains, one of the most common ACO-based algorithms, $ACO_R$, is based on the Gram Schmidt process. ACO algorithms use a pheromone model to generate probabilistic solutions for combinatorial optimization problems. But $ACO_R$ uses the solution archive as a way to identify the pheromone distribution over the space of search. A limited number of the complete solutions of the problem are stored in memory called the solution archive. For generating new solutions, the archive acts like a reference [67]. The equations given below are used in ACOR:

$$G_i(x) = \sum_{l=1}^{K} w_l g_l^i(x) = \sum_{l=1}^{K} w_l \frac{1}{\sigma_l^i \sqrt{2\pi}} \exp\left(-\frac{\left(x - \mu_l^i\right)^2}{2\sigma_l^{i2}}\right) \tag{26}$$

Here, $G_i(x)$ is the Gaussian Kernel to the i'th dimension of the solution and , $g_l^i(x)$ is the l'th sub-Gaussian function to the i'th dimension of the solution. $\mu_l^i$ and $\sigma_l^i$ are the i'th dimension mean value, and the i'th standard deviation to the l'th solution, respectively. Pheromone equation is:

$$\tau_{li(x)} = \frac{1}{\sigma_l^i\sqrt{2\pi}}\exp\left(-\frac{\left(x-\mu_l^i\right)^2}{2\sigma_l^{i2}}\right) \tag{27}$$

The equation provides the most relevant information to solve the objective function. This $ACO_R$ model requires many calculations for the right solution. Therefore, processors with high capability and speed are required in the ACO method. This situation increases the cost.

### *Grey Wolf Optimization (GWO)*

The GWO algorithm mimics the behaviours (hunting and leadership) of wild gray wolves and proposed in 2014 by Mirjalili et al [68]. There are four types of gray wolves in a wolfpack to mimic the leadership hierarchy. These are alpha (α), omega (ω), delta (δ), and beta (β). When designing the GWO, best to worse solutions are alpha, beta and delta, and omega, respectively. Gray wolves encircle a prey during hunting [69]. This behavior is expressed as

$$\vec{D} = \left|\vec{C}\cdot\vec{X}_p(t) - \vec{X}_p(t)\right| \tag{28}$$

$$\vec{X}(t+1) = \vec{X}_p(t) - \vec{A}\cdot\vec{D} \tag{29}$$

where t is the instant iteration, $\vec{D}$, $\vec{C}$ and $\vec{A}$ are the coefficients, $\vec{X}_p$ is the position of the prey, and $\vec{X}$ is the position of the gray wolf. $\vec{A}$ and $\vec{C}$ are calculated with the equations given below:

$$\vec{A} = 2\vec{a}\cdot\vec{r}_1 - \vec{a} \tag{30}$$

$$\vec{C} = 2\vec{r}_2 \tag{31}$$

The hunt is often led by leaders called alpha and occasionally followed by beta and delta. Thus, alpha is considered as the candidate solution with the best information of the prey location. Delta and omega take the role dealing the wounded members in the wolfpack. Gray wolves finish the hunt by attacking their prey when it gets stuck and stops [70].

The flowchart of the GWO MPPT method for the PV is shown in Fig. 18. For the number of gray wolves, namely the duty ratios, output power $P_{pv}$ is computed by the $V_{pv}$ and $I_{pv}$ measurements. When the MPP is found by the wolves, the correlated coefficient vectors turn into almost zero. In this algorithm duty cycle (D) is described as a grey wolf [71]. In this case, Equation (31) can be modified as given below:

$$D_i(k+1) = D_i(k) - A\cdot D \tag{32}$$

Thereby, the fitness function of the MPPT algorithm has been formulated as follows

$$P\left(D_i^k\right) > P\left(D_i^{k-1}\right) \tag{33}$$

where P, k, and i are the power, the number of iterations, and the number of present gray wolves, respectively.

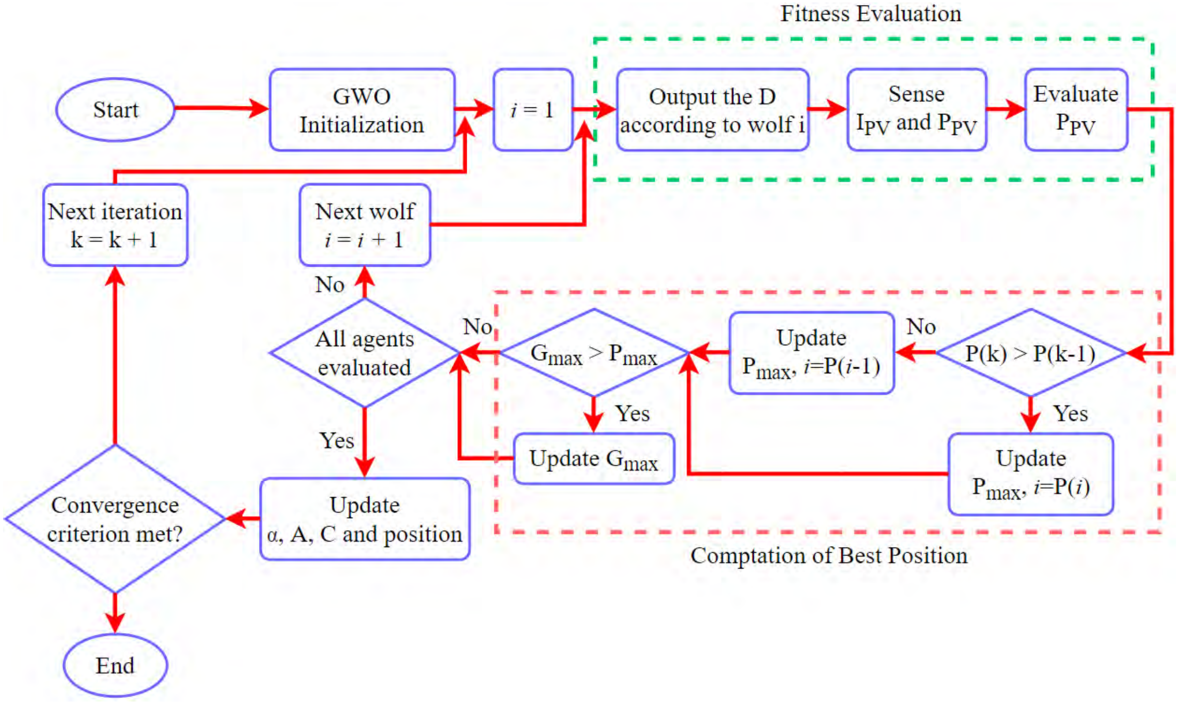

**Figure 18.** Grey wolf optimization flowchart

## RESULTS AND DISCUSSION

Numerous MPPT algorithms have been proposed to obtain maximum power and efficiency from the PV panel in years. These methods have many advantages and disadvantages. It is necessary to choose the optimum method for the PV system to be applied. Here, many parameters such as the atmospheric conditions of the region where the system will be installed, sunshine duration, and the budget allocated to the system should be taken into consideration. In this study, the most common methods were examined and compared with reference to certain parameters. Table 1 shows the comparison of the algorithms. While the comparison the major parameters such as speed, stability, cost, efficiency, etc considered into account. Here, 'V' refers to voltage, 'I' current, 'T' temperature sensor, 'A' analog, and 'D' digital.

MPPT methods can be classified by different names. There are different approaches in these classifications such as the characteristics of the method and the prevalence of use. Generally, they are divided into classes such as indirect, direct, intelligent, conventional methods etc. In the study, a new classification of the most used MPPT algorithms has been made by considering their dates of invention, complexity, and level of development, and is presented in Table 2.

1st generation methods are generally analog methods. These methods are easy to apply, low cost, low efficiency, and cannot track true MPPT. The most important advantage of these methods is that they can track MPP with acceptable speed and accuracy by low cost and fast setup.

**Table 2.** Classification of MPPT algorithms.

| Generation | Tracking Method |
|---|---|
| 1st Generation | Constant Voltage |
| | Fractional Open-Circuit Voltage |
| | Open-Circuit Voltage Pilot PV Cell |
| | Fractional Short-Circuit Current |
| | Look Up Table |
| | Load Current or Load Voltage Maximization |
| 2nd Generation | PV Output Senseless |
| | Perturb&Obsevre |
| | Three-Point Weight Comparison |
| | Hill Climbing |
| | On-Line MPP Search |
| | DC-Link Capacitor Drop Control |
| | Incremental Conductance |
| | Parasitic Capacitance |
| 3rd Generation | Fuzzy Logic Control |
| | Artificial Neural Networks |
| | Particle Swarm Optimization |
| | Ant Colony Optimization |
| | Grey Wolf Optimization |

**Table 1.** Comparison of MPPT algorithms.

| Tracking Method | Sensors | Stability | A/D | Speed | True MPPT | Cost | Efficiency | Ref |
|---|---|---|---|---|---|---|---|---|
| CV | V | Low | A | Mid | No | Low | Low | [72] |
| FOCV | V | Low | A | Mid | No | Low | Low | [73] |
| FOCVPVC | V | Low | A | Mid | No | Low | Low | [74] |
| FSCC | V | Low | A | Mid | No | Low | Low | [75] |
| LUT | T & I | Low | D | Mid | Maybe | Mid | Mid | [76] |
| LCLVM | V & I | Low | A | Low | No | Low | Low | [77] |
| POS | I | Low | D | Low | No | Low | Low | [78] |
| P&O | V & I | Low | A/D | Low | Yes | Mid | Mid | [79] |
| TPWC | V & I | Mid | D | Mid | Yes | Mid | Mid | [80] |
| HC | V & I | Mid | D | Low | Yes | Mid | Mid | [81] |
| OLMPP | V & I | Mid | D | Low | Yes | Mid | Mid | [82] |
| DCLC | V & I | Mid | D | Low | No | Low | Low | [83] |
| IncCond | V & I | Mid | D | Low | Yes | Mid | Mid | [84] |
| PC | V & I | Mid | D | Mid | Yes | High | Mid | [85] |
| FL | V & I | High | D | High | Yes | High | High | [21] |
| ANN | V & I | High | D | High | Yes | High | High | [86] |
| PSO | V & I | High | D | High | Yes | High | High | [87] |
| ACO | V & I | High | D | High | Yes | High | High | [88] |
| GWO | V & I | High | D | High | Yes | High | High | [89] |

2nd generation methods, the most widely used, are usually digital systems that require more than one sensor. In some methods of this generation, true MPPT can be achieved in medium level stability, speed, cost, and efficiency.

3rd generation methods, which especially emerged with the development of digital electronics, high-speed processors, and optimization theories, has quite high speed, complexity, stability, cost, and efficiency. For the successful implementation of these methods, it should be ensured that many iterations are made quickly, and the right decision is made. Therefore, it is necessary to use processors with high processing speed, but this also means an increase in cost.

## CONCLUSION

Considering the damage caused by fossil fuels to the environment, researches are carried out for cleaner energy resources. At this point, solar energy, which has an infinite source, also draws attention due to its eco friendliness. A great number of MPPT algorithms have been proposed in order to obtain maximum power and efficiency from PV panels. In this study, MPPT algorithms which are well accepted in the literature and widely used in the industry were examined and a detailed comparison table was presented. A new classification has been proposed for the analyzed MPPT algorithms. It is thought that this review can help in choosing the optimum algorithm for a PV system and can serve as a significant reference to future studies in this field.

## CONFLICT OF INTEREST

Authors approve that to the best of their knowledge, there is not any conflict of interest or common interest with an institution/organization or a person that may affect the review process of the paper.

## AUTHOR CONTRIBUTION

Omer Faruk Tozlu: Writing-review & editing, Methodology, Conseptualization. Huseyin Calik: Methodology, Conseptualization, Supervision.

## REFERENCES

1. Rabaia MKH, Abdelkareem MA, Sayed ET, Elsaid K, Chae KJ, Wilberforce T, et al. Environmental impacts of solar energy systems: A review. Sci Total Environ 2021;754:141989. https://doi.org/10.1016/j.scitotenv.2020.141989.
2. Motahhir S, El Hammoumi A, El Ghzizal A. The most used MPPT algorithms: Review and the suitable low-cost embedded board for each algorithm. J Clean Prod 2020;246:118983. https://doi.org/10.1016/j.jclepro.2019.118983.
3. Bahrami M, Zandi M, Gavagsaz R, Nahid-Mobarakeh B, Pierfederici S. A New Hybrid Method of MPPT for Photovoltaic Systems Based on FLC and Three Point-Weight Methods. Int. J. Adv. Sci. Technol., IEEE; 2016, p. 446–50.
4. Kumar M, Ban DK, Kim J. Photo-induced pyroelectric spikes for neuromorphic sensors. Mater Lett 2018;225:46–9. https://doi.org/10.1016/j.matlet.2018.04.106.
5. Lorenzo E. Solar electricity: engineering of photovoltaic systems. Earthscan/James & James; 1994.
6. Qi C, Ming Z. Photovoltaic Module Simulink Model for a Stand-alone PV System. Phys Procedia 2012;24:94–100. https://doi.org/10.1016/j.phpro.2012.02.015.
7. Kumar N, Hussain I, Singh B, Panigrahi BK. Framework of Maximum Power Extraction from Solar PV Panel Using Self Predictive Perturb and Observe Algorithm. IEEE Trans Sustain Energy 2018;9:895–903. https://doi.org/10.1109/TSTE.2017.2764266.
8. Motahhir S, El Hammoumi A, El Ghzizal A. Photovoltaic system with quantitative comparative between an improved MPPT and existing INC and P&O methods under fast varying of solar irradiation. Energy Reports 2018;4:341–50. https://doi.org/10.1016/j.egyr.2018.04.003.
9. Teshome DF, Lee CH, Lin YW, Lian KL. A modified firefly algorithm for photovoltaic maximum power point tracking control under partial shading. IEEE J Emerg Sel Top Power Electron 2017;5:661–71. https://doi.org/10.1109/JESTPE.2016.2581858.
10. Femia N, Petrone G, Spagnuolo G, Vitelli M. Power Electronics and Control Techniques for Maximum Energy Harvesting in Photovoltaic Systems. CRC Press, Taylor & Francis Group; 2017. https://doi.org/10.1201/b14303.
11. Christopher Iw, Assistant Professor S. Comparative Study of P&O and InC MPPT Algorithms. Am J Eng Res 2013;02:402–8.
12. Kota VR, Bhukya MN. A novel linear tangents based P&O scheme for MPPT of a PV system. Renew Sustain Energy Rev 2017;71:257–67. https://doi.org/10.1016/j.rser.2016.12.054.
13. Ishaque K, Salam Z, Lauss G. The performance of perturb and observe and incremental conductance maximum power point tracking method under dynamic weather conditions. Appl Energy 2014;119:228–36. https://doi.org/10.1016/j.apenergy.2013.12.054.
14. Wasynczuk O. Dynamic Behavior of a Class of Photovoltaic Power Systems. IEEE Trans Power Appar Syst 1983;PAS-102:3031–7.
15. Safari A, Mekhilef S. Simulation and hardware implementation of incremental conductance MPPT with direct control method using cuk converter. IEEE Trans Ind Electron 2011;58:1154–61. https://doi.org/10.1109/TIE.2010.2048834.
16. Elgendy MA, Zahawi B, Atkinson DJ. Assessment of the incremental conductance maximum power point tracking algorithm. IEEE Trans Sustain Energy 2013;4:108–17. https://doi.org/10.1109/TSTE.2012.2202698.
17. Tey KS, Mekhilef S. Modified incremental conductance MPPT algorithm to mitigate inaccurate responses under fast-changing solar irradiation level. Sol Energy 2014;101:333–42. https://doi.org/10.1016/j.solener.2014.01.003.
18. Shengqing L, Fujun L, Jian Z, Wen C, Donghui Z. An improved MPPT control strategy based on incremental conductance method. Soft Comput 2020;24:6039–46. https://doi.org/10.1007/s00500-020-04723-z.
19. Algarín CR, Giraldo JT, Álvarez OR. Fuzzy logic based MPPT controller for a PV system. Energies 2017;10. https://doi.org/10.3390/en10122036.
20. Bendib B, Krim F, Belmili H, Almi MF, Bolouma S. An intelligent MPPT approach based on neural-network voltage estimator and fuzzy controller, applied to a stand-alone PV system. IEEE Int.

Symp. Ind. Electron., IEEE; 2014, p. 404–9. https://doi.org/10.1109/ISIE.2014.6864647.

21. Yilmaz U, Kircay A, Borekci S. PV system fuzzy logic MPPT method and PI control as a charge controller. Renew Sustain Energy Rev 2018;81:994–1001. https://doi.org/10.1016/j.rser.2017.08.048.
22. Bollipo RB, Mikkili S, Bonthagorla PK. Critical Review on PV MPPT Techniques: Classical, Intelligent and Optimisation. IET Renew Power Gener 2020;14:1433–52. https://doi.org/10.1049/iet-rpg.2019.1163.
23. Joshi P, Arora S. Maximum power point tracking methodologies for solar PV systems – A review. Renew Sustain Energy Rev 2017;70:1154–77. https://doi.org/10.1016/j.rser.2016.12.019.
24. Bendib B, Belmili H, Krim F. A survey of the most used MPPT methods: Conventional and advanced algorithms applied for photovoltaic systems. Renew Sustain Energy Rev 2015;45:637–48. https://doi.org/10.1016/j.rser.2015.02.009.
25. Karami N, Moubayed N, Outbib R. General review and classification of different MPPT Techniques. Renew Sustain Energy Rev 2017;68:1–18. https://doi.org/10.1016/j.rser.2016.09.132.
26. Asim M, Tariq M, Mallick MA, Ashraf I. An improved constant voltage based MPPT technique for PMDC motor. Int J Power Electron Drive Syst 2016;7:1330–6. https://doi.org/10.11591/ijpeds.v7i4.pp1330-1336.
27. Ahmad J. A fractional open circuit voltage based maximum power point tracker for photovoltaic arrays. ICSTE 2010 - 2010 2nd Int. Conf. Softw. Technol. Eng. Proc., vol. 1, IEEE; 2010, p. 247–50. https://doi.org/10.1109/ICSTE.2010.5608868.
28. Enslin JHR, Wolf MS, Snyman DB, Swiegers W. Integrated photovoltaic maximum power point tracking converter. IEEE Trans Ind Electron 1997;44:769–73. https://doi.org/10.1109/41.649937.
29. Lopez-Lapeña O, Penella MT. Low-power FOCV MPPT controller with automatic adjustment of the sample&hold. Electron Lett 2012;48:1301–3. https://doi.org/10.1049/el.2012.1345.
30. Weddell AS, Merrett G V., Al-Hashimi BM. Ultra low-power photovoltaic MPPT technique for indoor and outdoor wireless sensor nodes. Proc. -Design, Autom. Test Eur. DATE, IEEE; 2011, p. 905–8. https://doi.org/10.1109/date.2011.5763302.
31. Sandali A, Oukhoya T, Cheriti A. Modeling and Design ofPV Grid Connected System Using a Modified Fractional Short-Circuit Current MPPT. 2014 Int. Renew. Sustain. Energy Conf., IEEE; 2014, p. 224–9. https://doi.org/10.1109/IRSEC.2014.7059859.
32. Masoum MAS, Dehbonei H, Fuchs EF. Theoretical and experimental analyses of photovoltaic systems with voltage and current-based maximum power point tracking. IEEE Trans Energy Convers 2004;19:652–3. https://doi.org/10.1109/TEC.2004.832449.
33. Sher HA, Murtaza AF, Noman A, Addoweesh KE, Al-Haddad K, Chiaberge M. A New Sensorless Hybrid MPPT Algorithm Based on Fractional Short-Circuit Current Measurement and P&O MPPT. IEEE Trans Sustain Energy 2015;6:1426–34. https://doi.org/10.1109/TSTE.2015.2438781.
34. Sankar M, Ramaprabha R. MODELLING AND SIMULATION OF MATLAB / SIMULINK BASED LOOKUP TABLE. ARPN J Eng Appl Sci 2013;8:948–53.
35. Kota VR, Bhukya MN. A simple and efficient MPPT scheme for PV module using 2-Dimensional lookup table. 2016 IEEE Power Energy Conf. Illinois, PECI 2016, IEEE; 2016, p. 2–8. https://doi.org/10.1109/PECI.2016.7459226.
36. Wang H, Vinayagam L, Jiang H, Cai ZQ, Ni Q, Li H. A new MPPT technique for the maximization of overall system output in solar generation. Proc Int Conf Power Electron Drive Syst 2015;2015-Augus:791–5. https://doi.org/10.1109/PEDS.2015.7203540.
37. Sanjeevikumar P, Grandi G, Wheeler PW, Blaabjerg F, Loncarski J. A simple MPPT algorithm for novel PV power generation system by high output voltage DC-DC boost converter. IEEE Int. Symp. Ind. Electron., vol. September, IEEE; 2015, p. 214–20. https://doi.org/10.1109/ISIE.2015.7281471.
38. Almutairi A, Abo-Khalil AG, Sayed K, Albagami N. MPPT for a PV grid-connected system to improve efficiency under partial shading conditions. Sustainability 2020;12:1–18. https://doi.org/10.3390/su122410310.
39. Kim SY, Park S, Jang SJ, Kim GH, Seo HR, Yu K. An effective POS MPPT control method for PV power generation system. Proc. - 12th Int. Conf. Electr. Mach. Syst. ICEMS 2009, IEEE; 2009, p. 1–6. https://doi.org/10.1109/ICEMS.2009.5382688.
40. Femia N, Petrone G, Spagnuolo G, Vitelli M. Optimization of perturb and observe maximum power point tracking method. IEEE Trans Power Electron 2005;20:963–73. https://doi.org/10.1109/TPEL.2005.850975.
41. Nedumgatt JJ, Jayakrishnan KB, Umashankar S, Vijayakumar D, Kothari DP. Perturb and observe MPPT algorithm for solar PV systems-modeling and simulation. Proc - 2011 Annu IEEE India Conf Eng Sustain Solut INDICON-2011 2011. https://doi.org/10.1109/INDCON.2011.6139513.
42. Sera D, Mathe L, Kerekes T, Spataru SV, Teodorescu R. On the perturb-and-observe and incremental conductance mppt methods for PV systems. IEEE J Photovoltaics 2013;3:1070–8. https://doi.org/10.1109/JPHOTOV.2013.2261118.
43. Femia N, Granozio D, Petrone G, Spagnuolo G, Vitelli M. Predictive & adaptive MPPT perturb and observe method. IEEE Trans Aerosp Electron Syst 2007;43:934–50. https://doi.org/10.1109/TAES.2007.4383584.
44. Piegari L, Rizzo R. Adaptive perturb and observe algorithm for photovoltaic maximum power point tracking. IET Renew Power Gener 2010;4:317–28. https://doi.org/10.1049/iet-rpg.2009.0006.
45. Abdelsalam AK, Massoud AM, Ahmed S, Enjeti PN. High-performance adaptive Perturb and observe MPPT technique for photovoltaic-based microgrids. IEEE Trans Power Electron 2011;26:1010–21. https://doi.org/10.1109/TPEL.2011.2106221.
46. Bahari MI, Tarassodi P, Naeini YM, Khalilabad AK, Shirazi P. Modeling and Simulation Of Hill Climbig MPPT Algorithm For Photovoltaic Application. Int. Symp. Power Electron. Electr. Drives, Autom. Motion, IEEE; 2016, p. 1041–4.
47. Xiao W, Dunford WG. A Modified Adaptive Hill Climbing MPPT Method for Photovoltaic Power Systems. 35th Annu. IEEE Power Electron. Spec. Conf., Aachen, Germany: 2004, p. 1957–63.
48. Altas IH, Sharaf AM. A Novel On-Line MPP Search Algorithm For PV Arrays. IEEE Trans Energy Convers 1996;11:748–54.
49. Kitano T, Matsui M, Xu D hong. Power sensor-less MPPT control scheme utilizing power balance at DC link system design to ensure stability and response. IECON Proc. (Industrial Electron. Conf., vol. 2, 2001, p. 1309–14. https://doi.org/10.1109/iecon.2001.975971.
50. Shi Y, Li R, Xue Y, Li H. High-frequency-link-based grid-tied PV system with small DC-link capacitor and low-frequency ripple-free maximum power point tracking. IEEE Trans Power Electron 2016;31:328–39. https://doi.org/10.1109/TPEL.2015.2411858.
51. Mei Q, Shan M, Liu L, Guerrero JM. A novel improved variable step-size incremental-resistance MPPT method for PV systems. IEEE Trans Ind Electron 2011;58:2427–34. https://doi.org/10.1109/TIE.2010.2064275.
52. Lee JH, Bae HS, Cho BH. Advanced incremental conductance MPPT algorithm with a variable step size. EPE-PEMC 2006 12th Int. Power Electron. Motion Control Conf. Proc., 2007, p. 603–7. https://doi.org/10.1109/EPEPEMC.2006.283227.

53. Brambilla A, Gambarara M, Garutti A, Ronchi F. New approach to photovoltaic arrays maximum power point tracking. PESC Rec - IEEE Annu Power Electron Spec Conf 1999;2:632–7. https://doi.org/10.1109/PESC.1999.785575.
54. Takashima T, Tadayoshi T, Amano M, Ando Y. Maximum Output Control of Photovoltaic (PV) Array. Collect. Tech. Pap. 35th Intersoc. Energy Convers. Eng. Conf. Exhib., 2000, p. 380–3.
55. Spiazzi G, Buso S, Mattavelli P. Analysis of MPPT algorithms for photovoltaic panels based on ripple correlation techniques in presence of parasitic components. 2009 Brazilian Power Electron Conf COBEP2009 2009:88–95. https://doi.org/10.1109/COBEP.2009.5347738.
56. Al Nabulsi A, Dhaouadi R. Efficiency optimization of a dsp-based standalone PV system using fuzzy logic and dual-MPPT control. IEEE Trans Ind Informatics 2012;8:573–84. https://doi.org/10.1109/TII.2012.2192282.
57. Algazar MM, Al-Monier H, El-Halim HA, Salem MEEK. Maximum power point tracking using fuzzy logic control. Int J Electr Power Energy Syst 2012;39:21–8. https://doi.org/10.1016/j.ijepes.2011.12.006.
58. Messalti S, Harrag AG, Loukriz AE. A new neural networks MPPT controller for PV systems. 2015 6th Int. Renew. Energy Congr. IREC 2015, IEEE; 2015. https://doi.org/10.1109/IREC.2015.7110907.
59. Ocran TA, Cao J, Cao B, Sun X. Artificial neural network maximum power point tracker for solar electric vehicle. Tsinghua Sci Technol 2005;10:204–8. https://doi.org/10.1016/S1007-0214(05)70055-9.
60. Heidari M. Improving efficiency of photovoltaic system by using neural network MPPT and predictive control of converter. Int J Renew Energy Res 2016;6:1524–9.
61. Ramaprabha R, Mathur BL, Sharanya M. Solar array modeling and simulation of MPPT using neural network. 2009 Int. Conf. Control Autom. Commun. Energy Conserv. INCACEC 2009, IEEE; 2009, p. 1–5.
62. de Oliveira FM, Oliveira da Silva SA, Durand FR, Sampaio LP, Bacon VD, Campanhol LBG. Grid-tied photovoltaic system based on PSO MPPT technique with active power line conditioning. IET Power Electron 2016;9:1180–91. https://doi.org/10.1049/iet-pel.2015.0655.
63. Renaudineau H, Donatantonio F, Fontchastagner J, Petrone G, Spagnuolo G, Martin JP, et al. A PSO-based global MPPT technique for distributed PV power generation. IEEE Trans Ind Electron 2015;62:1047–58. https://doi.org/10.1109/TIE.2014.2336600.
64. Dorigo M, Maniezzo V, Colorni A. Ant system: Optimization by a colony of cooperating agents. IEEE Trans Syst Man, Cybern Part B Cybern 1996;26:29–41. https://doi.org/10.1109/3477.484436.
65. Dorigo M, Birattari M, Stützle T. Ant colony optimization. IEEE Comput Intell Mag 2006:28–39. https://doi.org/10.4249/scholarpedia.1461.
66. Satheesh Krishnan G, Kinattingal S, Simon SP, Nayak PSR. MPPT in PV systems using ant colony optimisation with dwindling population. IET Renew Power Gener 2020;14:1105–12. https://doi.org/10.1049/iet-rpg.2019.0875.
67. Titri S, Larbes C, Toumi KY, Benatchba K. A new MPPT controller based on the Ant colony optimization algorithm for Photovoltaic systems under partial shading conditions. Appl Soft Comput J 2017;58:465–79. https://doi.org/10.1016/j.asoc.2017.05.017.
68. Mirjalili S, Mirjalili SM, Lewis A. Grey Wolf Optimizer. Adv Eng Softw 2014;69:46–61. https://doi.org/10.1016/j.advengsoft.2013.12.007.
69. Eshak MM, Khafagy MA, Makeen P, Abdellatif SO. Optimizing the performance of a stand-alone PV system under non-uniform irradiance using Gray-Wolf and hybrid neural network AI-MPPT algorithms. 2nd Nov. Intell. Lead. Emerg. Sci. Conf. NILES 2020, 2020, p. 600–5. https://doi.org/10.1109/NILES50944.2020.9257965.
70. Tjahjono A, Anggriawan DO, Habibi MN, Prasetyono E. Modified grey wolf optimization for maximum power point tracking in photovoltaic system under partial shading conditions. Int J Electr Eng Informatics 2020;12:94–104. https://doi.org/10.15676/ijeei.2020.12.1.8.
71. Guo K, Cui L, Mao M, Zhou L, Zhang Q. An Improved Gray Wolf Optimizer MPPT Algorithm for PV System with BFBIC Converter under Partial Shading. IEEE Access 2020;8:103476–90. https://doi.org/10.1109/ACCESS.2020.2999311.
72. Lasheen M, Rahman AKA, Abdel-Salam M, Ookawara S. Performance Enhancement of Constant Voltage Based MPPT for Photovoltaic Applications Using Genetic Algorithm. Energy Procedia 2016;100:217–22. https://doi.org/10.1016/j.egypro.2016.10.168.
73. Huang YP, Hsu SY. A performance evaluation model of a high concentration photovoltaic module with a fractional open circuit voltage-based maximum power point tracking algorithm. Comput Electr Eng 2016;51:331–42. https://doi.org/10.1016/j.compeleceng.2016.01.009.
74. Baimel D, Tapuchi S, Levron Y, Belikov J. Improved fractional open circuit voltage MPPT methods for PV systems. Electron 2019;8:1–20. https://doi.org/10.3390/electronics8030321.
75. Sher HA, Murtaza AF, Noman A, Addoweesh KE, Chiaberge M. An intelligent control strategy of fractional short circuit current maximum power point tracking technique for photovoltaic applications. J Renew Sustain Energy 2015;7. https://doi.org/10.1063/1.4906982.
76. Ilyas A, Khan MR, Ayyub M. Lookup Table Based Modeling and Simulation of Solar Photovoltaic System. 2015 Annu. IEEE India Conf., IEEE; 2015, p. 14–9.
77. Zhang L, Wang Z, Cao P, Zhang S. A maximum power point tracking algorithm of load current maximization-perturbation and observation method with variable step size. Symmetry (Basel) 2020;12:1–16. https://doi.org/10.3390/sym12020244.
78. Lee SJ, Park HY, Kim GH, Seo HR, Ali MH, Park M, et al. The experimental analysis of the gridconnected PV system applied by POS MPPT. Proceeding Int. Conf. Electr. Mach. Syst. ICEMS 2007, 2007, p. 1786–91. https://doi.org/10.1109/ICEMS.2007.4412095.
79. Killi M, Samanta S. Modified perturb and observe MPPT algorithm for drift avoidance in photovoltaic systems. IEEE Trans Ind Electron 2015;62:5549–59. https://doi.org/10.1109/TIE.2015.2407854.
80. Roy CP, Naick BK, Shankar G. Modified three-point weight comparison method for adaptive MPPT of photovoltaic systems. IET Conf. Publ., vol. 2013, 2013, p. 146–56. https://doi.org/10.1049/cp.2013.2184.
81. Liu F, Kang Y, Yu Z, Duan S. Comparison of P&O and Hill Climbing MPPT Methods for Grid-Connected PV Converter. 2008 3rd IEEE Conf. Ind. Electron. Appl. ICIEA 2008, 2008, p. 804–7. https://doi.org/10.1109/ICIEA.2008.4582626.
82. Altas IH, Sharaf AM. A Novel Photovoltaic On-Line Search Algorithm for Maximum Energy Utilization. Int. Conf. Commun., Oman: Computer and Power (ICCCP'07); 2007, p. 192–7.
83. Shi Y, Liu L, Li H, Xue Y. A single-phase grid-connected PV converter with minimal DC-link capacitor and low-frequency ripple-free maximum power point tracking. 2013 IEEE Energy Convers. Congr. Expo. ECCE 2013, IEEE; 2013, p. 2385–90. https://doi.org/10.1109/ECCE.2013.6647006.
84. Tey KS, Mekhilef S. Modified incremental conductance algorithm for photovoltaic system under partial shading conditions and load variation. IEEE Trans Ind Electron 2014;61:5384–92. https://doi.org/10.1109/TIE.2014.2304921.

85. Hohm DP, Ropp ME. Comparative study of maximum power point tracking algorithms. Prog Photovoltaics Res Appl 2003;11:47–62. https://doi.org/10.1002/pip.459.
86. Messalti S, Harrag A, Loukriz A. A new variable step size neural networks MPPT controller: Review, simulation and hardware implementation. Renew Sustain Energy Rev 2017;68:221–33. https://doi.org/10.1016/j.rser.2016.09.131.
87. Ishaque K, Salam Z, Amjad M, Mekhilef S. An improved particle swarm optimization (PSO)-based MPPT for PV with reduced steady-state oscillation. IEEE Trans Power Electron 2012;27:3627–38. https://doi.org/10.1109/TPEL.2012.2185713.
88. Jiang LL, Maskell DL, Patra JC. A novel ant colony optimization-based maximum power point tracking for photovoltaic systems under partially shaded conditions. Energy Build 2013;58:227–36. https://doi.org/10.1016/j.enbuild.2012.12.001.
89. Mohanty S, Subudhi B, Ray PK. A Grey Wolf-Assisted Perturb & Observe MPPT Algorithm for a PV System. IEEE Trans Energy Convers 2017;32:340–7. https://doi.org/10.1109/TEC.2016.2633722.

Hittite Journal of Science and Engineering, 2021, 8 (3) 221–231
ISSN NUMBER: 2148–4171
DOI: 10.17350/HJSE19030000232

# An Experimental and Numerical Evaluation of Seal Strictness on Ball Bearing Performance

**Zafer Ozdemir** **Osman Selim Turkbas** **Kaan Sarigoz**
Gazi University, Department of Mechanical Engineering, Ankara, Turkey

*Article History:*
*Received: 2021/03/03*
*Accepted: 2021/08/11*
*Online: 2021/09/29*

***Correspondence to**: Zafer Özdemir;*
*e-mails: krebnatlazafer@gmail.com,*
*ozdemirzafer@yahoo.com;*

## ABSTRACT

Rubber-based ball bearing seals are widely used in the bearing industry. These seals affect the performance of the ball bearings and endurance life as well. Effect of rolling bearing seal strictness value on bearing performance was investigated experimentally and numerically in this study. Four different seal strictness rolling bearing samples were manufactured for the tests. The bearing seal strictness which is used in tests are given respectively; 200 µm, 160 µm, 105 µm, 45 µm and contactless. First; friction torque test was performed without loading and bearings were rotated at 3000 rpm for one hour. Temperature values and friction generation in bearings against rotation were measured throughout the tests. Second; temperature tests have been carried out; roll bearings were rotated at 6000 rpm for one hour and 2000 N radial load was applied to samples. 5 samples for each test have been used. The contact reaction force between the region of inner ring and rubber seal inner lip was modeled by means of the finite element method and designed in ANSYS Workbench. ANSYS results and friction moment test results have been evaluated and compared. It is observed that as the strictness increases, the friction force and temperature increase, but this affects the life cycle of ball bearing negatively. It has been seen that the numeric results are consistent with the test results.

**Keywords:**
Ball bearing; Rubber seal; Friction torque; Strictness; Nitrile based rubbers (NBR); Finite element analysis; Ansys

## INTRODUCTION

The basic working principle of a ball bearing is to reduce the friction force to a minimum and to make load transfer between two relative rotating mechanisms. The ball bearings are used among a variety of mechanisms such as shaft, axis, pumps, heavy load machines, wind turbines, and machine tools [1].

The friction force produced by ball bearings determines the heat amount produced. Friction force arises from the loads applied to ball-bearing, type and size of ball-bearing, operating cycle, lubricant properties. The total reaction force against the rotation force inside ball-bearing includes sliding and rolling friction force at contact areas, the friction force between rolling elements and rolling paths, the friction force between rolling elements and the cage. Friction occurs because of lubricant movements and contact covers [2].

A ball bearing seal has 2 basic tasks; the lubricant in and keeping contaminates out of the bearing system. This separation must be accomplished between surfaces in relative motion, usually a shaft or bearing inner ring and a housing [3].

## LITERATURE REVIEW

Considerable studies have been made on the rolling bearing, cage and seal strictness relation by now. Some of the notable ones have been discussed below.

T.Sada and his colleagues examined friction loss reduction of ball bearings [4]. Ł.Gorycki and his colleagues analyzed the impact of the cage type on the frictional moment of ball bearings and showed that the type of cage used in ball bearings has a significant impact on the frictional moment [5]. B.Choe and his colleagues investigated the dynamic behavior of ball bearing cage (polytetrafluoroethylene (PTFE) cages are used as solid lubricants in such environments) in cryogenic environments and suggested (PTFE) cages [6]. Y.Cui and his colleagues investigated the vibration effect analysis of ball dynamic unbalance on the cage of high-speed cylindrical ball bearing and concluded that the increase of the radial load of the bearing, to a certain extent, can reduce the vibration of cage considering the ball dynamic unbalance [7]. Z.Yang and his colleagues presented

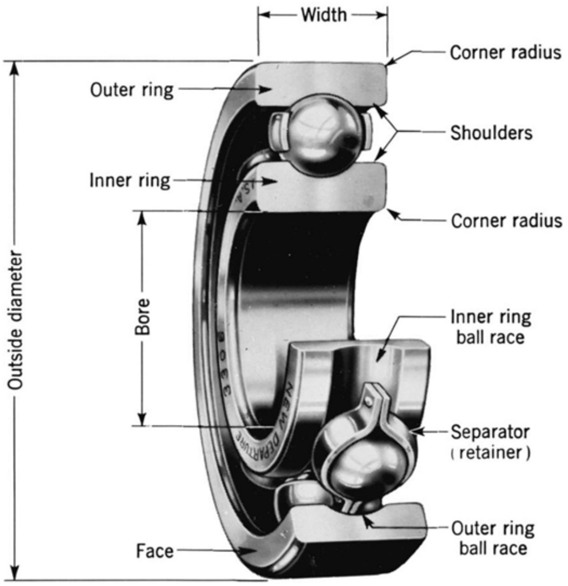

**Figure 1.** Nomenclature of a ball bearing. [1]

**Figure 2.** Components of a ball bearing [2]

a five degree-of-freedom (5-DOF) quasi-dynamic model to analyze the relationship between the cage clearance and heating characteristics. The results show that there is a critical value for both the guide and pocket hole clearance and that the heating is obviously decreased and gradually stabilizes when the clearance exceeds a critical value [8]. M.Takimoto and his colleagues introduced the development of automotive wheel bearing seals (Muddy-water resistant seal, low temperature environment seal and super low-torque seal) [9].

As the literature has been gone through, it has been seen that there is not adequate research on the seal strictness versus ball bearing performance and FEA analyze of seal strictness. This makes this study an original one in the ball bearing performance in terms of seal strictness and FEA-ANSYS field.

As friction force increases, ball bearing life decreases [4]. Theoretically, we have 2 main equations to calculate the friction force [10]. One of them is the Palmgren method [11]. According to this method, the friction force is calculated below;

$$M = M_0 + M_1 \text{ if } v \times n \geq 2000 \text{ then;} \quad (1)$$

$$M_0 = 10^{-7}.f_0\left(v \times n\right)^{2/3}.dm^3 \text{ if } v \times n < 2000 \text{ then} \quad (2)$$

$$M_0 = 1{,}6.10^{-5}.f_0.dm^3 \quad (3)$$

$$M_1 = f_1.P_1.dm \quad (4)$$

$$f_1 = z\left(F_s/C_s\right)y \quad (5)$$

$F_s$ equivalent statical load and $C_s$ are statically load number, z and y values are presented at table 1. [6].

**Table 1.** Coefficients according to the bearing types to calculate f1

| Rolling Bear Type | Nominal Contact Angle [°] | z | y |
|---|---|---|---|
| Deep Groove Ball Bearing | 0 | 0,0004-0,0006 | 0,55 |
| Angular Contact Ball Bearing | 30-40 | 0,001 | 0,33 |
| Axial Contact Ball Bearing | 90 | 0,0008 | 0,33 |
| Self-Aligning Ball Bearing | 10 | 0,0003 | 0,40 |

M: Total friction moment (Nmm.)
$M_0$: Oiling friction moment (Nmm.)
$M_1$: Load friction moment (Nmm.)
n: Cycle (rpm)
v: Kinematic viscosity of oil ($m^2/s$)
$f_0$: Ball bearing coefficient
dm: Ball bearing mean diameter (mm.)
$f_1$: Coefficient according to the bearing type and load
$P_1$: Load (N)

Friction moment calculation according to the SKF Company [11];

$$M = M_{rr} + M_{sl} + M_{seal} + M_{drag} \quad (6)$$

M: Total friction moment (Nmm.)
$M_r$: Radial friction moment (Nmm.)
$M_{sl}$: Sliding friction moment (Nmm.)
$M_{seal}$: Seal friction moment (Nmm.)
$M_{drag}$: Dragging friction moment (Nmm.) (oil, grease, and reaction against force and rolling)

Mathematical equations consider some variables affecting friction moment; however, cage design, cover strictness, bearing rolling ways, radius values, rolling way roughness affect friction moment. Therefore, it is necessary to conduct experimental studies to ensure the best performance of ball bearings life cycle.

Ball bearings are used with rubber-based seals, iron-plate based seals and without seals. No maintenance is required for rubber-based and iron-plate based seals for a lifetime [3,12].

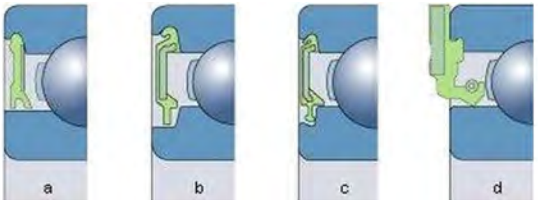

**Figure 3.** Some rubber-based seals design comprehensively used in SKF Company

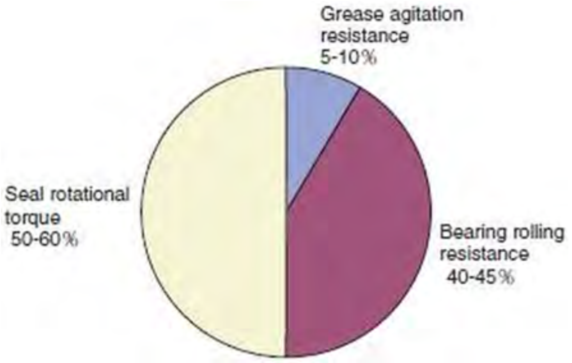

**Figure 4.** The effect of friction torque at a ball bearing [11]

There are some types of rubber-based seals used in ball bearings. Below are some of them presented comprehensively used in the SKF Company [11].

As seen in Fig 4, most of the friction torque arises from the seal cage rotational torque. The %50-60 of friction in ball bearing is caused approximately from seal rotational torque, %40-45 from bearing rolling resistance and %5-10 from grease agitation resistance [3,11]. According to the data, the great part of the friction is caused from seals.So, the design of seal is an important parameter for ball bearing manufacture.

At higher cycles; iron plate-based seals and contact-free rubber-based seals have advantages on performance. However, it is better to use rubber-based seals if tightness is desired.

## MATERIALS AND METHOD

### Experimental Study

Reaction and performance of rubber-based seals having different strictness values have been examined using the experimental setup as seen in Fig 5. Radial 6008 2RSR ball bearing is used in tests (Fig 6).

The tests aim to investigate and determine the effect of seal strictness on the performance of bearing and to measure the bearing life theoretically. Special fabricated rubber-based seals at different strictness have been used in 6008 2RSR ball bearings.

Two different types of tests have been conducted; 1) friction moment-time, 2) temperature-time tests.

The outer ring of the ball bearing was fixed to the outer side of the shaft with a screw, and the inner ring was mounted to the shaft. Screw transmits the force to the load cell. The friction moment could be calculated by the load cell via this connection as seen in figure 5. X is 20 cm (200 mm.)

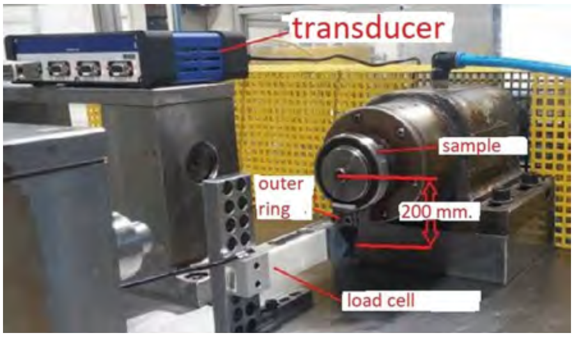

**Figure 5.** Experimental setup

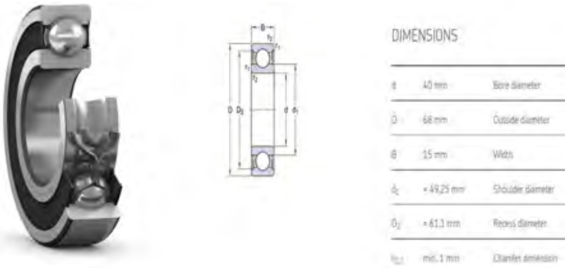

**Figure 6.** Radial 6008 2RSR ball bearing and dimensions used in tests [11]

$$M = F.X \tag{7}$$

M: Friction moment (Nm.)
F: Force (N.)
X: distance (m.)

Before tests; 1) Bolt and nut tightness of the setup has been controlled 2) Radial gap is not allowed in the samples and 3) Roller bearing samples are manually rotated to control the setup.

### Preparation of Rubber-Based Seals (RSR-Rubber Seal Radial) Having Different Strictness

Seal strictness is the measure of the stress of this seal to the inner ring of the ball bearing to provide. oil tightness. As the strictness value increase, the tightness increase [12] and [13].

NBR (Nitrile Based Rubbers) have been used in our experimental studies. NBR are copolymers of butadiene and acrylonitrile. The term has also been applied to copolymers of other dienes and/or nitriles. Acrylonitrile content may range from 18-50%. Increasing acrylonitrile content leads to higher hardness, strength, abrasion resistance, heat resistance, and oil/fuel resistance and lower resilience and low-temperature flexibility [14]. The enduring temperature range is between -40°C and 110°C [14].

Half section view of ball bearing used in experiments is shown in Fig. 7. As seen in detail-A, it could be seen what a seal strictness is. It is easier to adjust the strictness at radial ball bearings because machining tolerance is lower since the

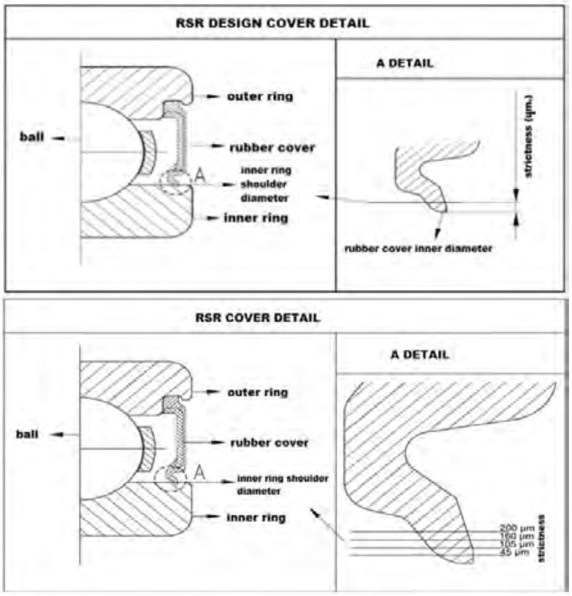

**Figure 7.** The strictness of seals and the values used in tests of Radial 6008 2RSR ball bearing

inner ring shoulder was machined at a grinding machine, not at a lathe.

The sensitivity of the measuring device is 0,05µm. (Fig. 8.)

The measurements have been conducted by optical and laser measuring method; optical camera laser measurement device (Fig. 9.) scale resolution is 0,1µm.

Seal strictness design calculation is presented below:

Seal Strictness [µm]= Inner ring shoulder diameter–Radial seal inner diameter (8)

Inner ring shoulder diameter: 100 mm.

Radial seal inner diameter: 99,8 mm.

Seal strictness: 100 – 99,8 = 200 µm

Seal strictness in radius: 100µm (Seal strictness worked out in this study are based on mostly mentioned in real-life usage of ball bearings.) Seal strictness values of inner ring shoulder diameter and radial seal inner diameter for all test samples of ball bearings were measured exactly %100 with ±10 µm tolerance. Each seal strictness group has 5 samples.

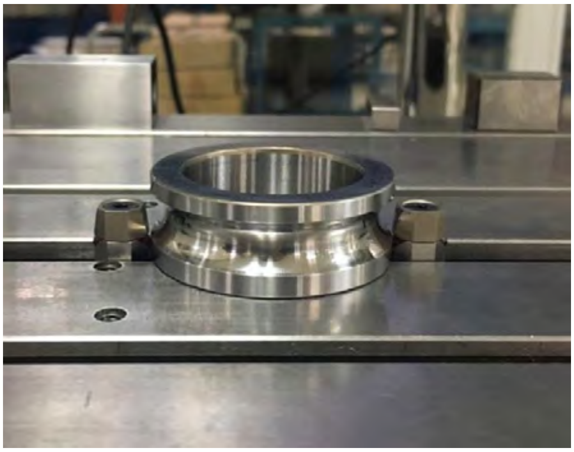

**Figure 8.** Measuring the diameter of the inner ring

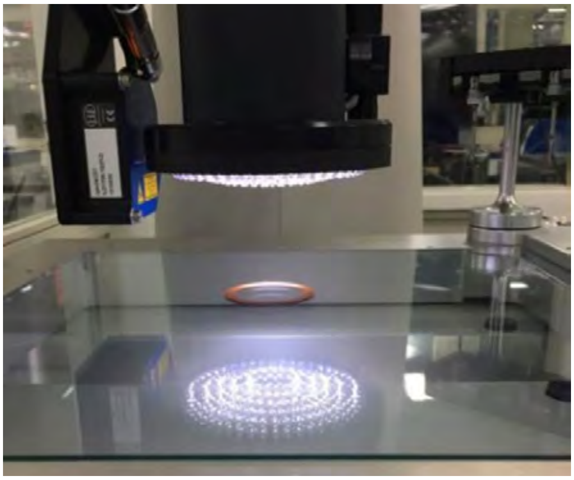

**Figure 9.** Measuring the inner diameter of the rubber-based seal

**Table 2.** Seal Strictness Values of Specially Fabricated Cages [µm]

| *Sample Number* | *200 µm* | *160 µm* | *105 µm* | *45 µm* | *Contactless* |
|---|---|---|---|---|---|
| *1* | *201,7* | *161,8* | *113,2* | *42,7* | - |
| *2* | *203,7* | *156,8* | *102,7* | *43,1* | - |
| *3* | *208* | *159,2* | *103,7* | *38,3* | - |
| *4* | *197,8* | *165,4* | *103,1* | *40,1* | - |
| *5* | *200,3* | *158,7* | *115,1* | *43,5* | - |
| *Mean Value [µm]* | *202,3* | *160,4* | *107,6* | *41,5* | - |

The values indicated in table 2 are the seal strictness values of specially fabricated rubber seal values. 5 different groups have been fabricated and the mean values are taken as respectively 200, 160, 105 and 45 µm for calculation. After the heat treatment process, rolling bearings' last fabrication process has been carried out at and the rubber seals are mounted then. A very sensitive process has been carried out as seen in Fig. 8.and 9.

## Test Conditions

Specifications of ball bearings used in tests are detailed in table 3 below:

**Table 3.** Specifications of ball bearings

| *Rolling Bearing Used* | *6008 2RSR* |
|---|---|
| *Cover Type* | *Radial Sealing Element* |
| *Rubber/Seal Cover Material* | *NBR* |
| *Quantity of Grease Oil* | *% 30 of Rolling Bearing Inner Volume* |
| *Radial Gap* | *C3* |
| *Cage Type* | *J* |
| *Rolling Bearing Cover Strictness* | *200 µm* |
| | *160 µm* |
| | *105 µm* |
| | *45 m* |
| | *0 - contactless* |

In temperature test; The aim is to investigate the effect of temperature on the seal strictness at 6000 rpm and 2000 N radial load.

The tests have been conducted according to the ASTM G182 – 13 (2018) “Standard Test Method for Determination of the Breakaway Friction Characteristics of Rolling Element Bearings” [15] and DIN 51819-1 2016 Edition, December 2016 “Testing of lubricants - Mechanical-dynamic testing in the roller bearing test apparatus FE8 - Part 1: General working principles” [16].

**Table 4.** Test Conditions

| *Test Conditions* | *Friction Moment Test* | *Temperature Test* |
|---|---|---|
| *Cycle (RPM)* | *3000* | *6000* |
| *Radial Force (N.)* | *-* | *2000* |
| *Time (min.)* | *60* | *60* |
| *Inner Ring* | *rotating* | *rotating* |
| *Outer Ring* | *fixed* | *fixed* |
| *Data Collection* | *1 Hz.* | *60 Hz.* |

# EXPERIMENTAL RESULTS

The results that have been given are the mean values of the collected data through the tests.

## Friction Moment Test

### *Friction Moment–Time*

Friction moment versus time values of 200µm. seal strictness samples have been observed as seen in Fig. 10. Starting torque is greater, but as the steady state occurs the torque decreases. Approximately, at the 300th second, the steady state begins. The mean friction value has been observed between 0,115 Nm.(number 4 sample) and 0,156 Nm. (number 2 sample).

Friction moment versus time values of 160µm. seal strictness samples have been observed in Fig. 11. Starting torque is greater, but approximately, at the 300th second, the steady state begins. The mean friction value has been observed between 0,093 Nm. (number 2 sample) and 0,118 Nm. (number 4 sample).

Friction moment versus time values of 105µm. seal strictness samples have been observed in Fig. 12. Starting torque is greater, but approximately, at the 600th second, the steady state begins. The mean friction value has been observed between 0,060 Nm. (number 4 sample) and 0,088 Nm. (number 1 sample).

Friction moment versus time values of 45µm. seal strictness samples have been observed in Fig. 13. Starting torque is greater, but approximately, at the 300th second, the steady state begins. The mean friction value has been obser-

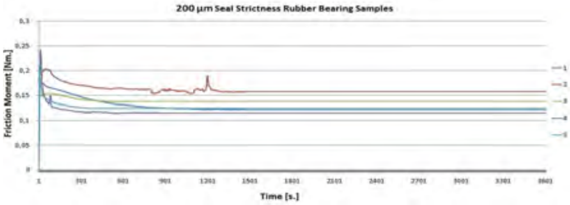

**Figure 10.** Friction moment values of 200µm. seal strictness according to time (5 samples)

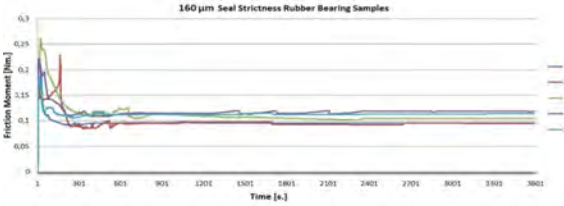

**Figure 11.** Friction moment values of 160µm. seal strictness according to time (5 samples)

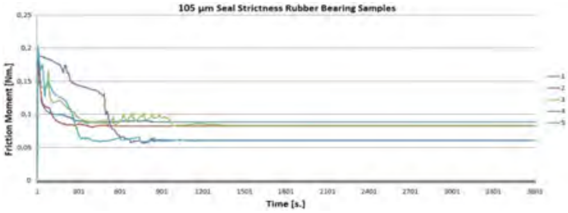

**Figure 12.** Friction moment values of 105µm. seal strictness according to time (5 samples)

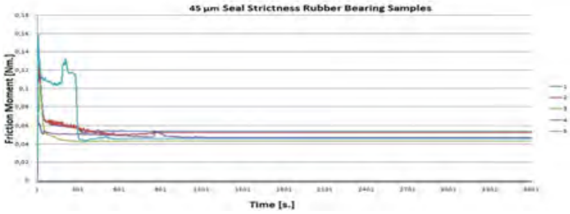

**Figure 13.** Friction moment values of 45µm. seal strictness according to time (5 samples)

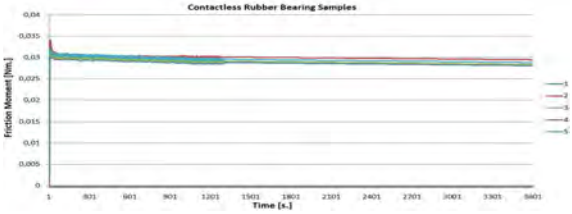

**Figure 14.** Friction moment values of contactless rubber bearings according to time (5 samples)

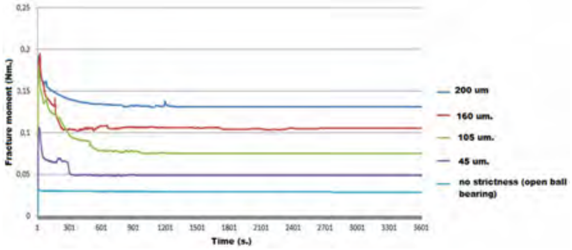

**Figure 15.** Mean friction values of different seal strictness according to time

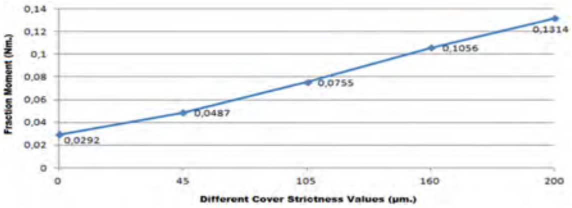

**Figure 16.** Different seal strictness; mean friction values

ved between 0,043 Nm. (number 3 sample) and 0,054 Nm. (number 1 sample).

A more stable graphic is observed for the contactless rubber bearings as seen in Fig. 14. The mean friction value has been observed between 0,0282 Nm. (number 1 sample) and 0,0295 Nm. (number 2 sample).

Mean friction moment results have been shown in Fig. 16. As the seal strictness increases, friction moment increases linearly. Ball bearing has been tested without any load, so the effect of strictness could be determined obviously. The last 50 min. friction moment values have been considered, not at first 10 min. values. Mean friction moment values have been given according to different seal strictness at table 5.

**Table 5.** Friction moment results collected of different seal strictness

| | *Mean friction moment values [Nm]* | | |
|---|---|---|---|
| *Ball bearings according to the seal strictness* | *1 hour* | *First 10 minutes* | *Last 50 minutes* |
| *200 µm* | *0,1334* | *0,1435* | *0,1314* |
| *160 µm* | *0,1076* | *0,1176* | *0,1056* |
| *105 µm* | *0,0806* | *0,1059* | *0,0755* |
| *45 µm* | *0,0504* | *0,0591* | *0,0487* |
| *0 µm* | *0,0293* | *0,0299* | *0,0292* |

## Temperature Test

Temperature change according to time has been observed at temperature tests. The specifications of the rolling bearing used in tests are shown in table 2. The same samples are used as in friction tests. 2000 N. Radial load is applied and 6000 rpm cycle has been carried out as shown in table 6.

**Table 6.** Temperature Pre-Test Values

| *Cycle (rpm.)* | *6000* |
|---|---|
| *Radial Load (N.)* | *2000* |
| *Test Duration (min.)* | *60* |
| *Inner Ring* | *Rotating* |
| *Outer Ring* | *Fixed* |
| *Temperature Data Collection Frequency (Hz.)* | *1/30* |

The test aims to observe and evaluate the effect of seal strictness values differences. According to the obtained values, the life cycle of ball bearings (rolling bearings) and real life cycle of ball bearings will be calculated according to the ISO 281:2007 (Rolling Bearings - Dynamic Load Ratings and Rating Life) [17].

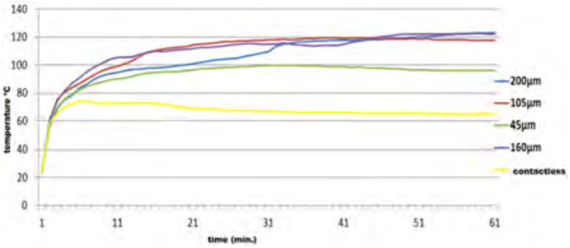

**Figure 17.** Different seal strictness; time versus temperature

The ambient temperature is 20°C. Measurement frequency is 1/30 Hz and the total test time is 60 min. A sensitive probe touching to the outer ring of rolling bearings measures the temperature.

Mean temperature values according to time have been shown in Fig. 17. As the seal strictness increases, friction moment increases and henceforth temperature increases; but temperature values become steady almost after 12 minutes. 200 µm, 160 µm and 105 µm seal strictness ball bearings temperature values are almost the same after a steady state after 41 minutes.

The temperature test results have been shown in table 7. As seen in Table 7, we need 30 minutes to be sure and obtain accurate data. After 30 minutes; the effect of strictness versus temperature could be seen obviously.

**Table 7.** Temperature test results.

| *Different seal strictness* | *Mean temperature values Last 30 minutes(°C)* | *Maximum temperature values (°C)* |
|---|---|---|
| *200 µm* | *118,9* | *150* |
| *160 µm* | *118,9* | *145* |
| *105 µm* | *118,6* | *132,5* |
| *45 µm* | *97,8* | *104* |
| *0 µm* | *65,7* | *67* |

Temperature (max. and mean values) versus seal strictness values have been observed as seen in Fig. 18. Temperature does not change at 105 µm, 160 µm and 200 µm strictness after the steady-state begins. The mean temperature value is approximately 119°C. The contactless rolling bearing is 65,7°C and 45 µm strictness is 97,8°C.

According to the temperature test results having 6000 rpm and 2000 N. load, after a value bigger than 105 µm, temperatures are the same. So it can be concluded that smaller seal strictness values than 105 µm should be preferred for fewer temperature degrees.

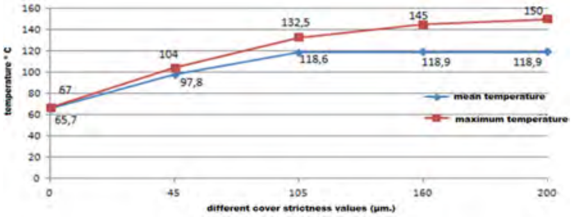

**Figure 18.** Seal strictness; mean and max. temperatures

**Table 8.** Temperature Test Values

| Seal Strictness | Mean Temperature, Last 30.min. (°C) | The ratio of mean temperature to a minimum temperature | Maximum Rolling Bearing Temperature (°C) | The ratio of mean temperature to maximum temperature |
|---|---|---|---|---|
| 200 µm | 118,9 | 118,9/65,7=1,81 | 150 | 150/67=2,23 |
| 160 µm | 118,9 | 118,9/65,7=1,81 | 145 | 145/67=2,16 |
| 105 µm | 118,6 | 118,6/65,7=1,80 | 132,5 | 132,5/67=1,97 |
| 45 µm | 97,8 | 97,8/65,7=1,48 | 104 | 104/67=1,55 |
| contactless | 65,7 | 1 | 67 | 1 |

Mean and maximum temperature values are shown in table 8.

## Calculating of Ball Bearing Life Theoretically According to the Temperature Test Results

The life cycle of ball bearings (rolling bearings) is standardized according to the ISO 281:2007 (Rolling Bearings - Dynamic Load Ratings and Rating Life) [17].

$$L_{10} = (C_r / P_r)^3 \qquad (9)$$

Here in this equation;

$C_r$: Basic Dynamic Radial Load Rating [Newton]
$P_r$: Dynamic Equivalent Radial Load [Newton]
$L_{10}$: basic life cycle [million cycle]. Here, the number 10 is a definition considered statistically.

## Developed a Life Cycle

Below is the equation that gives this formula of the developed rolling bear life cycle [17].

$$L_{nm} = a_1 . a_{iso} . L_{10} \qquad (10)$$

$L_{nm}$: Developed a life cycle.
$a_1$: Life modification factor for reliability
$a_{iso}$: Life modification quotient is as given in references [17] and [18].

The life cycle results calculated at MESYS software [19] (figure 19). According to the tests, the results are presented in Fig. 18 and 19.

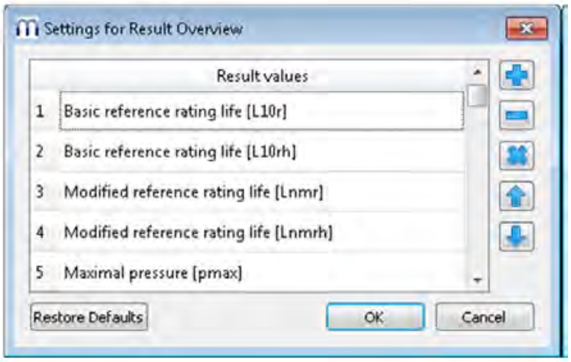

1 Basic reference rating life [L10r]
2 Basic reference rating life [L10rh]
3 Modified reference rating life [Lnmr]
4 Modified reference rating life [Lnmrh]
5 Maximal pressure [pmax]

**Figure 19.** The computing of the life cycle by MESYS software

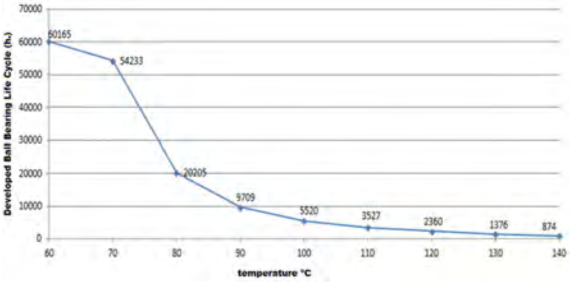

**Figure 20.** 6008 ball bearing developed life cycle versus temperature computed by MESYS software [19]

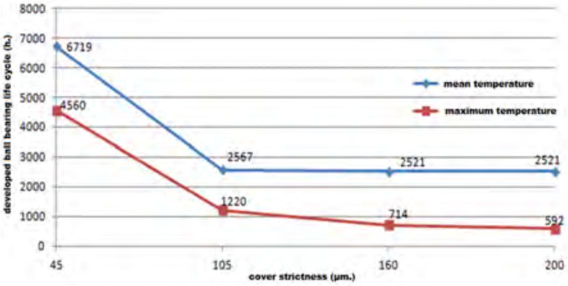

**Figure 21.** 6008 ball bearing developed life cycle versus seal strictness based on mean and max. temperatures computed by MESYS software [19].

The life cycle of ball bearings according to the temperature and seal strictness values are presented in Fig. 20 and 21. As strictness increases, the life cycle decreases. The most dramatic drop in the life cycle is between 45µm and 105µm. Between 105 µm and 200 µm, a slight decrease in the life cycle has been observed. This is because temperature degrees also slightly decrease between 105 µm and 200 µm as seen in Fig. 21.

**Table 9.** Developed life cycle versus seal strictness based on mean and max. temperatures

| Seal Strictness | Mean Temperature, Last 30.min. (°C) | 6008 ball bearing developed life cycle (h.) | Maximum Rolling Bearing Temperature (°C) | 6008 ball bearing developed life cycle (h.) |
|---|---|---|---|---|
| 200 µm | 118,9 | 2521 | 150 | 592 |
| 160 µm | 118,9 | 2521 | 145 | 714 |
| 105 µm | 118,6 | 2567 | 132,5 | 1220 |
| 45 µm | 97,8 | 6719 | 104 | 4560 |
| contactless | 65,7 | 60165 | 67 | 60165 |

The developed life cycles according to the seal strictness values are given in table 9. It is seen that as the seal strictness increase, temperature increase and the life cycle decreases. Strictness values bigger than 105 µm do not affect the life cycle significantly.

## FINITE ELEMENT ANALYSIS (FEA)

Two different basic material model is available for composing FEA model for elastomers. One of them is Rivlin Series (a polynomial function) that depends on strain invariants and the other one is Ogden Form (a strain energy function) that depends on stretch ratios. These models are embedded in ANSYS; some of them are Neo-Hookean, Arruda-Boyce, Gent, Blatz-Ko, Mooney Rivlin, Yeoh, Ogden hyperelastic models [20].

The most commonly used one is Mooney-Rivlin Strain Energy Function for the elastomers non-lineer stress analysis [13].

Contact stress has been analysed and evaluated by ANSYS Workbench. There are 3 criteria to make a FEA model of an elastomer material [21];

1. Model must be not linear,
2. Mechanical behaviour must be not linear,
3. Contact type that used in FEA software must be not linear.

According to these 3 criteria; non-linear model is chosen. Some presuppositions are;

1. Material is perfectly elastic,
2. Material is izotropic,
3. Material is uncompressible. According to these assumptions; hyperelastic model is choosen.

These criteria and pre-suppositions are also our boundry conditions.

**Table 10.** Mesh Form Analysis

| | Different Mesh Forms Models | | | | | |
|---|---|---|---|---|---|---|
| | 1 | 2 | 3 | 4 | 5 | 6 |
| Mesh Number | 202 | 525 | 2122 | 12562 | 49700 | 197955 |
| Mesh Quality (%) | 92,7 | 96,8 | 98,2 | 98,6 | 98,9 | 98,91 |
| Mesh Dimension (mm.) | default | 0,05 | 0,025 | 0,01 | 0,005 | 0,0025 |

Six different mesh models are composed as seen in table 10, results of each is given in table 11.

The solution time for 4th model is 739 s., for 5th model is 3990 s. and for 6th model is 33624 s. After making an evaulation according to the solution times and practical process, 5th model is chosen for ANSYS. 5th model has a low contact penetration as 0,4 µm and this is acceptable for the FEA. Mesh form is seen in figure 20 for 160 µm cover strictness sample.

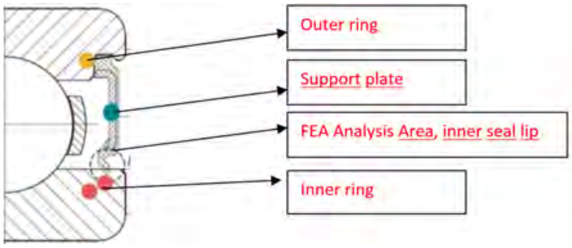

**Figure 22.** FEA Analysis Area

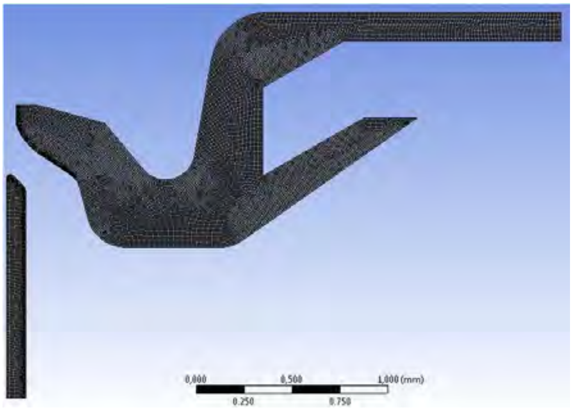

**Figure 23.** 160 µm cover strictness mesh structure

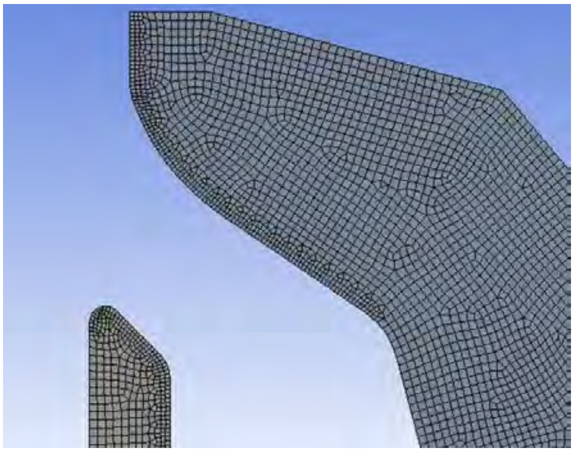

**Figure 24.** 160 µm cover strictness mesh structure-detailed

Boundry Conditions are detailed as follows: Inner ring is fixed in all directions, elastomer seal has a displacement degree of freedom in x:0 mm, y:-0,75 mm. Except FEA analysis area (between inner lip of elastomer seal and inner ring contact surface) Fig. 22, all the parts are fixed. Because, friction occurs in FEA analysis area. Our study/investigation is on seal strictness and friction force.

**Table 11.** Mesh Form Analysis Results

| Model No. | Max. Stress [MPa] | Max. Strain | Max. Contact Pressure [MPa] | Contact Reaction Force [N] | | | Contact Penetration [µm] |
|---|---|---|---|---|---|---|---|
| | | | | | Y | Total | |
| 1 | 1,1586 | 0,10858 | 0,3912 | 4,165 | 0,6974 | 4,2232 | 7,5306 |
| 2 | 1,2025 | 0,11159 | 0,4651 | 4,216 | 0,7102 | 4,275 | 4,0786 |
| 3 | 1,3076 | 0,11904 | 0,6116 | 4,232 | 0,7073 | 4,2952 | 2,055 |
| 4 | 1,471 | 0,13096 | 1,0506 | 4,318 | 0,6403 | 4,3647 | 0,8929 |
| 5 | 1,5273 | 0,13496 | 1,5408 | 4,303 | 0,65692 | 4,3532 | 0,4003 |
| 6 | 1,5568 | 0,13704 | 1,7655 | 4,308 | 0,65798 | 4,3575 | 0,2179 |

## Hyperelastic Models in ANSYS

Mooney –Rivlin Method, 9 parameter (Fig. 25) is chosen to solve curve fit method (Fig. 26.) in ANSYS.

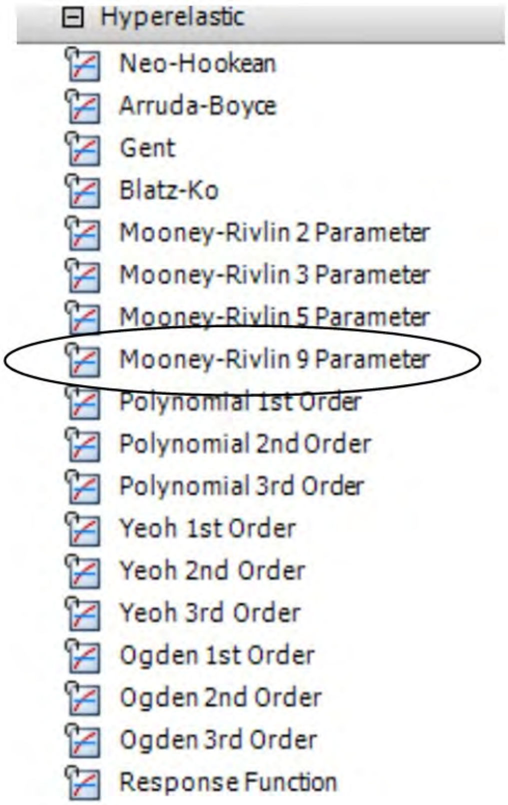

**Figure 25.** Hyperelastic Material Models in ANSYS Workbench

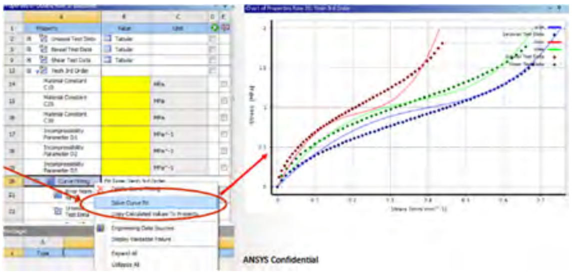

**Figure 26.** Solve Curve Fit Method by ANSYS Workbench [22]

## ANSYS Analysis Results

Contact force in 200 µm cover strictness is shown in Fig. 28. Most of the contact force is at x-axis. As the seal strictness value increases, the contact force increases as shown in table 12.

**Table 12.** Contact Reaction Force between Seal and Bearing Slice (FEA Results)

| *Cover Strictness [µm.]* | *Rate of Friction Test Mean Results [Nm.]* | *Rate of FEA Contact Force Results [Nm.]* |
|---|---|---|
| *105/45* | *0,0755/0,0487=1,55* | *3,10/1,53=2,02* |
| *160/105* | *0,1056/0,0755=1,40* | *4,36/3,10=1,41* |
| *200/160* | *0,1314/0,1056=1,24* | *5,18/4,36=1,18* |

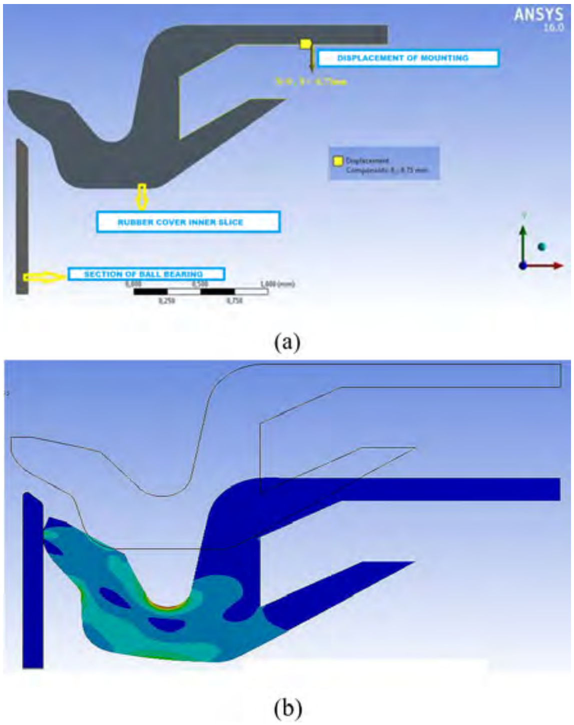

**Figure 27.** 160 µm cover strictness ; position a) before mounting and b) during the mounting (stress distribution)

**Figure 28.** Total contact reaction force in 200 µm cover strictness (45,105 and 160 µm cover strictness is not shown, since they are same as 200 µm)

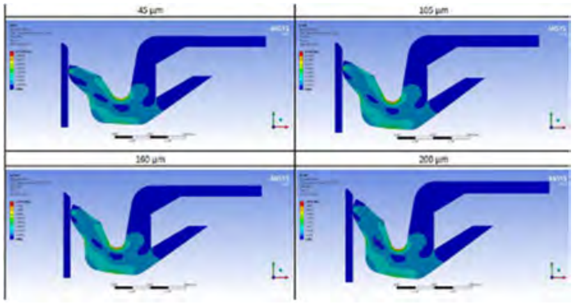

**Figure 29.** Contact Reaction Force for Different Seal Strictness Covers between Seal and Bearing Slice

**Table 13.** Comparison (By Ratio) of Friction Tests and FEA Results

| *Cover Strictness [µm.]* | *Max. Equivalent Stress [MPa]* | *Contact Reaction Force [MPa]* | | |
|---|---|---|---|---|
| | | *X* | *Y* | *Total* |
| *45* | *0,538* | *1,514* | *0,227* | *1,531* |
| *105* | *0,949* | *3,074* | *0,461* | *3,108* |
| *160* | *1,476* | *4,317* | *0,648* | *4,366* |
| *200* | *1,853* | *5,13* | *0,77* | *5,187* |

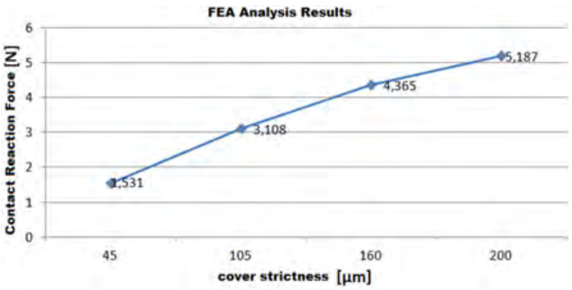

**Figure 30.** Contact Reaction Force between Seal and Bearing Slice (FEA Results)

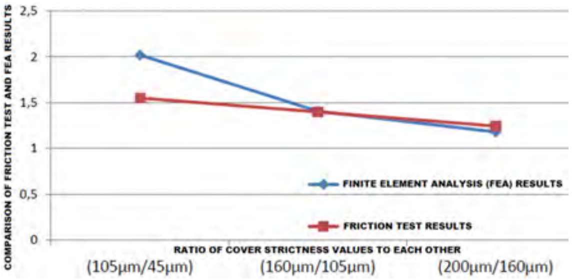

**Figure 31.** Friction Test and FEA Results (non-unit comparison)

As seen in Fig. 30, contact force increases with the high cover strictness values. The friction momnet test results and FEA-ANSYS analysis results are consistent with each other (table 13 and Fig. 31).

Friction test and FEA analysis results are consistent with each other as seen in Fig. 31.

## DISCUSSION

One of the most significant parameters that affect the ball bearing performance is seal strictness and its design. As the test results are observed and examined, the temperature reaches 150°C at the 200µm seal strictness. This is a high value and is needed to be reevaluated. Namely; material (NBR) starts to deteriorate and lose its performance specifications at 150°C. Sealing property is about to be lost in a short time. The most efficient temperature value should be in the 120-125°C range. So; a ball bearing seal strictness is a factor directly affect the life of a ball bearing.

Then it is essential to make optimization. We will choose either a lesser seal strictness value or a more durable material. More durable material means a more expensive material.

As the strictness increases, friction moment increases linearly at unloaded ball bearings. In our study, the effect of strictness affects directly the performance of ball bearing via friction moment and temperature degrees.

An optimum value for seal strictness according to the usage area is to be chosen.

The relationship between numerical results obtained from numeric simulation and friction moment test results have been analysed and evaulated. As a consequence, it has been observed and proved that the numeric results are consistent with the test results.

## CONCLUSION

Based on the obtained results, the following deductions may be drawn;

1. The seal strictness has a great effect on the life of a rolling bearing.
2. As the strictness increases, temperature increases and this leads to a decrease in the life cycle of the bearing.
3. It should be made an optimization to choose the seal according to the usage area. Because there is a contradiction, if we choose strictness greater, we can provide the seal better, but the life cycle decreases as the temperature increases. Vice versa is also true.
4. These results are also consistent with theory and MESYS software.
5. The friction test and FEA/ANSYS results are consistent with each other.
6. The optimum service temperature of rolling bearing according to tests is 110°C, because every temperature increase after 110°C decreases developed bearing life dramatically.

## ACKNOWLEDGEMENTS

We are very grateful to the Ortadoğu Rulman Sanayi A.Ş. for helping and guiding us at conducting tests and making time for experiments; esp. Mr. Tahir YILDIRIM Manufacture Director, Mr. Bilal DEMİR Automotive Application Chief, Mr. Tahir YILDIRIM and Mr. İbrahim TEMİZBAŞ senior engineers.

## CONFLICT OF INTEREST

Authors approve that to the best of their knowledge, there is not any conflict of interest or common interest with an institution/organization or a person that may affect the review process of the paper.

## AUTHOR CONTRIBUTION

Z. Ozdemir, K. Sarigoz and O.S. Turkbas contributed equally this study and experiments. All authors take the access and responsibility for the integrity of data.

## References

1. Shigley's Mechanical Engineering Design, Eighth Edition Budynas∻Nisbett. 2011.
2. ORS Rulman. Ortadoğu Rulman Sanayi ve Ticaret A.Ş.. URL:https:// ors.com.tr/tr/page/42/rulman-nedir last update, 2017-12-19.
3. Harris, T. A., Kotzalas M. N., Essential Concepts of Bearing Technology, CRC Press, Taylor Francis Group, 2007.
4. Sada, T. Loss reduction of rolling bearings for the automobile, Journal of Japanese Society of Tribologists. (2017).
5. Gorycki, L. Analysis of the Impact of the Cage Type on the Frictional Moment Rolling Bearings, David Publishing. Journal of Mechanics Engineering and Automation 5 (2015) 450-453.
6. B.Choe, J.Lee, D.Jeon and Y.Lee, Experimental study on dynamic behavior of ball bearing cage in cryogenic environments, Part I: Effects of cage guidance and pocket clearances. Mechanical Systems and Signal Processing Elsevier (2018).
7. Y.Cui, S.Deng, R.Niu, G.Chen, Vibration effect analysis of ball dynamic unbalance on the cage of high-speed cylindrical ball bearing. Journal of Sound and Vibration Elsevier (2018).
8. Z.Yang, T.Yu, Y.Zhang and Z.Sun, Influence of Cage Clearance on the Heating Characteristics of High-Speed Ball Bearings. Tribology International (2016).
9. Takimoto, M., Ishikawa, T., and Harada, K., Technical development of automotive wheel bearing seals (Muddy-water resistant seal, low-temperature environment seal and super low-torque seal). JTEK Engineering Journal (2011) 64-68.
10. White J. R., De, S. K., Rubber Technologist's Handbook, The United Kingdom. Rapra Technology Limited, 50, 77-78, 2001.
11. SKF Group, Rolling Bearings Catalogue, 2013.
12. Brown R., Physical Testing of Rubber. Springer, 2006.
13. Gent, A. N. Engineering With Rubber How to Design Rubber Components (Third Edition), Munich: Hanser Publishers, 2012.
14. Simpson, R. B. "Rubber Basics", United Kingdom: Rapra Technology Limited, 2002.
15. ASTM G182 - 13, Standard Test Method for Determination of the Breakaway Friction Characteristics of Rolling Element Bearings, 2018.
16. DIN 51819-1 2016 Edition, Testing of Lubricants - Mechanical-Dynamic Testing İn The Roller Bearing Test Apparatus FE8 - Part 1: General Working Principles, 2016.
17. ISO-16281:2008. Rolling bearings-Methods for calculating the modified reference rating life for universally loaded bearing, 2008.
18. ISO-281:2007. Rolling Bearings - Dynamic Load Ratings and Rating Life, International Standard Organization, 11-12, 18, 25-32, 44, 2010.
19. ISO 16281:2008-Rolling bearings: Methods for calculating the modified reference rating life for universally loaded bearing, 2008.
20. MESYS Software MSC Software. Nonlinear finite element analysis of elastomers. MSC Software, 2010.
21. Ghaemi, H., Behdinan, K., Spence, A. On the development of compressible pseudo-strain energy density for elastomers application to finite element. Journal of Materials Processing Technology, 318. (2006).
22. Carlescu, V., Prisacaru, G., Olaru, N. D. (2014). FEM simulation on uniaxial tension of hyperelastic elastomers. Applied Mechanics and Materials 659 (2014), 57-62.
23. Miller, K. (2014). Experiments and fitting of advanced polymer models in ANSYS. Axel Products Regional Conference, 28, 2014.

Hittite Journal of Science and Engineering, 2021, 8 (3) 233–240
ISSN NUMBER: 2148–4171
DOI: 10.17350/HJSE19030000233

# Investigation of Shale Gas Reserves in the World and A Case Study for Electricity Production from Shale Gas in Turkey

**Erman Kadir Oztekin** **Alperen Tozlu**
Bayburt University, Department of Mechanical Engineering, Bayburt, Turkey

***Article History:***
*Received: 2021/04/25*
*Accepted: 2021/08/18*
*Online: 2021/09/29*

***Correspondence to****: Erman Kadir Oztekin,*
*Bayburt University, Mechanical*
*Engineering, 69000, Bayburt, TURKEY*
*E-Mail: ermanoztekin@bayburt.edu.tr*
*Phone: +90 458 211 1153/1643*
*Fax: +90 458 211 1178*

## ABSTRACT

Shale gas reserves, which is globally accepted as unconventional gas resource, scattered around the world and can be used in order to meet the growing energy needs due to limited amounts of conventional resources. Since notable effort has to be put in order to investigate and drill shale gas resources the early decision has to be made carefully, especially considering the economic benefits. Several factors must be considered including the known technically recoverable shale gas amount at the selected region, current technology to drill the shale source and the amount of investment before the extraction of shale gas. In this study, global underground shale gas amount and recent discoveries as well as the potential shale gas areas in Turkey are presented. Benefits of using shale gas for electricity generation and common methods being used during shale gas extraction are studied along with gas and liquid flow mechanisms. At the end, general overview of separation and utilization of shale gas components is schematically presented. In the case study, the potential of electricity generation in the SE Anatolia region in Turkey is estimated with only using methane obtained from the shale gas purification process at the power generation step. According to the estimations, 3337.8 MW installed power may be generated for 50-55 years, at the appropriate gas engine by using 8.5 billion cubic meter shale gas annually.

**Keywords:**
Shale gas; Natural gas; Electricity generation; Global reserves; Gas engine

## INTRODUCTION

### Shale Gas and Effective Factors in the Formation

Today many studies have been carried out to benefit from alternative energy reserves to meet the increasing energy needs and the depletion of conventional energy reserves in our world. Shale gas reserves have a large share among these unconventional energy reserves and have started to find an increasing place in the literature [1-3]. Generally, ‘unconventional gas’ can be grouped in six classes namely; coalbed methane, tight gas, geopressured gas, gas hydrates, shale gas, and ultra-deep gas placed in different layers of the Earth’s crust [4-6]. The termination of unconventional gas is highly depending on the technology for production however the classification can be schematically seen from Fig. 1.

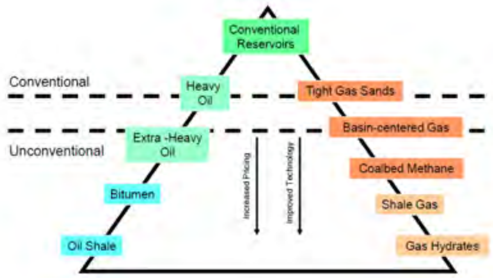

**Figure 1.** Classification of unconventional resources [7].

Shale gas is known as a compressed gas with rich hydrocarbon content that accumulates within shale formations of sedimentary rocks where these formations poses natural barrier to the migration of oil and gas. These gases are formed by the transformation of the contents of the residues remaining in the pores of the bedrock and later turned into gas form while the migration of natural gas and oil from the bedrock to different layers of Earth crust. Similarly, shale gas can be associated with natural gas trapped inside mudrocks that can be named as mudstone or shale and shale gas

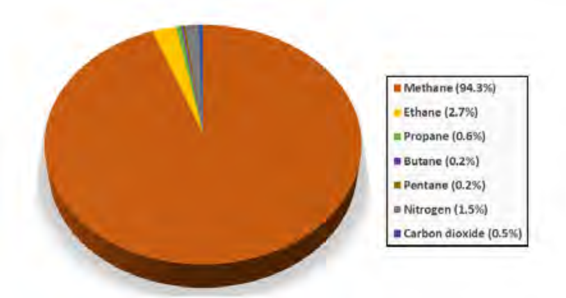

**Figure 2.** Volumetric averages of shale gas composition extracted in the US [12].

can be found in free, adsorbed and dissolved from in shale structure [8]. One of the most important factors affecting the accumulation shale gas in the solid structure are the porosity of the shale rock structure, the chemical content of the matrix and especially the amount of organic matter in this content [9, 10]. The chemical content contains both organic, namely kerogen, and inorganic components such as clay minerals. Therefore, estimation of total permeability of the shale is essential for gas extraction [2]. The porosity of the shale matrix is estimated within the range from 5 to 10 percent [8]. After all required criteria are met mentioned earlier, rich shale target can be observed at shallow depths with a sufficient thermal maturity [5]. Gas flow is obtained through fractures so macroscopic properties of the gas flow such as permeability, adsorption and diffusivity are important.

Shale gas contains methane ($CH_4$) the most in its content where methane can be found as free gas under high pressure inside the fractures or pores and found in adsorbed phase in the bulk media of micropores in accordance with strong binding energy [11]. Averaged volumetric ratios of shale gas contents obtained in the U.S. can be seen on Fig. 2. Methane and nitrogen are the major components in the typical shale gas along with propane, ethane, oxygen, and carbon monoxide [12]. Shale gas does not contain harmful hydrogen sulfide. It should be noted that shale gas content varies from basin to basin.

## Methods to Obtain Shale Gas and History of Development

Appropriate methods have been implemented for obtaining shale gas. Among these methods, the horizontal drilling and hydraulic fracturing methods which are currently being used today and made it possible to extract shale gas efficiently [13, 14]. Namely, these two methods have made it possible to obtain shale gas from places that previously would have been inaccessible [15]. In the hydraulic fracture method, the liquid, which is sent with high pressure and in a controlled manner, creates fractures and cracks in the structure of the rock and allows the gas inside to be collected. Depending on the scale of the drilling area, millions of gallons of water along with proppants such as; acid, mineral oil, iso propanol, ethylene glycol and sodium carbonate are sent with high pressure to the area where the trapped gas exist. The piping in this system is arranged to make the flow of fracture liquid and collected gas bidirectional and controlled. If necessary, cement and casing combination is mounted in the well. In this way, the groundwater in the region is protected. Similarly, horizontal drilling method is a technological method which allows long lines can be drawn in kilometers. During completion of shale gas wells both cement and casing can be used to protect underground water sources. The completely active first producing and commercial gas well in the U.S. was dated back to 1821 [15]. After a while, the UK drilled its first shale gas well in 1875 [5]. In 1976, the American Department of Energy initiated incentive projects for shale gas extraction, and as a result of successful projects, many companies have accelerated their shale gas extraction efforts since 2005 [16]. It can be argued that the technology used in the production of shale gas is a continuation of the technology implemented for natural gas production. It has been calculated that the shale gas production process can be completed in the most economical way when combining horizontal drilling and hydraulic fracturing methods [14]. By this way the permeability of the shale matrix can be increased. In addition, as previously stated, the management of the water used for shale gas production and the extra water coming from the well is important in terms of human health, environment and economy. The fluid moves along the cracks formed in the rough structure by obeying Darcy's law. Therefore, before the shale gas extracting event, the correct estimation of shale permeability is crucial [17]. Typical fracture patterns are considered during estimations such as; dead end, effective flow path and merged fractures. For example, in particular case dead end fractures may not be effective in fracture network in the rough structure. These types of studies somehow are not perfectly matched with real time data; thus, it was argued that the structure and effectiveness of kerogen, a macromolecule directly related with hydrocarbons in shales, in flow mechanisms should be understood for better model estimations [18].

## Shale Gas Transport Mechanisms

Existence of highly porous media with pores formed in various scales and simultaneous multiple physicochemical processes lead to complex and transient flow characteristics during shale gas extraction [8, 19]. Flow transport occurs in multiple mechanisms. Desorption of shale gas from walls of pores formed in different scales, diffusion of dissolved gas in kerogen medium and gas transport

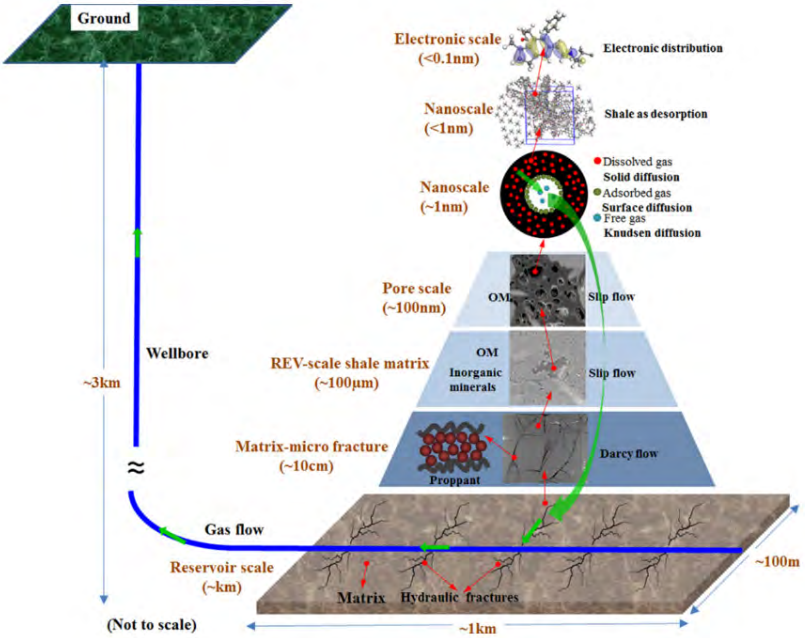

**Figure 3.** Detailed flow, diffusion, desorption and distribution processes during shale gas extraction [8].

from the boundaries of pores are governed with multiple physics laws such as Darcy flow, transition flow, Knudsen diffusion [8]. In addition, changing physical properties of pore medium during hydraulic fracturing, and nano scale effects in small pores lead to significantly confusing flow network during operation. The flow process can be summarized in Fig. 3. Understanding flow mechanism is essential in order to increase shale gas recovery during hydraulic fracturing [20-22]. For example injection of $CO_2$ into fracture fluid may result in an increase methane recovery based on simulations [20, 23, 24].

## ENERGY BENEFITS AND ENVIRONMENTAL ASPECTS OF SHALE GAS PRODUCTION

The correct application of the techniques used in shale gas production, planning and qualified work are of great importance in terms of both energy gain and environmental factors [5]. Although the increasing shale gas production can close the energy gap of the countries, the United States has planned to increase the shale gas production to 50 percent of the total national gas production by 2030. Global shale gas production by the addition of other countries including Canada, Russia, India, Australia, countries of Europe and China will be expected to reach 32 percent of global natural gas production by 2035.

Per thousand cubic feet of shale gas costs from $2 to $3 which is almost the half price of same amount of natural gas obtained from conventional gas wells [25]. The cheaper price of shale gas can eventually lead to cheaper electricity which can manifest itself in the annual economic growth. Increasing the shale gas production, which has a vast distribution on the basis of countries, can reduce the foreign dependence of countries on natural gas, i.e. the ever-increasing need of the European Union, and prevent foreign interventions in their economies [25, 26].

Opening and actively benefiting from gas wells eventually will lead to new job opportunities. For instance, in 2011, annual operation of Barnett Shale in Texas resulted in approximately 8% increase in the economy of the state, and supported 10% of regional employment [27].

In terms of environmental concerns shale gas has lower toxic gas emissions than fossil fuels [28, 29]. It can definitely be used for industrial purposes in terms of global warming concerns [30]. Commercial use of shale gas can offer cleaner atmosphere in countries where the industial use is highly dependent on oil and coal consumption [5].

As mentioned above before extraction of gas from a specific well, hydraulic fracturing operation require significant amount of water to be sent to target area with high pressure [31, 32]. For instance, annual water usage in Texas for three wells namely; Barnett Shale, Texas-Haynesville Shale, and Eagle Ford Shale was estimated to be equal of approximately 9 percent water consumption of 1.3 million people. And the injection of fluids does not include only water but also relatively significant amount of acids, surfactants, inhibitors, and friction reducers [33, 34]. So, the safety of the underground water sources should be considered and necessary precauti-

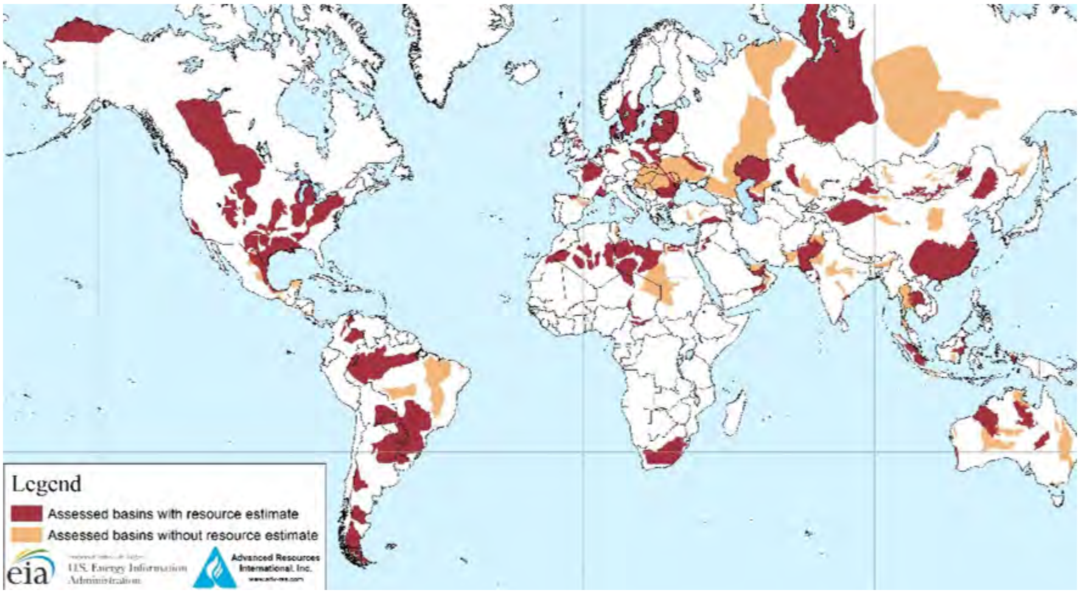

**Figure 4.** Map of basins with assessed shale oil and shale gas formations, as of May 2013 [42].

ons must be taken before and after drilling since these additives are posing danger to environment and they are known to be carcinogenic [35, 36]. Thus several filtering methods have been employed to clean recovered water from wells [14, 37, 38]. Additionally, studies continue to investigate that the tremors that occur as a result of shale gas extraction trigger earthquakes [39-41].

## GLOBAL SHALE GAS PRODUCTION

Shale gas resources spread in 42 countries worldwide, including U.S. that constitute 32 percent of the world's technically recoverable resources [42]. The Fig. 4 illustrates the major shale gas basins distributed around the world. It can be concluded that the presence of the source is vast and can be economically benefited by production in huge amounts.

Moreover, since most of the countries have the potential for gas production, many countries can meet the energy needs. For example, U.S. Energy Information Administration released a report that U.S. had significant amount of proved reserves containing approximately 342.1 trillion cubic feet shale gas in 2018 and later this value has increased to 353.1 trillion cubic feet in 2019 [43]. Moreover, every year the amount of proved natural gas reserves tend to increase along with the shale gas share in the total with new discoveries. The annual shale gas production in the U.S. was 0.3 tcf in 2000 and it was taken off to 4.8 tcf in 2010 and eventually reached up to 9.6 tcf in 2012 [44]. The annual production of The Barnett Shale in Texas alone was approximately 0.5 tcf of natural gas in 2005 [42]. Fig. 5 shows the growth of U.S. total natural gas proved reserves (shale and other sources) from 2012 to 2019.

According to the world data, Russia has the most technically recoverable shale oil resources in the world [42]. United States, China, Argentina and Libya are also listed in the first five countries which have the most technically recoverable shale oil resources in the world. Although studies on shale gas basins generally deal with calculations for certain countries, there are still not enough studies for regions with rich underground resources such as the Caspian region and Middle East [5]. Today, at least 60 years of energy need of the world can be met with the technically recoverable shale oil and gas reserves known in our world [14]. There is no Globally accepted shale gas investigation method but U.S. Energy Information Administration set specific standards, that is, shale formations can be assessed based on a combination of factors such as availability of data, natural gas import dependence of a nation, observed large shale formations, and efforts by companies and governments directed

**Figure 5.** Proved natural gas reserves of the U.S. (shale and other sources), from 2012 to 2019 [43].

at shale resource development [42]. Moreover, obtained data from Argentina promise a future in shale gas production [45]. The natural gas production potential of Argentina has been steadily increasing for the last three years due to high capacity at the Neuquén Basin's Vaca Muerta shale and tight gas play. At Neuquén Basin, with 583 tcf technically recoverable shale gas reserve, 29 thousand cubic meters of shale gas produced in one day.

## SHALE GAS PRODUCTION POTENTIAL OF TURKEY

According to U.S. Energy Information Administration report Turkey has 24 tcf EIA/ARI unproved wet shale gas and 4700 million barrels EIA/ARI unproved shale oil technically recoverable resources in 2013 [42]. Map of major shale basins in Turkey can be seen on Fig. 6. Turkey has two major approved basins, SE Anatolian (Dadas shale) and Thrace (Hamitabat shale) with 17 and 6 tcf technically recoverable shale gas and 4.6 and 0.1 Billion bbl technically recoverable shale oil, respectively. Turkish national petroleum company (TPAO) and several international companies have still ongoing research and drilling operation on these two major basins.

Salt Lake basin and Sivas basin are predicted to have also shale production potential when examining the geological details but still more data is required for certain predictions. The Southeast Anatolia Basin, covering 32,100 square meters area, is located at south-east side of Turkey and is adjacent to Iraq and Syria. First well was opened by Anatolia Energy in 2012 [46]. The Thrace Basin, covering 6,500 square meters area, is located at north-west side of Turkey and bordered with several massif areas including Istranca Massif, the Rhodope Massif and the Sakarya Massif. The basin is Turkey's primary natural gas producing area with approximately 350 wells.

Shell and TPAO partnership started in shale gas exploration works in Diyarbakır, Silvan, initially Joint Venture Agreements contract was signed in 2011 [45]. In 2015, calculated total technically recoverable shale gas resources was estimated, approximately 15 tcf, lower than current data and it was estimated that the reserve, estimated in 2015, corresponds to Turkey's energy needs for 30 years [47]. Later, Shell company left the project in 2016 [45]. As a result, it was determined that Turkey has processible shale gas formations with suitable mudstone depth and rocks with sufficient mineral compositions for the formation of shale gas and available for hydraulic fracturing usage.

**Figure 6.** Major Shale Basins of Turkey [42].

## CASE STUDY: ELECTRICITY GENERATION IN SE ANATOLIAN BASIN

Since shale gas is an important alternative fuel source, the results of its possible use for electricity generation in our country should be evaluated carefully. In this context, the stages from shale gas extraction to electricity generation are schematically presented in Fig. 7 to create a general impression for the reader. As seen in the Fig. 7, by-products produced from shale gas at different stages can be used for several reasons. At the end of the designed process, electricity generation can be accomplished at the power plant with selection of appropriate engines.

Herein, as a case study, the electricity generation potential of SE Anatolia region with 481.3 billion cubic meter technically recoverable shale gas is evaluated by utilization of methane output [42]. Several methods have already been developed to produce electricity from unconventional

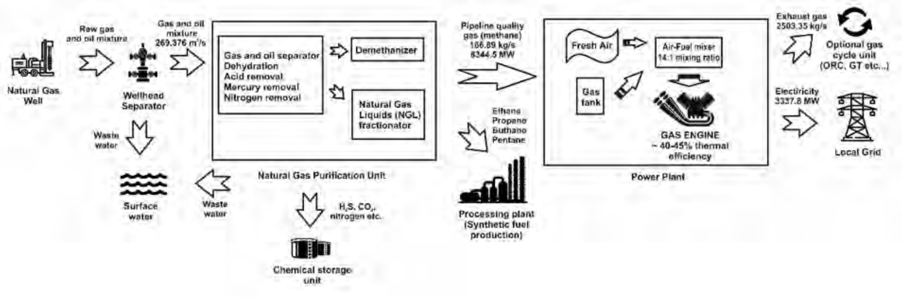

**Figure 7.** General scheme of shale gas separation and utilization.

energy sources [48-51]. Diesel engines and gas engines are widely used in energy industry [52-56]. Since Turkey is still in a need for investment in shale gas exploration and drilling, the annual shale gas production in SE Anatolia region is considered to be approximately 8.5 billion cubic meter which is similar to US production in 2000 when US is not yet very experienced in shale gas production [44]. This corresponds to approximately 50 to 55 years of shale gas production for this case study. This estimated time frame is in line with the previous estimates for Turkey's energy demand from shale gas [45, 47].

As seen from Fig. 7, the water used for hydraulic fracturing is initially separated from wellhead and the remaining gas-oil mixture is sent to purification stage in order to be delivered to mainline transmission systems and to meet necessary quality standards. Some of by-products produced from purification stage such as acids, nitrogen can be either stored or utilized for specific reasons since they are still valuable in chemical industry. Accordingly, natural gas liquids (NGL) can be further processed to obtain synthetic fuels. NGL products are valuable in fuel industry [57, 58]. Moreover they can be used as alternative fuel especially methanol [59]. Pipeline gas (methane) is obtained in the last step of purification stage. Composition of shale gas can slightly change from basin to basin but methane is still the dominant component of the shale gas. For this study 94% of the shale gas composition is considered to be pure methane which is similar with the average shale gas composition in US basins [12]. This amount is approximately corresponding to methane mass flow ratio of 166.89 kg per second. In power plant several common types of gas engines can be employed to produce electricity power. The thermal efficiency of gas engines operating using natural gas is generally between 40 and 45% [60-64]. Here 40% thermal efficiency is considered to produce electric power. And also, methane gas is mixed with 14 times more air. 3337.8 MW installed power is calculated. Relatively huge amount of exhaust gas is obtained during electricity generation. The temperature of the exhaust gas can vary with respect to engine type but it can be argued that the temperature of the exhaust gas will be around 400°C ~ 500°C [65-67]. Thus, the exhaust gas which contains considerable amount of thermal energy can be further utilized in several gas cycles such as Organic Rankine Cycle (ORC), Gas Turbine Cycle (GT) for further electric power production [68-72].

## CONCLUSION

In this study, the amount of available shale gas and developments across the world and in Turkey has been examined. Additionally, the flow mechanisms of the shale gas wells are presented. The results and the comments that can be made can be listed as follows:

- Shale gas exploration and drilling activities continue around the world and are supported by new investments.

- In addition to countries with large shale gas reserves such as America and China, countries such as Argentina come to the fore with their reserves in the light of new studies.

- Turkey needs new investments to cover the high costs of shale gas drilling and production. Thus, developing technology in shale gas exploration and drilling will be an important factor in reducing costs and in determining Turkey's shale gas extraction targets.

- The estimated amount of shale gas reserves in Turkey is 679 billion cubic meter which is very small compared to the dominant countries in the world in terms of shale gas reserves. For instance, Argentina's Neuquén Basin alone has 24 times more shale gas reserves.

- In this case study it has been put forward that 3337.8 MW installed power may be generated by using 8.5 billion cubic meter shale gas annually for 50-55 years only in SE Anatolia region. According to the data presented in the first half of 2021, the installed capacity of power plants in Turkey is 92,798 MW [73]. The calculated electric power from shale gas corresponds to 3.6% of Turkey's current capacity.

- The positive returns of by-products obtained from shale gas can be quantified in future studies. In addition, it can be investigated whether the extra power that can be obtained by the use of exhaust gases will also be beneficial to the total power.

- Depending on newly discovered shale gas resources and their capacities in Turkey, total possible electric power generation can be re-calculated in future studies.

## ACKNOWLEDGEMENT

Authors gratefully acknowledge Bayburt University for providing their software facilities and constant interests in this study.

## CONFLICT OF INTEREST

Authors approve that to the best of their knowledge, there is not any conflict of interest or common interest with an institution/organization or a person that may affect the review process of the paper.

## AUTHOR CONTRIBUTION

All section including conceptualisation, methodology, software, analysis, writing, review and editing were equally organised and performed by Erman Kadir Oztekin and Alperen Tozlu.

## References

1. Mastalerz, M., A. Drobniak, and A.B. Stankiewicz, Origin, properties, and implications of solid bitumen in source-rock reservoirs: A review. International Journal of Coal Geology. 195, 14-36, 2018.
2. Cui, J. and K. Wu, Equivalent permeability of shale rocks: Simple and accurate empirical coupling of organic and inorganic matter. Chemical Engineering Science. 216, 115491, 2020.
3. Estrada, J.M. and R. Bhamidimarri, A review of the issues and treatment options for wastewater from shale gas extraction by hydraulic fracturing. Fuel. 182, 292-303, 2016.
4. Hackley, P.C. and B.J. Cardott, Application of organic petrography in North American shale petroleum systems: A review. International Journal of Coal Geology. 163, 8-51, 2016.
5. Sovacool, B.K., Cornucopia or curse? Reviewing the costs and benefits of shale gas hydraulic fracturing (fracking). Renewable and Sustainable Energy Reviews. 37, 249-264, 2014.
6. Davies, R.J., et al., Oil and gas wells and their integrity: Implications for shale and unconventional resource exploitation. Marine and Petroleum Geology. 56, 239-254, 2014.
7. Chan, P., J.R. Etherington, and R. Aguilera, A Process to Evaluate Unconventional Resources. Paper presented at the SPE Annual Technical Conference and Exhibition, Florence, Italy, September 2010.
8. Wang, H., et al., Modeling of multi-scale transport phenomena in shale gas production — A critical review. Applied Energy. 262, 114575, 2020.
9. Gale, J.F.W., et al., Natural fractures in shale: A review and new observations. Aapg Bulletin. 98(11), 2165-2216, 2014.
10. Ross, D.J.K. and R. Marc Bustin, The importance of shale composition and pore structure upon gas storage potential of shale gas reservoirs. Marine and Petroleum Geology. 26(6), 916-927, 2009.
11. Dang, W., et al., Investigation of gas content of organic-rich shale: A case study from Lower Permian shale in southern North China Basin, central China. Geoscience Frontiers. 9(2), 559-575, 2018.
12. Korpyś, M., J. Wójcik, and P. Synowiec, Methods for sweetening natural and shale gas. Chemik Science-Technique-Market. 68, 213-215, 2014.
13. Stephanie, M.R., et al., Hybrid membrane bio-systems for sustainable treatment of oil and gas produced water and fracturing flowback water. Separation and Purification Technology. 171, 297-311, 2016.
14. Chang, H.Q., et al., Potential and implemented membrane-based technologies for the treatment and reuse of flowback and produced water from shale gas and oil plays: A review. Desalination. 455, 34-57, 2019.
15. Ground Water Protection Council, Modern Shale Gas Development In The United States: A Primer, U.S. Department of Energy, Office of Fossil Energy, National Energy Technology Laboratory (NETL), Oklahoma City, OK, 2009.
16. Gregory, K.B., R.D. Vidic, and D.A. Dzombak, Water Management Challenges Associated with the Production of Shale Gas by Hydraulic Fracturing. Elements. 7(3), 181-186, 2011.
17. Chen, D., Z. Pan, and Z. Ye, Dependence of gas shale fracture permeability on effective stress and reservoir pressure: Model match and insights. Fuel. 139, 383-392, 2015.
18. Agrawal, V. and S. Sharma, Are we modeling the properties of unconventional shales correctly? Fuel. 267, 117316, 2020.
19. Javadpour, F., D. Fisher, and M. Unsworth, Nanoscale Gas Flow in Shale Gas Sediments. Journal of Canadian Petroleum Technology. 46(10), 2007.
20. Iddphonce, R., J.J. Wang, and L. Zhao, Review of CO2 injection techniques for enhanced shale gas recovery: Prospect and challenges. Journal of Natural Gas Science and Engineering. 77, 12, 2020.
21. Liu, J., et al., Numerical evaluation on multiphase flow and heat transfer during thermal stimulation enhanced shale gas recovery. Applied Thermal Engineering. 178, 16, 2020.
22. Huang, L., et al., Effect of organic type and moisture on CO2/CH4 competitive adsorption in kerogen with implications for CO2 sequestration and enhanced CH4 recovery. Applied Energy. 210, 28-43, 2018.
23. Rani, S., E. Padmanabhan, and B.K. Prusty, Review of gas adsorption in shales for enhanced methane recovery and CO2 storage. Journal of Petroleum Science and Engineering. 175, 634-643, 2019.
24. Hu, X., et al., Thermodynamic effects of cycling carbon dioxide injectivity in shale reservoirs. Journal of Petroleum Science and Engineering. 195, 7, 2020.
25. Deutch, J., The Good News About Gas: The Natural Gas Revolution and Its Consequences. Foreign Affairs. 90(1), 82-93, 2011.
26. Tuğan, M.F., Assessing Uncertainties And Managing Risks In Shale Gas Projects, PhD thesis in Petroleum and Natural Gas Engineering Department. Middle East Technical University, Ankara, 2017.
27. House, E.J., Fractured Fairytales: The Failed Social License for Unconventional Oil and Gas Development. Wyoming Law Review. 13, 2013.
28. Wei, L.J. and P. Geng, A review on natural gas/diesel dual fuel combustion, emissions and performance. Fuel Processing Technology. 142, 264-278, 2016.
29. Burnham, A., et al., Life-cycle greenhouse gas emissions of shale gas, natural gas, coal, and petroleum. Environ Sci Technol. 46(2), 619-27, 2012.
30. Adgate, J.L., B.D. Goldstein, and L.M. McKenzie, Potential Public Health Hazards, Exposures and Health Effects from Unconventional Natural Gas Development. Environmental Science & Technology. 48(15), 8307-8320, 2014.
31. Vengosh, A., et al., A Critical Review of the Risks to Water Resources from Unconventional Shale Gas Development and Hydraulic Fracturing in the United States. Environmental Science & Technology. 48(15), 8334-8348, 2014.
32. Nicot, J.P. and B.R. Scanlon, Water use for Shale-gas production in Texas, U.S. Environ Sci Technol. 46(6), 3580-6, 2012.
33. Stringfellow, W.T., et al., Physical, chemical, and biological characteristics of compounds used in hydraulic fracturing. Journal of Hazardous Materials. 275, 37-54, 2014.
34. Howarth, R.W., A. Ingraffea, and T. Engelder, Natural gas: Should fracking stop? Nature. 477(7364), 271-5, 2011.
35. Kahrilas, G.A., et al., Biocides in Hydraulic Fracturing Fluids: A Critical Review of Their Usage, Mobility, Degradation, and Toxicity. Environmental Science & Technology. 49(1), 16-32, 2015.
36. Warner, N.R., et al., Impacts of Shale Gas Wastewater Disposal on Water Quality in Western Pennsylvania. Environmental Science & Technology. 47(20), 11849-11857, 2013.
37. Al-Ghouti, M.A., et al., Produced water characteristics, treatment and reuse: A review. Journal of Water Process Engineering. 28, 222-

239, 2019.

38. Shaffer, D.L., et al., Desalination and Reuse of High-Salinity Shale Gas Produced Water: Drivers, Technologies, and Future Directions. Environmental Science & Technology. 47(17), 9569-9583, 2013.
39. Li, L., et al., A review of the current status of induced seismicity monitoring for hydraulic fracturing in unconventional tight oil and gas reservoirs. Fuel. 242, 195-210, 2019.
40. Costa, D., et al., Extensive review of shale gas environmental impacts from scientific literature (2010–2015). Environmental Science and Pollution Research. 24(17), 14579-14594, 2017.
41. Ellsworth, W.L., Injection-Induced Earthquakes. Science. 341(6142), 2013.
42. U.S. Energy Information Administration, Technically Recoverable Shale Oil and Shale Gas Resources: An Assessment of 137 Shale Formations in 41 Countries Outside the United States. U.S. Department of Energy, Washington, DC, 2013.
43. U.S. Energy Information Administration, Proved Reserves of Crude Oil and Natural Gas in the United States, Year-End 2019. U.S. Department of Energy, Washington, DC, 2021.
44. Hao, F., H. Zou, and Y. Lu, Mechanisms of shale gas storage: Implications for shale gas exploration in China. AAPG Bulletin. 97, 1325-1346, 2013.
45. Derman, A., Unconventional Resources in Turkey: Myth or Reality? Energy Policy Turkey. (3), 75 - 87, 2017.
46. Anatolia Energy, Unlocking Turkey's Shale Resources. March, 2013.
47. Karsli, S.l., Shale Gas in Turkey According to the Latest Developments. Journal of the Institute of Science and Technology. 5(3), 2015.
48. Raj, N.T., S. Iniyan, and G. Ranko, A review of renewable energy based cogeneration technologies. Renewable and Sustainable Energy Reviews. 15(8), 3640-3648, 2011.
49. Ayşegül, A., S. Demir, and M. Kanoğlu, Biyogaz Beslemeli Gaz Motorlu Bir Kojenerasyon Sisteminin Termoekonomik Analizi. Isı Bilimi ve Tekniği Dergisi. 33(2), 9-21, 2013.
50. Michele, B., B. Lisa, and Andrea, Combining waste-to-energy steam cycle with gas turbine units. Applied Energy. 130, 764-773, 2014.
51. Mehmet, K.l., Süleyman, and A.l. Ayşegül, Performance characteristics of a Diesel engine power plant. Energy Conversion and Management. 46(11), 1692-1702, 2005.
52. Duc Luong, C., H. Guang, and L. Anh Tuan, Applying chemical heat storage to saving exhaust gas energy in diesel engines: Principle, design and experiment. Journal of Energy Storage. 28, 101311, 2020.
53. Ting, H. and L. Wensheng, Energy saving research of natural gas liquefaction plant based on waste heat utilization of gas turbine exhaust. Energy Conversion and Management. 225, 113468, 2020.
54. Dmitry, P., Energy optimization analysis of a thermochemical exhaust gas recuperation system of a gas turbine unit. Energy Conversion and Management. 171, 917-924, 2018.
55. Junjiang, B. and Z. Li, A review of working fluid and expander selections for organic Rankine cycle. Renewable and Sustainable Energy Reviews. 24, 325-342, 2013.
56. Olumide, O., W. Meihong, and K. Greg, Closed-cycle gas turbine for power generation: A state-of-the-art review. Fuel. 180, 694-717, 2016.
57. Wood, D.A., C. Nwaoha, and B.F. Towler, Gas-to-liquids (GTL): A review of an industry offering several routes for monetizing natural gas. Journal of Natural Gas Science and Engineering. 9, 196-208, 2012.
58. Yeşilyurt, M.K., An Experimental Study On The Performance And Exhaust Emission Characteristics Of A CI Engine Powered By Alcohol/Biodiesel/Diesel Fuel Blends Containing Different Types Of Alcohol (Isopropanol-C3, 1-Butanol-C4, And Isopentanol-C5). Hittite Journal of Science and Engineering. 7(2), 135-148, 2020.
59. Zhen, X.D. and Y. Wang, An overview of methanol as an internal combustion engine fuel. Renewable & Sustainable Energy Reviews. 52, 477-493, 2015.
60. Thomson, H., J.J. Corbett, and J.J. Winebrake, Natural gas as a marine fuel. Energy Policy. 87, 153-167, 2015.
61. Emrah, Ö. and T. Alperen, Optimization of an adapted Kalina cycle to an actual municipal solid waste power plant by using NSGA-II method. Renewable Energy. 149, 1146-1156, 2020.
62. Özahi, E., A. Tozlu, and A. Abusoglu, Organik Rankine çevrimi entegre edilmiş S-CO2 kullanılan bir gaz türbin çevriminin termodinamik ve termoekonomik analizi. Gazi Üniversitesi Mühendislik-Mimarlık Fakültesi Dergisi, 33(3), 2018.
63. Alperen, T., A. Ayşegül, and Ö. Emrah, Thermoeconomic analysis and optimization of a Re-compression supercritical CO2 cycle using waste heat of Gaziantep Municipal Solid Waste Power Plant. Energy. 143, 168-180, 2018.
64. Emrah, Ö., T. Alperen, and A. Ayşegül, Thermoeconomic multi-objective optimization of an organic Rankine cycle (ORC) adapted to an existing solid waste power plant. Energy Conversion and Management. 168, 308-319, 2018.
65. Emrah, O., A. Aysegul, and T. Alperen, A comparative thermoeconomic analysis and optimization of two different combined cycles by utilizing waste heat source of an MSWPP. Energy Conversion and Management. 228, 113583, 2021.
66. Aysegul, A., T. Alperen, and A.-M. Amjad, District heating and electricity production based on biogas produced from municipal WWTPs in Turkey: A comprehensive case study. Energy. 223, 119904, 2021.
67. Tozlu, A., Y. Büyükmurat, and E. Özahi, Thermoeconomic analyses of an actual power plant. Turkish Journal of Electromechanics & Energy. 5(1), 2020.
68. Bertrand, M. Pétrissans, and G. Papadakis, Heat resources and organic Rankine cycle machines. Renewable and Sustainable Energy Reviews. 39, 1185-1199, 2014.
69. Karaali, R. and İ.T. Öztürk, Analysis of Steam Injection into Combustion Chamber of Gas Turbine Cogeneration Cycles Hittite Journal of Science and Engineering. 5, 2018.
70. Kilicarslan, A. and M. Kiris, Exergy Destruction Analysis of a Gas Turbine Power Plant. Hittite Journal of Science and Engineering. 5(4), 339-346, 2018.
71. Sarac, B. and T. Ayhan, Exergy Thermodynamic Analysis of Effects of the Inlet Air Cooling on Cycle Performance in Combined Brayton-Diesel Cycle. Hittite Journal of Science and Engineering. 7(1), 2020.
72. Balku, S., Thermal Efficiency Optimization for A Natural-Gas Power Plant. Hittite Journal of Science and Engineering. 4(2), 151-157, 2017.
73. Yılmaz, A. Enerji Atlası. Access time: 13 March 2021. Available from: https://www.enerjiatlasi.com/.

Hittite Journal of Science and Engineering, 2021, 8 (3) 241–246
ISSN NUMBER: 2148–4171
DOI: 10.17350/HJSE19030000234

# Influence of Stem-cell Size and Culture Media Flowing Modality on Cell's Fate within a Microchannel; a Numerical Analysis

**Daver Ali**
Karabuk University, Department of Medical Engineering, Karabuk, Turkey

***Article History:***
*Received: 2021/05/26*
*Accepted: 2021/09/15*
*Online: 2021/09/29*

***Correspondence to**: Daver Ali,*
*Karabuk University, Medical Engineering,*
*Karabuk, TURKEY*
*E-Mail: daverali@karabuk.edu.tr Phone:*
*+90 370 418 70 21*

## ABSTRACT

The dynamic cell culture process has been widely used in tissue engineering. The success of cell culture is influenced by many factors, one of which is how the cells are transferred from the bioreactor to the scaffolds through microchannels. The risk that can reduce the success of the cell culture process is that the cells do not reach the final destination correctly. In this study, the movement of stem cells through a microchannel was theoretically analysed using discrete phase computational fluid dynamics. Three factors of cell size, fluid flow rate and fluid viscosity were investigated on their sedimentation rate before reaching the microchannel outlet. Four sizes of 10, 15, 20 and 30 µm for cells, and four flow rates of 20, 50, 90 and 180 µl/min in addition, four viscosities of 0.001, 0.005, 0.01 and 0.025 Pa.s were selected for culture media left us a total number of 64 models. The analysis results showed that cells with smaller sizes have a better chance of reaching the microchannel outlet, and larger cells are more likely to sediment. On the other hand, higher flow velocities and higher fluid viscosity delivering more cells to the destination. The results of this study shed more light on the regulation and control of dynamic cell culture parameters.

**Keywords:**
Microchannel; Cell culture; Stem-cells; DPM Aanalysis; CFD analysis

## INTRODUCTION

A microfluidic device is a small scale channel that can be exploited in very fine fluid flow volumes. Nowadays, microfluidic systems gain more attention because of their increasing applications in many areas like computers' cooling systems [1], biological lab-on-chips [2], microparticles trapping in air purification [3]. Based on their application, these systems are prepared and used in very different dimensions and geometries. For example, in a microchannel that is used for heat transfer, increasing the wall surface area can increase its efficiency [4], wherein for a microchannel designed for cell tracking or trapping, applied forces on suspended cells are the determining factors that are highly dependent on fluid flow modality [5]. Therefore, based on the microfluidic system applications, very different parameters are considered in their design.

Although small-scale chemistry studies and physics analysis initially influenced microfluidic research, recently, the integration of cell biology with microfluidics has become a significant focus of the scientific community [6]. In biological lab-on-chip systems, microchannels are used as a transporter of suspension from a reservoir to the final destination [7]. Before embarking on research involving complex biological systems containing live cells, the study of various aspects of fluid flow within microscale channels is inevitable. Many studies showed that conventional fluid dynamics theories are generally applicable in microchannels fluid flow analysis [8, 9]. However, due to the small size of the microchannel, parameters such as surface roughness and wettability of their walls can cause differences in the way fluid flows in larger-scale channels [10-12]. Another factor that can add to studying fluid flow in microchannels, especially in biological systems, is the inherent complexity of biological fluids. For example, in terms of viscosity, most biofluids are non-Newtonian fluids [13, 14]. The problem is exacerbated when the microchannel operates in a system such as a cell culture where wall shear stress is a critical parameter to the success of the process [15]. Here the contradictory situation and the difficulty is that a high flow rate increases the wall shear stress at the destination, such as scaffolds walls [16, 17], and a low flow rate can cause microparticles and cells to deposit on the microchannel wall and finally its obstruction [18, 19]. Therefore, finding an optimal flow rate considering the fluid properties and a suspended biological organism's physical aspects like its density and size is still a challenge for researchers.

In a dynamic cell culture system, cells are sent from a bioreactor to a destination, usually a synthetic scaffold. In such a system, microchannels are playing as transporters [20-23]. As with other microchannel systems, in dynamic cell culture, cell deposition can lead to process failure. Factors such as cell clogging [7], van der Waals forces [24], gravity or inertial forces [25] can cause the cells to settle before reaching the destination. Minimizing cell deposition within microchannels needs to control each causative factor sophisticatedly.

In addition to in-vitro studies, in silico simulations in the study of human cells have recently been considered [26-30]. For example, Marin et al. showed experimental and computational that a low flow rate in cell culture can cause cells to sediment in microchannels before reaching the outlet area [31]. In addition, a recent study by the author has performed a discrete phase model to probe the effect of scaffold architecture on the initial attachment of dynamic culture cells [32]. Natu et al. conducted a numerical analysis to examine stem cell movement in a cell sorting microchannel [33]. In a similar work Sun et al. performed a numerical simulation to predict the rare tumor cells movement inside a double spiral microchannel [34]. As can be seen in cell culture studies, computer simulations can provide reliable results, especially cell movement in microchannels.

In dynamic cell culture, the effect of the physical properties of the media can be very significant in process outcomes. For example, Torres et al. showed that adding macromolecules like dextran and Ficoll (Ficoll-Pq) could regulate media viscosity and density in controlling the rate of cell settlement on scaffolds [35]. Another factor affecting cell movement within a microchannel is its physical properties, including size, shape, and density relative to the fluid. Ge et al. showed that stem cells have an almost spherical geometry that varies in diameter from 10 to 35 microns [36]. However, to the author's best knowledge, no study in the literature examines the effects of all these parameters together. To address such a gap in the literature, in this study, the effect of flow rate, cell culture media properties, and the size of the buoyant cells on their sedimentation rate within a fixed size microchannel were investigated theoretically.

**Table 1.** Fluid density and viscosity for CFD analysis.

| Density (kg/m$^3$) | 1000 | 1020 | 1022 | 1024 |
|---|---|---|---|---|
| Dynamic Viscosity (Pa.s) | 0.001 | 0.005 | 0.01 | 0.025 |

# MATERIALS AND METHODS

## Microchannel

As mentioned in the introduction, the effect of fluid physical characteristics and cell size on their passage or settling was investigated in this study. A microchannel with a rectangular cross-sectional area of 3000×1000 μm and a length of 40 mm [31] was designed. The microchannel was used horizontally to take into account the effect of gravitational force on cells.

## CFD Analysis

In this study, the cell culture media was considered a Newtonian and non-compressible fluid, and its flow was considered to be fully developed. Then the Navier-Stokes equation was used in CFD calculations [37]:

$$\rho\frac{\partial u}{\partial t}-\mu\nabla^{2}\mathrm{u}+\rho(\mathrm{u}.\nabla)\mathrm{u}+\nabla\mathrm{p}=\mathrm{F},\ \ \nabla.\mathrm{u}=0 \qquad (1)$$

where, u, and $\mu$ represent the density (kg/m$^3$), velocity (m/s), and the dynamic viscosity of fluid (kg/m.s). ∇ denotes the del operator, and p denotes the pressure (Pa). F represents the forces, such as gravity and centrifugal force [37, 38]. A No-slip boundary condition was assigned on the microchannel wall [39].

## Fluid Properties and Boundary Conditions in CFD

Based on Torres et al. study result [35], four different densities and related viscosity were assigned to the culture media.

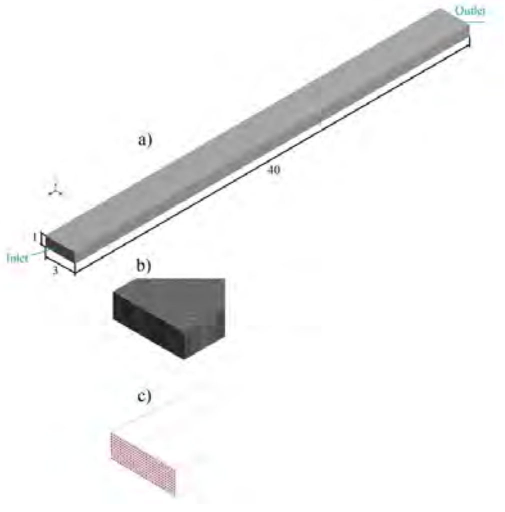

**Figure 1.** The microchannel model used in this study; a) geometry, b) mesh of the CFD analysis, c) cells injection from the inlet surface.

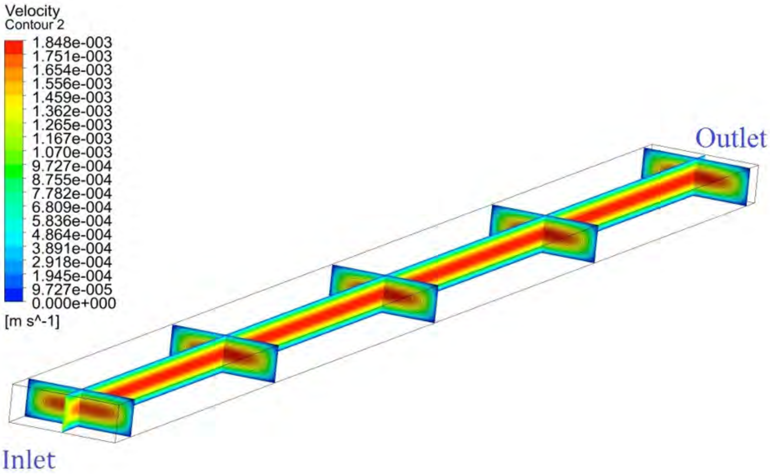

**Figure 2.** Velocity contour for the model with a flow rate of 180 µL/min and media viscosity of 0.005 Pa.s viscosity.

Also, four different inlet flow rates of 20, 50, 90 and 180 µl/min were selected to investigate the effect of fluid velocity on the fate of cells within the microchannel [31]. The microchannel geometry was meshed using hexagonal elements with a size of 50 µm and a total number of 960,000 elements (Fig. 1). For CFD analysis, the criterion of residual sensitivity was set as 1e$^{-6}$.

### Governing Equations in Discrete Phase

Cells motions within microchannels could be explained using particle motion equation[40], which was defined by the following equations:

$$\frac{dU_p}{dt} = \mathrm{F}_d(U - U_p) + \frac{g(\rho_\mathrm{p} - \rho)}{\rho_p} \tag{2}$$

and;

$$\mathrm{F}_d = \frac{18\mu}{\rho_p d_P^4}\frac{C_p.Re}{24} \tag{3}$$

wherein; $U_p$, $\mathrm{F}_d$, $U$, $g$, $\rho_p$, $\rho$, $\mu$, $d_p$, $C_d$, and Re represented particle velocity (m/s), drag force (N), fluid phase velocity (m/s), gravitational acceleration (9.81 m/s$^2$ ), cell density, fluid density, fluid dynamic viscosity, cell diameter, and an empirical drag coefficient factor for spherically-shaped particles [41]; respectively. Stem-cells were assumed as spheroids with 10, 15, 20 and 30 µm diameters in four sizes [36] as well as they were also modelled as a discrete phase with a density of 1130 kg/m$^3$ [27]. Moreover, one-way coupling was considered between cells and media so that only the fluid phase could affect the cells [31]. Three hundred cells were injected using the group injection method from the inlet surface with a zero velocity. This study assumed that the cells adhered to the microchannel walls had once collided with them. To this end, the trap condition was assigned to the interaction type between cells and microchannel walls [27].

## RESULTS

Selecting four sizes for the cells' diameter and four different viscosities plus four flow rates for each model left a total of 64 models in this study. A small Reynolds number for all models ensures that the analysis is performed under a laminar flow (among all the models, the maximum Re = 1.54). Fig. 2 shows fluid flow conditions within the microchannel.

As can be seen, just after the inlet, the flowing fluid maintains its uniform flow contour to the end of the microchannel, indicating a fully developed flow, which was the same in all the models in this study. The streamlines of cells for four different models are shown in Figure to illustrate their fate.

As can be seen, except for the model with 10 µm cell size, in all other models, all the injected cells have settled, and none of them has found a way outlet, indicating a determining role of cell size in how they move along the microchannel.

Fig. 4 shows the percentage of cells that settled before leaving the microchannel for each model.

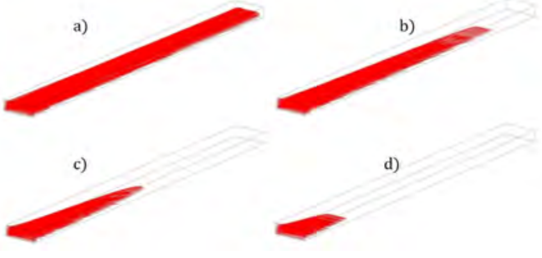

**Figure 3.** The path of the cell from the microchannel inlet for models with a flow rate of 90 µl/min and a viscosity of 0.005 Pa.s and cell size a) 10 µm, b) 15 µm, c) 20 µm and d) 30 µm.

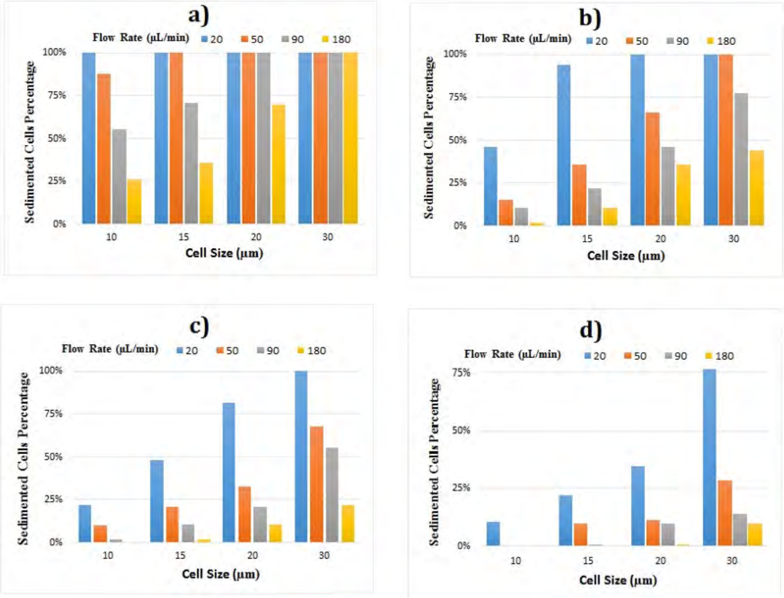

**Figure 4.** The number of sedimented cells was normalized with the total number of injected cells, and the assigned viscosity for the models' media was: a) 0.001, b) 0.005, c) 0.01, and d) 0.025 Pa.s, respectively.

As shown in Fig. 4, all three parameters, namely cell size, viscosity and flow rate, were influential in the rate of cell deposition. In all models, the sedimentation rate increases with increasing cell size. However, increasing the flow rate and viscosity in the models has reduced cell sedimentation. Under a flow rate of 20 μl/min in all models, a significant percentage of cells have been deposited. Also, cells with a size of 30 μm under all flow rates and viscosities selected for the carrying fluid in this study showed a percentage of sediment.

## DISCUSSION

To evaluate the reliability of the results, a part of those was compared with a similar study by Marin et al., which is presented in Table 2. As can be seen, the results are very close.

As shown in Fig. 5, the two main forces acting on a floating cell are drag ($F_d$) and gravitational ($F_W$) forces. According to equation 3, the drag force is a function of viscosity (μ) and flow rate (Re). Also, the gravitational force relates to the mass and volume of the cell.

**Table 2.** The number of sediment cells from 300 injected cells at different flow rates for a model with a cell size of 10 μm and a media viscosity of 0.001 Pa.s in this study and similar work in the literature.

| *Flow Rate (μl/min)* | *Marin el al. [31]* | *Current work* |
|---|---|---|
| *20* | *300* | *300* |
| *50* | *264* | *263* |
| *90* | *166* | *166* |
| *180* | *78* | *78* |

As seen in Fig. 5, drag and ground forces are perpendicular to each other. Therefore, the sum of the two forces is to be predicted to be angled and downward.

According to the result, it can be understood that the trajectory and fate of the cells within the microchannel from the inlet to the outlet more than anything depends on the flow velocity. In all models with a flow rate of 20 μl/min, a significant percentage of cell sediment was observed. Cell size is another highly influential factor in cell movement behaviour through a microchannel following the flow rate. For example, in all models of this study, most of the

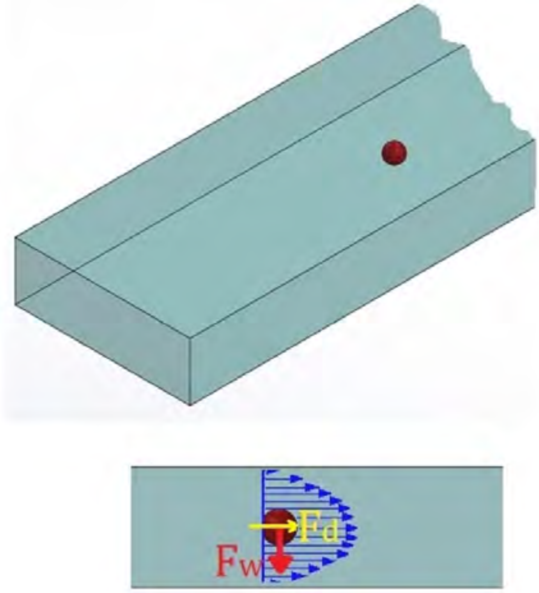

**Figure 5.** Effective forces on a buoyant cell.

injected cells with 30 μm size could not reach the outlet and got stuck in the microchannel. Moreover, the viscosity of the carrier fluid also plays a vital role in the number of trapped cells. With increasing viscosity in all models, more cells reached the microchannel outlet. The movement of cells towards the outlet without deposition depends on the balance between the two main forces, namely the drag force and the gravitational force. Naturally, when the size of the cells increases due to the difference in density with the solution, it experiences more gravitational force and is pulled down. Similarly, when the flow rate or viscosity of the culture media increases, the drag force on a cell increases and can overcome the gravitational force. We can conclude that fewer cells can trap within transport microchannels in dynamic cell culture with increasing flow rate and viscosity. However, an increased viscosity and flow rate can lead to a higher wall shear stress in the destination scaffold surfaces. Therefore, we may need to be careful about increasing the fluid viscosity and the flow rate. Also, the use of cells of the same size can facilitate the regulation and selection of cell culture conditions such as flow rate and viscosity of the media because the presence of cells with various sizes can make it more difficult to control their trajectory. Therefore, having the same size cells can be considered a prerequisite for a successful cell culture process. Other factors such as microchannel material can affect the fluid flow profile and consequently the fate of cells. For example, since PDMS is a hydrophobic material whereas glass is hydrophilic [42], the velocity profile can vary for each of them, and this cause different streamline modality within a microchannel. In this study, the boundary condition of walls was chosen as no-slip, so the microchannel material effect on cells fate is ignored. Since cell subsidence and, consequently, blockage of a micro-device is a catastrophe, solutions such as sheath fluid flow [43], applying dielectrophoresis [44], an increase in wall shear stress to separate cells from microchannel wall [45] can be considered to overcome this phenomenon.

## CONCLUSION

In this study, the movement of stem cells thought of a microchannel was investigated using discrete phase model CFD analysis. Based on the results of this study, the following conclusions can be drawn:

- All three factors, cell size, flow rate and fluid viscosity, play a decisive role in the movement of cells from the inlet to the outlet of a microchannel.

- The presence of three independent parameters makes the regulation and control of the cell culture process difficult and a challenge that can be managed using computer simulations to solve possible problems.

- Having cells of the same size can be an essential step in reducing the challenges of regulating cell culture conditions.

- The results of this study are limited to a microchannel with specific dimensions. In contrast, the microchannel dimensions can play an essential role in fluid flow and, consequently, cell fate. Hence, new and more studies with different size and geometries of the microchannel are necessary.

## CONFLICT OF INTEREST

The author declare no conflicts of interest.

## References

1. Wiriyasart, S., C. Hommalee, and P. Naphon, Thermal cooling enhancement of dual processors computer with thermoelectric air cooler module. Case Studies in Thermal Engineering, 2019. 14: p. 100445.
2. Jayamohan, H., et al., Chapter 11 - Advances in Microfluidics and Lab-on-a-Chip Technologies, in Molecular Diagnostics (Third Edition), G.P. Patrinos, Editor. 2017, Academic Press. p. 197-217.
3. Andrade, J.R., E. Kussul, and T. Baydyk, Microchannel filter for air purification. Open Physics, 2020. 18: p. 241 - 254.
4. Abdollahi, A., et al., Fluid flow and heat transfer of nanofluids in microchannel heat sink with V-type inlet/outlet arrangement. Alexandria Engineering Journal, 2017. 56(1): p. 161-170.
5. Narayanamurthy, V., et al., Microfluidic hydrodynamic trapping for single cell analysis: mechanisms, methods and applications. Analytical Methods, 2017. 9(25): p. 3751-3772.
6. David J. Beebe, a. Glennys A. Mensing, and G.M. Walker, Physics and Applications of Microfluidics in Biology. Annual Review of Biomedical Engineering, 2002. 4(1): p. 261-286.
7. Moghadas, H., et al., Challenge in particle delivery to cells in a microfluidic device. Drug delivery and translational research, 2018. 8(3): p. 830-842.
8. Morini, G.L., Single-phase convective heat transfer in microchannels: a review of experimental results. International Journal of Thermal Sciences, 2004. 43(7): p. 631-651.
9. Hetsroni, G., et al., Fluid flow in micro-channels. International Journal of Heat and Mass Transfer, 2005. 48(10): p. 1982-1998.
10. Jin, Y., et al., Scale and size effects on fluid flow through self-affine rough fractures. International Journal of Heat and Mass Transfer, 2017. 105: p. 443-451.
11. Cui, J. and Y.Y. Cui, Effects of Surface Wettability and Roughness on the Heat Transfer Performance of Fluid Flowing through Microchannels. Energies, 2015. 8(6): p. 5704-5724.
12. Dai, B.M., M.X. Li, and Y.T. Ma, Effect of surface roughness on liquid friction and transition characteristics in micro- and mini-channels. Applied Thermal Engineering, 2014. 67(1-2): p. 283-293.
13. Wyma, A., et al., Non-Newtonian rheology in suspension cell cultures significantly impacts bioreactor shear stress quantification. Biotechnology and Bioengineering, 2018. 115(8): p. 2101-2113.
14. Li, X., et al., In Vitro Recapitulation of Functional Microvessels for the Study of Endothelial Shear Response, Nitric Oxide and [Ca2+]i. PLOS ONE, 2015. 10(5): p. e0126797.
15. Tehranirokh, M., et al., Microfluidic devices for cell cultivation and proliferation. Biomicrofluidics, 2013. 7(5): p. 051502.
16. Lesman, A., Y. Blinder, and S. Levenberg, Modeling of flow-induced shear stress applied on 3D cellular scaffolds: Implications

for vascular tissue engineering. Biotechnology and Bioengineering, 2010. 105(3): p. 645-654.

17. Ali, D., et al., Permeability and fluid flow-induced wall shear stress in bone scaffolds with TPMS and lattice architectures: A CFD analysis. European Journal of Mechanics-B/Fluids, 2020. 79: p. 376-385.
18. Huber, D., et al., Hydrodynamics in Cell Studies. Chemical reviews, 2018. 118(4): p. 2042-2079.
19. Shelby, J.P., et al., A microfluidic model for single-cell capillary obstruction by <em>Plasmodium falciparum</em>-infected erythrocytes. Proceedings of the National Academy of Sciences, 2003. 100(25): p. 14618-14622.
20. Korin, N., et al., Design of well and groove microchannel bioreactors for cell culture. Biotechnology and Bioengineering, 2009. 102(4): p. 1222-1230.
21. Coluccio, M.L., et al., Microfluidic platforms for cell cultures and investigations. Microelectronic Engineering, 2019. 208: p. 14-28.
22. Marimuthu, M. and S. Kim, Continuous oxygen supply in pump-less micro-bioreactor based on microfluidics. BioChip Journal, 2015. 9(1): p. 1-9.
23. Byun, C.K., et al., Pumps for microfluidic cell culture. Electrophoresis, 2014. 35(2-3): p. 245-57.
24. Kendall, K. and A.D. Roberts, van der Waals forces influencing adhesion of cells. Philosophical Transactions of the Royal Society B: Biological Sciences, 2015. 370(1661): p. 20140078.
25. Bao, F., et al., Numerical Study of Nanoparticle Deposition in a Gaseous Microchannel under the Influence of Various Forces. 2021. 12(1).
26. Liu, Z., et al., Cell Seeding Process Experiment and Simulation on Three-Dimensional Polyhedron and Cross-Link Design Scaffolds. Frontiers in Bioengineering and Biotechnology, 2020. 8(104).
27. Olivares, A.L. and D. Lacroix, Simulation of Cell Seeding Within a Three-Dimensional Porous Scaffold: A Fluid-Particle Analysis. Tissue Engineering Part C-Methods, 2012. 18(8): p. 624-631.
28. Robu, A., A. Neagu, and L. Stoicu-Tivadar, Cell seeding of tissue engineering scaffolds studied by Monte Carlo simulations. Stud Health Technol Inform, 2011. 169: p. 882-6.
29. Campos Marin, A. and D. Lacroix, Computational Simulation of Cell Seeding in a Tissue Engineering Scaffold, in Multiscale Mechanobiology in Tissue Engineering, D. Lacroix, et al., Editors. 2019, Springer Singapore: Singapore. p. 81-104.
30. Lee, H., et al., Computational fluid dynamics for enhanced tracheal bioreactor design and long-segment graft recellularization. Scientific Reports, 2021. 11(1): p. 1187.
31. Marin, A.C., et al., μ-Particle tracking velocimetry and computational fluid dynamics study of cell seeding within a 3D porous scaffold. Journal of the Mechanical Behavior of Biomedical Materials, 2017. 75(Supplement C): p. 463-469.
32. Ali, D., Effect of scaffold architecture on cell seeding efficiency: A discrete phase model CFD analysis. Computers in biology and medicine, 2019. 109: p. 62-69.
33. Natu, R. and R. Martinez-Duarte, Numerical Model of Streaming DEP for Stem Cell Sorting. Micromachines, 2016. 7(12): p. 217.
34. Sun, J., et al. Size-based hydrodynamic rare tumor cell separation in curved microfluidic channels. Biomicrofluidics, 2013. 7, 11802 DOI: 10.1063/1.4774311.
35. Cámara-Torres, M., et al., Improving cell distribution on 3D additive manufactured scaffolds through engineered seeding media density and viscosity. Acta Biomaterialia, 2020. 101: p. 183-195.
36. Ge, J., et al., The size of mesenchymal stem cells is a significant cause of vascular obstructions and stroke. Stem Cell Rev Rep, 2014. 10(2): p. 295-303.
37. Vossenberg, P., et al., Darcian permeability constant as indicator for shear stresses in regular scaffold systems for tissue engineering. Biomechanics and Modeling in Mechanobiology, 2009. 8(6): p. 499.
38. Xue, X., et al., Analysis of fluid separation in microfluidic T-channels. Applied Mathematical Modelling, 2012. 36(2): p. 743-755.
39. Ali, D. and S. Sen, Computational fluid dynamics study of the effects of surface roughness on permeability and fluid flow-induced wall shear stress in scaffolds. Annals of biomedical engineering, 2018. 46(12): p. 2023-2035.
40. Morsi, S.A. and A.J. Alexander, An investigation of particle trajectories in two-phase flow systems. Journal of Fluid Mechanics, 2006. 55(2): p. 193-208.
41. Morsi, S.A. and A.J. Alexander, An investigation of particle trajectories in two-phase flow systems. Journal of Fluid Mechanics, 1972. 55(2): p. 193-208.
42. Del Giudice, F., et al., Particle alignment in a viscoelastic liquid flowing in a square-shaped microchannel. Lab on a Chip, 2013. 13(21): p. 4263-4271.
43. Yun, H., K. Kim, and W.G. Lee, Effect of a dual inlet channel on cell loading in microfluidics. Biomicrofluidics, 2014. 8(6): p. 066501-066501.
44. Kang, D.-H., K. Kim, and Y.-J. Kim, An anti-clogging method for improving the performance and lifespan of blood plasma separation devices in real-time and continuous microfluidic systems. Scientific Reports, 2018. 8(1): p. 17015.
45. Couzon, C., A. Duperray, and C. Verdier, Critical stresses for cancer cell detachment in microchannels. Eur Biophys J, 2009. 38(8): p. 1035-47.

Hittite Journal of Science and Engineering, 2021, 8 (3) 247–253
ISSN NUMBER: 2148–4171
DOI: 10.17350/HJSE19030000235

# Caffeic Acid Phenethyl Ester Alleviates Cryodamage to Lung Cancer Cells During Cryopreservation

**Ezgi Avsar Abdik**
Yeditepe University, Department of Genetics and Bioengineering, Istanbul, Turkey

***Article History:***
*Received: 2021/06/10*
*Accepted: 2021/09/23*
*Online: 2021/09/29*

***Correspondence to**: Ezgi Avşar Abdik;*
*e-mail: ezgi.avsar@yeditepe.edu.tr;*
*Phone: +90 (216) 578 0619;*
*Fax: +90 (216) 578 2182.*

## ABSTRACT

Cryopreservation is widely used technique for long-term preservation of viable cells at low temperature. In this process, considering the effects of cryodamage on cells, the application of safe and efficient cryoprotective agents is very important. Caffeic acid phenethyl ester (CAPE) is a natural biological compound which is found in propolis extract and possess beneficial effects such as anti-oxidant, antimicrobial, anti-inflammatory. In the current study was to investigate the cryoprotective effects of CAPE on human lung cancer cell line, A549. Firstly, cells were cryopreserved in freezing medium with/without different concentrations of CAPE (5, 10, and 20 µM). The cells were frozen slowly and kept in liquid nitrogen for one month. After thawing, the cryoprotective effects of CAPE were determined by cell viability, proliferation, colony formation, and gene expression levels. The results showed that 5µM CAPE supplemented freezing medium significantly increased the viability of post thaw A549 cells. 5µM CAPE treatment significantly increased cell proliferation after 24, 48 and 72h since thawing compared to control. 10 µM CAPE did not significantly affect cell viability compared to control group. Also, 5µM CAPE increased the number of A549 colonies compared to 10µM CAPE and control groups. Furthermore, markedly larger colonies were noticed in 5µM CAPE group. In addition, 5µM CAPE significantly increased apoptosis and proliferation-related genes, Akt, NFκB and Bcl-2, expression levels compared to 10µM CAPE and control groups. CAPE may be a potential cryoprotective agent for relieving cryodamage during cryopreservation.

**Keywords:**
Cryopreservation; Cryoprotective agents; CAPE; Lung cancer cell line; Cell viability

## INTRODUCTION

Cryopreservation is a process to preserves viable cells and tissues at very low-temperature conditions for a long period time [1]. Cryopreservation of various cell types is important to ease storage of large quantities, transportation and banking for long periods of time [2]. However, production of reactive oxygen species (ROS), osmotic pressure and ice crystals cause irreversible damage the structure and function of cells undergoing the freezing and thawing processes. Under oxidative stress, accumulation of intracellular ROS production leads to the marked reduction in the viability of freeze-thawed cells and trigger apoptotic cell death. In fact, studies have reported that a relationship between ROS and apoptotic cell death and also compounds with antioxidant properties can inhibit apoptosis by acting as ROS scavengers [3].

During cryopreservation process, the formation of ice crystals can be lethal for viable cells. Fast cooling can causes the death of cells due to intracellular ice formation. In the last few decades, researches have focused on optimization of cryopreservation procedures and the addition of cryoprotective agents (CPAs) to protect cells overcoming freeze–thaw stress. CPAs should have some features such as being able to easily penetrate into the cells and possess low toxicity [4]. Dimethyl sulfoxide (DMSO) is commonly used as CPAs for cryopreservation process, however, it may not be appropriate for cryopreservation of cells are used in clinical practice due to its cytotoxicity. Therefore, there is a need to develop alternatives to reduce the toxic effects of DMSO [5],[6].

Caffeic Acid Phenethyl Ester (CAPE) is a biologically active component existing in propolis extract which is found in the base of the honeybee hives. CAPE is a structurally related to flavonoids and has polyphenolic structures that contains hydroxyl groups. It is a non-toxic and lipophilic antioxidant. Due to its structural features, CAPE exerts numerous beneficial effects such as anti–inflammatory, immunomodulatory, and anti-oxidant [7],[8]. CAPE completely inhibits the ROS production due to its free radical scavenging and anti-oxidant activity [9],[10]. It has been determined that CAPE has no detrimental effect on healthy cells [11]. Furthermore, several studies showed that CAPE plays a protective role to prevent cells from undergoing apoptosis. CAPE can exert anti-apoptotic properties via inhibiting ROS production and caspase activation [11]–[13].

This study was to determine the protective effects of CAPE on human lung carcinoma cell line, A549, after freezing and thawing process during cryopreservation.

## MATERIALS AND METHODS

### Cell Culture and Reagent

Non-small cell lung cancer cell line, A549, was purchased from the ATCC (American Type Culture Collection, Rockville, MD). They were cultured in DMEM-High Glucose (Gibco, UK) supplemented with 10% fetal bovine serum (FBS, Gibco, UK) and 1% Penicillin/Streptomycin/ Amphotericin (PSA, Gibco, UK) under 5% CO2, 95% humidity at 37°C. Cells were trypsinized and passaged after enough confluency ~ 80%.

CAPE (#BCBR2913V, Sigma-Aldrich, USA) was resuspended in DMSO (dimethyl sulfoxide, 1550557, Fisher Scientific, UK) to reach the main stock concentration of 20mM and kept in -20°C.

### Cell Freezing, Thawing and Storage

Freezing and thawing process was performed to show the potential cryoprotective effect of CAPE on lung cancer cell line. Briefly, cells were trypsinized and total cell number were counted using hemocytometer. Cells were divided into four different groups. 1x106 cells from each group were resuspended in 1 mL cell freezing medium (90% FBS, 10% DMSO) with 5, 10 and 20µM CAPE and without (control group, 0 µM CAPE). Then they were frozen in a freezing container at – 80 °C. After 24h incubation, the cryo-vials were transferred and stored into 196°C liquid nitrogen tank. After 30 days storage, the cells were placed in a 37 °C water bath immediately, rinsed with culture medium to reduce detrimental effect of DMSO and centrifuged. Then, the cell pellet was diluted in growth medium for further experiments.

The schematic representation of the experiment is shown in Fig. 1.

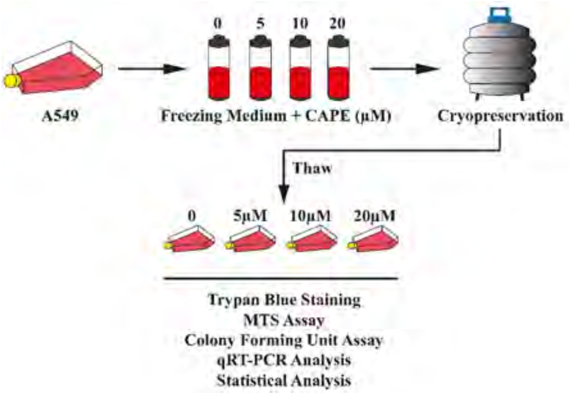

**Figure 1.** The schematic illustration of the experimental design.

### Trypan Blue Staining

Trypan blue staining (T-8154, Sigma-Aldrich) was performed to assess the cell viability. Briefly, after thawing process, cell suspension were mixed with 0.4 % trypan blue (1:1 ratio) and incubated 5 min at room temperature (RT). After the incubation, viable/dead cells were counted using a hemocytometer.

### MTS Assay

MTS (3-(4,5-di-methyl-thiazol-2-yl)-5-(3-carboxymethoxyphenyl)-2-(4-sulfo-phenyl)-2H-tetrazolium) assay (CellTiter96 Aqueous One Solution; Promega, Southampton, UK) was conducted to assess the proliferative effects of CAPE concentrations on the cells. Briefly, cells (5x103) were seeded into 96-well plates for 24, 48 and 72h. After the incubation periods, 10µL MTS solution was added into each wells and incubated for 1h at 37 °C in the dark. The optical density (OD) was read at 495 nm by using ELISA microplate reader (Biotek, Winooski, VT).

### Colony Forming Unit (CFU) Assay

Colony forming unit assay was used to determine the effects of CAPE concentrations on frozen-thawed cells. Briefly, cells were seeded into 6-well plates (300 cells/well) and medium was changed with fresh growth medium five times for 15 days until colonies were visible. Then, 4% paraformaldehyde (PFA) was used to fix colonies for 30min and they were stained with crystal violet dye for 10min. After the incubation, colonies were observed and photographed by ZEISS PrimoVert light microscopy system with AxioCam ICc 5 camera.

### Quantitative Real Time PCR (qRT-PCR) Analysis

Changes in proliferation and apoptosis-related gene expression levels were determined by qRT-PCR analysis. Briefly, cells (150x103) were seeded into 6-well plates. After 24h, total RNAs were isolated using High Pure RNA isolation kit (#11828665001, Roche, USA) and then cDNA was synthesized according to the High Fidelity cDNA synthesis kit (#05081955001, Roche, USA) protocol.

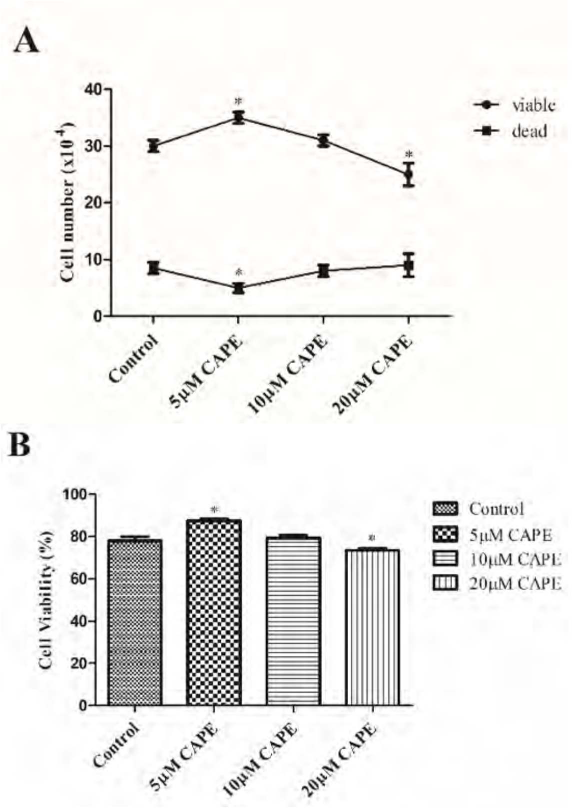

**Figure 2.** Effects of CAPE concentrations (5, 10 and 20μM) on viability of thawed A549 cells were evaluated using trypan blue staining A. The viable (trypan blue-negative) and dead (trypan blue-positive) cell number after cryopreservation. B. Cell viability (%) after cryopreservation in 5, 10 and 20μM CAPE. *P < 0.05.

mRNA levels of the target genes were determined by qRT-PCR with SYBR Green Master Mix (Thermo-Fisher, USA). 2μL cDNAs, 1μL primers, 5μL SYBR-mix (#K0221, Fermentas, USA) and 2μL PCR grade distilled water (#SH30538.02, Hyclone, Utah, USA) in a total volume of 20μl was used for RT-PCR. Primer-BLAST software (National Center for Biotechnology, MD, USA) were used to design AKT, NFκB and BCL-2 primers and Macrogen (Seoul, Korea) synthesized these primers. Data were normalized by a housekeeping gene GAPDH. The CFX96 RT-PCR system was used for RT-PCR experiments (Bio-Rad, Hercules, CA).

### Statistical Analysis

One-way analysis of variance (ANOVA) was used to statistical analysis followed by Tukey's post-hoc test. The data was given as the mean ± SD. Statistical significance was considered as P < 0.05.

## RESULTS

### CAPE Protects Lung Cancer Cells in Cryopreservation Process

The trypan blue staining was used to assess the effects of different CAPE concentrations (5, 10 and 20μM) on the viability of A549 cells. A dose of 5μM CAPE added to freezing medium significantly increased viable and reduced dead cells (Fig. 2A).

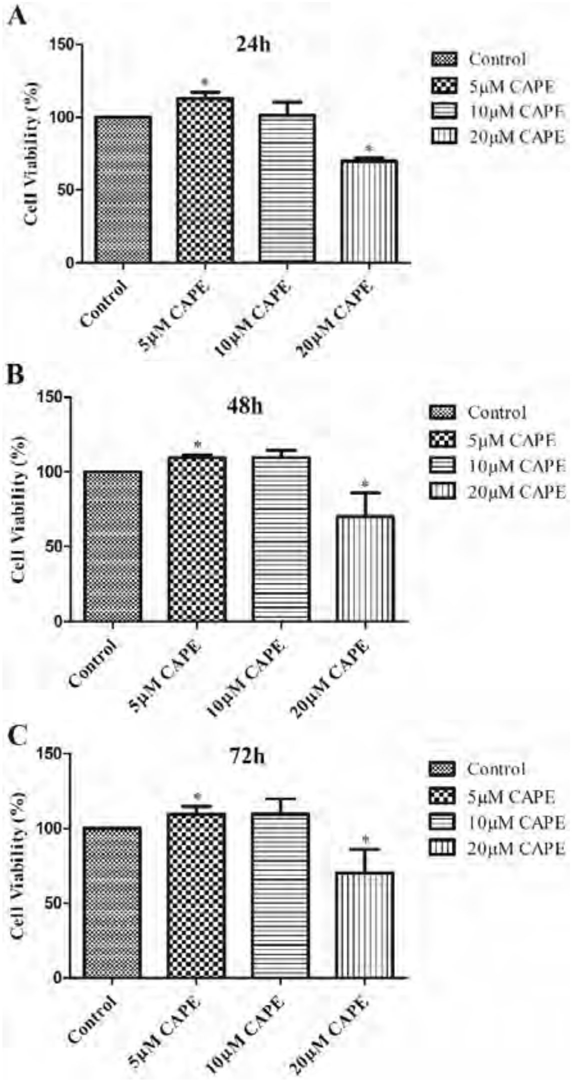

**Figure 3.** Effects of CAPE concentrations (5, 10 and 20μM) on viability of thawed A549 cells for (A) 24, (B) 48 and (C) 72h were evaluated by MTS assay. *P < 0.05.

Cryopreservation medium supplemented with 5μM CAPE notably increased the viability of post-thaw A549 cells (87±1.5%). No significant effects was observed in 10μM CAPE supplemented group (79±0.7%) compared to control (78±1.3%), suggesting that 5μM CAPE was selected for further experiment. However, cryopreservation medium supplemented with 20μM CAPE significantly decreased the viability of post-thaw A549 cells (73±0.5%) (Fig. 2B).

### CAPE Improves the Proliferation of Lung Cancer Cells in Cryopreservation Process

MTS assay was conducted to assess the proliferation for 24, 48 and 72h after thawing process. 5μM CAPE signifi-

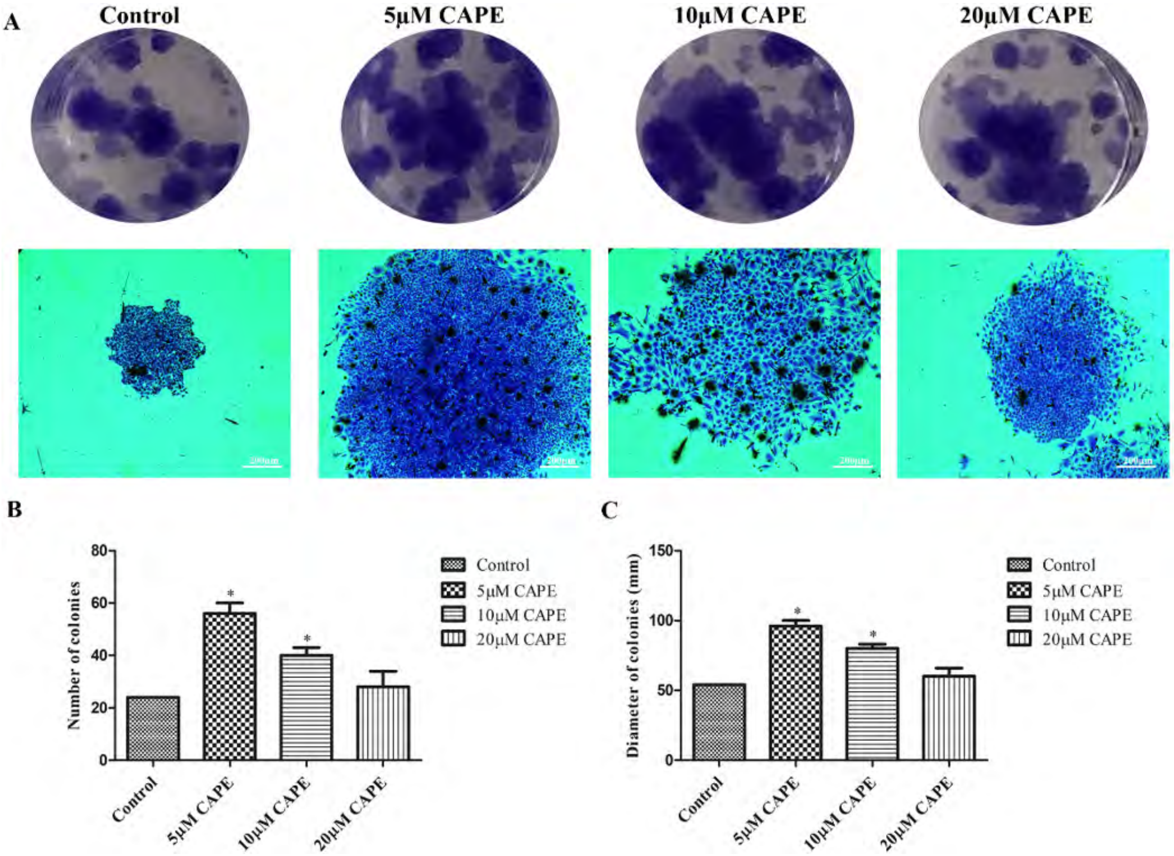

**Figure 4.** Effects of CAPE concentrations (5, 10 and 20µM) on colony forming ability of thawed A549 cells. A. The colony formation ability of A549 cells in each group was assessed by CFU assay. B. Graph shows the number of colonies. C. Graph shows the diameter of colonies. *P < 0.05.

cantly increased cell viability to 112±%4, 109±1%, 118±5% after 24, 48 and 72h, respectively. There was no observed any significant changes in the viability of 10µM CAPE-supplemented group while, at the highest CAPE concentration of 20µM significantly decreased the viability of cells after 24, 48 and 72h after thawing compared to control (Fig. 3).

### CAPE Enhances Colony Forming Capacity of Lung Cancer Cells

CFU assay was assessed the effects of different CAPE concentrations on colony forming capacity of A549 cells after freezing and thawing process. 5 and 10µM CAPE notably increased the number of A549 colonies compared to 20µM CAPE-supplemented and control group. In addition, no significant difference was observed in number of colonies between 20µM CAPE-supplemented and control group. Moreover, dramatically bigger colonies were noticed in 5 and 10µM CAPE-supplemented group. Size of colonies were similar to 20µM CAPE-supplemented and control group (Fig. 4).

### CAPE Changes Gene Expression Profiles of Lung Cancer Cells

qRT-PCR analysis was used to determine the effects of different CAPE concentrations on pro-apoptotic and anti-apoptotic gene expression levels after freezing and thawing process. The addition of 5µM CAPE resulted in a significant upregulation of AKT (~75.9 fold), NFκB (~11.6 fold) and Bcl-2 (~20.2 fold) expression levels. Similarly, 10µM CAPE significantly upregulated AKT (~46.5 fold), NFκB (~5.4 fold) and Bcl-2 (~6.8 fold) gene expression levels. 5 µM CAPE supplementation markedly increased gene expression levels compared to 10 µM CAPE (Fig. 5).

## DISCUSSION

Cryopreservation is a crucial process to preserve viable cells, tissues and organs. Cryopreservation of cells is commonly used in numerous fields such as biotechnology, agricultural and medicine. During freezing process, cryodamage may result in reduced cell viability due to the formation of ice crystal [14]. Cryoprotective agents (CPAs) help to alleviate cryodamage and ice crystals by attenuating the water crystallization and improving the viscosity [15],[16]. Glycerol and dimethyl sulfoxide (DMSO) are well known CPAs for several types of cells, however they have some limitations. Glycerol has relatively weak cryoprotective effect while DMSO can exert

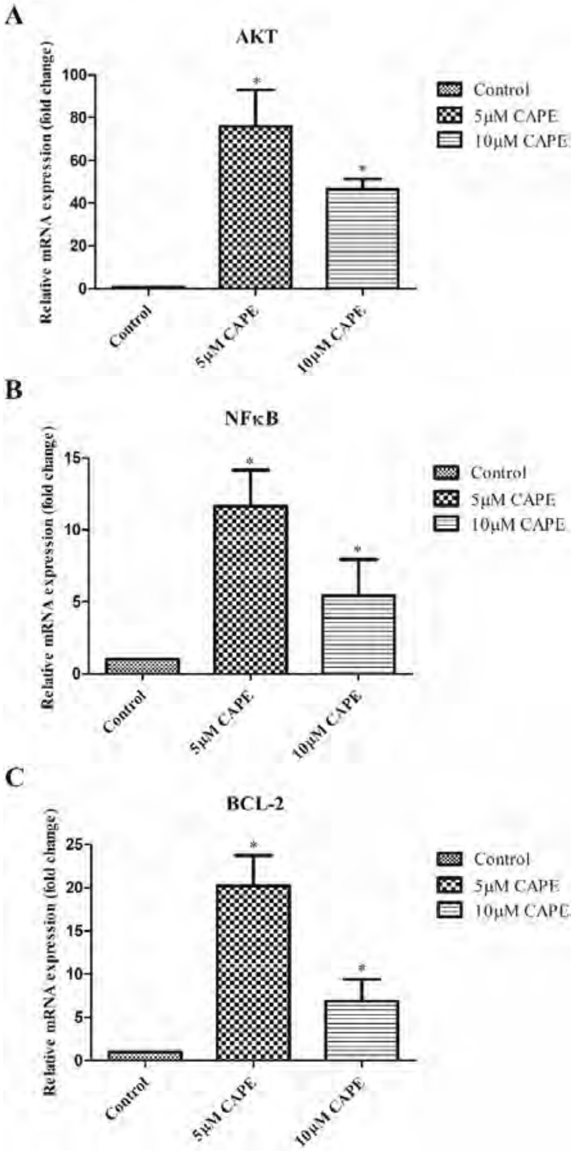

**Figure 5.** Effects of CAPE concentrations (5 and 10µM) on proliferation and apoptosis related gene expression levels (A) AKT, (B) NFκB and (C) BCL-2 of thawed A549 cells. AKT: Protein kinase B, NFκB: Nuclear factor kappa B, BCL2: B-cell lymphoma 2. *$P < 0.05$.

cytotoxic effect and needs to be quickly removed after thawing process [17]. Recent studies mainly focused on two approaches: reducing DMSO concentration and replacing it with more effective and non-toxic agents.

The cryopreservation increases the cellular ROS production [18]. The excessive ROS production induces oxidative stress and impairs the structure, function and viability of cells [19]. Also, increased ROS levels induce cytochrome C release from mitochondria to cytosol via stimulation of mitochondrial membrane permeability transition (MMPT), thereby triggering apoptosis [20]. Furthermore, when abnormal changes occur in physiological conditions, cells begin to reuse their components to produce energy and thereby autophagic cell death is triggered [21]. Non-toxic and effective CPA supplementation in freezing medium to inhibit oxidative stress and apoptosis, significantly improves cryopreservation process [22].

CAPE, a natural phenolic compound, is found in propolis and has beneficial effects such as antioxidant, antimicrobial and immunomodulatory. CAPE is an ester form and a derivative of caffeic acid. Due to its structural properties, CAPE presents high biological activity and able to easily cross the cell membranes than caffeic acid [23]. Several studies have examined the use of caffeic acid on cryopreservation process [24],[25]. Cryopreservation elevates apoptotic biomarkers such as membrane permeability and caspase activation [26]. CAPE can exert anti-apoptotic properties via inhibiting ROS production and caspase activation [11],[12]. However, the effects of CAPE on cryopreservation of cells are still largely unknown, it needs to be elucidated.

This study was evaluated the potential cryoprotective efficiency of CAPE on lung cancer cells. These results showed that the addition of CAPE to the freezing medium significantly increases the viability of A549 cells after cryopreservation process. The number of viable A549 cells was markedly elevated by CAPE included cryopreservation medium. The viability of post-thaw A549 in 5µM CAPE-supplemented group was significantly higher than 10 and 20µM CAPE-supplemented and control groups. 5µM CAPE showed to protect A549 cells to against apoptosis. Moreover, 5µM CAPE was significantly increased the proliferation rates of the cells for 24, 48 and 72h. The proliferation rates of the cells treated with 10µM CAPE was similar to control group. CFU results also supported the cell viability analysis. 5µM CAPE-supplemented group was shown significantly increased colony formation capacity of cells. However, there was no significant change in CFU assay of 10µM and 20µM CAPE-supplemented group, indicating that 5µM CAPE has shown to have a better effect in protecting cell functions. Similar to these results, Li et. al reported that CAPE significantly increase the viability of cells and colony formation capacity [27].

It is known that cryopreservation process change the gene expression profiles of cells [28]. PI3K/AKT signaling leads to the inhibition of apoptotic signaling cascade, which is associated with the production of reactive oxygen species, caspase activation [29]. Akt, a serine/threonine kinase, has a pivotal role in survival and proliferation of cells [30]. The agents with anti-oxidant properties was shown to increase the Akt expression level during cryopreservation [31].

Transcription factor NFκB is a downstream target of Akt and activation of NFκB promote cell survival [32]. Moreover, Bcl-2 family members are major role in regulating apoptosis and cell survival. Upregulation of anti-apoptotic Bcl-2 inhibits apoptosis and promotes cell survival [33]. qRT-PCR analysis revealed that CAPE treatment upregulates the proliferation related gene expression, Akt, NFκB, and anti-apoptotic gene expression level, Bcl-2, in A549 cells. The AKT, NFκB and BCL-2 levels were shown to be increased in A549 cell after freezing and thawing process with 5 and 10μM CAPE. However, 5μM CAPE supplementation has shown significantly upregulated these genes compared to 10μM CAPE. In consistent with these results, previous studies have reported that CAPE reduce apoptotic cell death and induce cell proliferation [34]–[36].

## CONCLUSION

Taken together, the addition of CAPE to the freezing medium increased the viability, colony formation capacity and proliferation related gene expression of post thaw A549 cells. CAPE, a natural compound, may be a promising candidate as a cryoprotective agent for protection of cells from cryodamage and storage of cells without loss of their viability for long periods of time. Further studies are required to understand the underlying the protective mechanisms of CAPE at molecular level and its role in cellular metabolism during cryopreservation process. Additionally, the protective effects of CAPE should be investigated after long term cryopreservation.

## ACKNOWLEDGEMENTS

This study was supported by Yeditepe University.

## CONFLICT OF INTEREST

Authors approve that to the best of their knowledge, there is not any conflict of interest or common interest with an institution/organization or a person that may affect the review process of the paper.

## References

1. Pegg DE. Principles of cryopreservation. In: Cryopreservation and Freeze–Drying Protocols. Springer, (2015) 3–19.
2. Gonda K, Shigeura T, Sato T, Matsumoto D, Suga H, Inoue K, Aoi N, Kato H, Sato K, Murase S, Koshima I, Yoshimura, K. Preserved proliferative capacity and multipotency of human adipose–derived stem cells after long–term cryopreservation. Plastic and reconstructive surgery 121 (2008) 401–410.
3. Nunes VA, Gozzo AJ, Cruz–Silva I, Juliano MA, Viel TA, Godinho RO, Meirelles FV, Sampaio MU, Sampaio CAM, Araujo MS. Vitamin E prevents cell death induced by mild oxidative stress in chicken skeletal muscle cells. Comparative Biochemistry and Physiology Part C: Toxicology & Pharmacology 141 (2005) 225–240.
4. Joshi A. A review and application of cryoprotectant: The science of cryonics. PharmaTutor 4 (2016) 12–18.
5. Luzar A, Chandler D. Structure and hydrogen bond dynamics of water––dimethyl sulfoxide mixtures by computer simulations. The Journal of chemical physics 98 (1993) 8160–8173.
6. Hornberger K, Yu G, McKenna D, Hubel A. Cryopreservation of hematopoietic stem cells: emerging assays, cryoprotectant agents, and technology to improve outcomes. Transfusion Medicine and Hemotherapy 46 (2019) 188–196.
7. Borrelli F, Maffia P, Pinto L, Ianaro A, Russo A, Capasso F, Ialenti A. Phytochemical compounds involved in the anti–inflammatory effect of propolis extract. Fitoterapia 73 (2002) S53––S63.
8. Koltuksuz U, Irmak MK, Karaman A, Uz E, Var A, Ozyurt H, Akyol O. Testicular nitric oxide levels after unilateral testicular torsion/detorsion in rats pretreated with caffeic acid phenethyl ester. Urological research 28 (2000) 360–363.
9. Son S, Lewis BA. Free radical scavenging and antioxidative activity of caffeic acid amide and ester analogues: Structure– activity relationship. Journal of agricultural and food chemistry 50 (2002) 468–472.
10. Zheng Z, Yenari MA. Post–ischemic inflammation: molecular mechanisms and therapeutic implications. Neurological research 26 (2004) 884–892.
11. Guney M, Oral B, Karahan N, Mungan T. Protective effect of caffeic acid phenethyl ester (CAPE) on fluoride–induced oxidative stress and apoptosis in rat endometrium. Environmental toxicology and pharmacology 24 (2007) 86–91.
12. Parlakpinar H, Sahna E, Acet A, Mizrak B, Polat AI. Protective effect of caffeic acid phenethyl ester (CAPE) on myocardial ischemia––reperfusion–induced apoptotic cell death. Toxicology 209 (2005) 1–14.
13. Amodio R, De Ruvo C, Di Matteo V, Poggi A, Di Santo A, Martelli N, Lorenzet R, Rotilio D, Cacchio M, Esposito E. Caffeic acid phenethyl ester blocks apoptosis induced by low potassium in cerebellar granule cells. International journal of developmental neuroscience 21 (2003) 379–389.
14. Isildar B, Ozkan S, Oncul M, Baslar Z, Kaleli S, Tasyurekli M, Koyuturk M. Comparison of different cryopreservation protocols for human umbilical cord tissue as source of mesenchymal stem cells. Acta histochemica 121 (2019) 361–367.
15. Ninagawa T, Eguchi A, Kawamura Y, Konishi T, Narumi A. A study on ice crystal formation behavior at intracellular freezing of plant cells using a high–speed camera. Cryobiology 73 (2016) 20–29.
16. Mazur P. Kinetics of water loss from cells at subzero temperatures and the likelihood of intracellular freezing. The Journal of general physiology 47 (1963) 347–369.
17. Matsumura K, Hyon S–H. Polyampholytes as low toxic efficient cryoprotective agents with antifreeze protein properties. Biomaterials 30 (2009) 4842–4849.
18. Aliakbari F, Gilani MAS, Amidi F, Baazm M, Korouji M, Izadyar F, Yazdekhasti H, Abbasi M. Improving the efficacy of cryopreservation of spermatogonia stem cells by antioxidant supplements. Cellular Reprogramming (Formerly" Cloning and Stem Cells") 18 (2016) 87–95.

19. Shaban S, El-Husseny MWA, Abushouk AI, Salem AMA, Mamdouh M, Abdel-Daim MM. Effects of antioxidant supplements on the survival and differentiation of stem cells. Oxidative Medicine and Cellular Longevity 2017 (2017).
20. Bugger H, Pfeil K. Mitochondrial ROS in myocardial ischemia reperfusion and remodeling. Biochimica et Biophysica Acta (BBA)-Molecular Basis of Disease 1866 (2020) 165768.
21. Singh R, Cuervo AM. Autophagy in the cellular energetic balance. Cell metabolism 13 (2011) 495-504.
22. Feng T-Y, Li Q, Ren F, Xi H-M, Lv D-L, Li Y, Hu J-H. Melatonin Protects Goat Spermatogonial Stem Cells against Oxidative Damage during Cryopreservation by Improving Antioxidant Capacity and Inhibiting Mitochondrial Apoptosis Pathway. Oxidative Medicine and Cellular Longevity 2020 (2020).
23. Song YS, Park E-H, Hur GM, Ryu YS, Lee YS, Lee JY, Kim YM, Jin C. Caffeic acid phenethyl ester inhibits nitric oxide synthase gene expression and enzyme activity. Cancer letters 175 (2002) 53-61.
24. Mahdi NS, Azarbani F, Pirnia A, Abbaszadeh A, Gholami M. The Effect of Caffeic Acid on Spermatogonial Stem Cell-type A Cryopreservation. Reports of Biochemistry & Molecular Biology 7 (2018) 85.
25. Soleimanzadeh A, Talavi N, Yourdshahi VS, Bucak MN. Caffeic acid improves microscopic sperm parameters and antioxidant status of buffalo (Bubalus bubalis) bull semen following freeze-thawing process. Cryobiology 95 (2020) 29-35.
26. Balao da Silva CM, Macias-Garcia B, Miró-Morán A, González-Fernández L, Morillo-Rodriguez A, Ortega-Ferrusola C, Gallardo-Bolaños JM, Stilwell G, Tapia JA, Peña FJ. Melatonin reduces lipid peroxidation and apoptotic-like changes in stallion spermatozoa. Journal of pineal research 51 (2011) 172-179.
27. Liu Y, Zhang B, Zhang J, Wang S, Yao H, He L, Chen L, Yue W, Li Y, Pei X. CAPE promotes the expansion of human umbilical cord blood-derived hematopoietic stem and progenitor cells in vitro. Science China Life Sciences 57 (2014) 188-194.
28. Çalışkan M, Pritchard JK, Ober C, Gilad Y. The effect of freeze-thaw cycles on gene expression levels in lymphoblastoid cell lines. PloS one 9 (2014) e107166.
29. Koppers AJ, Mitchell LA, Wang P, Lin M, Aitken RJ. Phosphoinositide 3-kinase signalling pathway involvement in a truncated apoptotic cascade associated with motility loss and oxidative DNA damage in human spermatozoa. Biochemical Journal 436 (2011) 687-698.
30. Downward J. PI 3-kinase, Akt and cell survival. In: Seminars in Cell & Developmental Biology. Vol 15 (2004) 177-182.
31. Najafi A, Adutwum E, Yari A, Salehi E, Mikaeili S, Dashtestani F, Abolhassani F, Rashki L, Shiasi S, Asadi E. Melatonin affects membrane integrity, intracellular reactive oxygen species, caspase3 activity and AKT phosphorylation in frozen thawed human sperm. Cell and tissue research 372 (2018) 149-159.
32. Fahy BN, Schlieman M, Virudachalam S, Bold RJ. AKT inhibition is associated with chemosensitisation in the pancreatic cancer cell line MIA-PaCa-2. British journal of cancer 89 (2003) 391-397.
33. Braun F, de Carné Trécesson S, Bertin-Ciftci J, Juin P. Protect and serve: Bcl-2 proteins as guardians and rulers of cancer cell survival. Cell Cycle 12 (2013) 2937-2947.
34. Uz E, Söğüt S, Şahin Ş, Var A, Ozyurt H, Güleç M, Akyol O. The protective role of caffeic acid phenethyl ester (CAPE) on testicular tissue after testicular torsion and detorsion. World journal of urology 20 (2002) 264-270.
35. Dilber Y, Inan S, Ercan GA, Sencan A. The role of CAPE in PI3K/AKT/mTOR activation and oxidative stress on testis torsion. Acta histochemica 118 (2016) 31-37.
36. Tolba MF, Omar HA, Azab SS, Khalifa AE, Abdel-Naim AB, Abdel-Rahman SZ. Caffeic acid phenethyl ester: a review of its antioxidant activity, protective effects against ischemia-reperfusion injury and drug adverse reactions. Critical reviews in food science and nutrition 56 (2016) 2183-2190.

Hittite Journal of Science and Engineering, 2021, 8 (3) 255–263
ISSN NUMBER: 2148–4171
DOI: 10.17350/HJSE19030000236

# Evaluation of controlled hydroxychloroquine releasing performance from calcium-alginate beads

**Canan Armutcu** **Sena Piskin**
Hacettepe University, Department of Chemistry, Ankara, Turkey

*Article History:*
*Received: 2021/06/25*
*Accepted: 2021/08/31*
*Online: 2021/09/29*

***Correspondence to**: Canan Armutcu,*
*Hacettepe University, Faculty of Science,*
*Department of Chemistry, TR-06800*
*Ankara, Turkey*
*E-Mail: cananarmutcu@hacettepe.edu.tr*
*Phone: +90 (312) 297 7963*
*Fax: +90 (312) 299 2163*

## ABSTRACT

This study aimed to develop an effective controlled drug delivery system based on alginate beads to treat autoimmune diseases such as Rheumatoid Arthritis (RA) and Systemic Lupus Erythematosus (SLE). The present study describes the drug delivery systems to control the practical uses of hydroxychloroquine (HCQ) by Ca-alginate beads. The characterization techniques were employed to evaluate the physicochemical properties as scanning electron microscopy (SEM), swelling test (S), hydrolytic degradation (weight loss, WL), and Fourier transform infrared-attenuated total reflection (FTIR-ATR). The release studies from alginate beads prepared in various drug doses were carried out in the aqueous solutions at different pH (5–8) and temperatures (4-37°C). The approximately half-amount of HCQ in HCQ-AB3 was released in 12 h, and about 84.38% was released within 8 days. Korsmeyer-Peppas was applied to model the HCQ release kinetic of alginate beads, which corresponded to the non-Fickian transport mechanism.

**Keywords:**
Calcium-alginate beads; hydroxychloroquine; drug delivery; RA; SLE

## INTRODUCTION

Alginate is a well-known and most favored biomaterial found in many applications such as the food sector, textile industry, waste removal, and pharmaceutical industries [1-4]. Alginate is a polysaccharide composed of D-mannuronic acid and *L*-guluronic acid monomers [5,6]. One of the essential properties of alginate is its ability to react with divalent cations and form insoluble crosslinked gels due to the carboxyl groups in the structure. Still, the standard method has been calcium ion gelation to obtain alginate beads [7,8]. Calcium alginate is the most commonly employed system for its easiness of gel formation. Once liquid alginate solutions are contacted with polycation ($Ca^{2+}$), they are immediately transformed into gel binding between guluronic acid blocks in alginate and $Ca^{2+}$. Ca-Alginate beads are widely used in drug delivery due to their favorable properties such as non-toxic, water-soluble, film-forming, biocompatibility, ease of gelation, and biodegradable [9-11].

Controlled drug release is the technique that provides releasing of a drug at the therapeutic dose to the desired site in the body [12,13]. The importance of intelligent drug delivery systems (DDSs) in biomedical and pharmacological fields is growing daily. The main goal of DDSs is to provide drug release for long periods avoiding the side effects of the drugs, that increase the efficacy and safety of drug. The delivery system will also be biocompatible or biodegradable so that it is transformed into non-toxic parts that are eliminated harmlessly from the body [14,15].

Chloroquine (CQ) and its derivate hydroxychloroquine (HCQ) are classified as anti-malarial agents [16]. Although, during the Second World War, the use of anti-malarial as prophylaxis by millions of soldiers, these drugs have been shown for the therapeutic effects in numerous other autoimmune diseases such as Rheumatoid Arthritis (RA) and Systemic Lupus Erythematosus (SLE) [17,18]. HCQ is widely used as it effectively controls dermatological complications in SLE, an autoimmune disease. However, it has been reported to effectively manage the symptoms of Sjøgren syndrome, a chronic autoimmune disease, and prevent thrombosis in phospholipid antibody (aPL) syndrome. It has been observed that HCQ also reduces the risks of atherosclerosis and cardiovascular disease in RA patients [19]. In RA and SLE, HCQ is preferred over CQ owing to the lower incidence of gastrointestinal adverse reactions and its safer dose-dependent toxicity profile [19-21]. HCQ has known controlling inflammatory processes and immunomodulatory effects. In addition, HCQ has a modulating effect on activated immune cells [17,22]. HCQ has also been widely used worldwide as a candidate drug against SARS-CoV-2 infection to treat patients with COVID-19 due to its antiviral effects [23]. This has led to drug shortages and access problems for patients with SLE in many countries and rising anxiety, concerns in patients with SLE [24].

This study is focused on the treatment strategy to a controlled release of HCQ as a model therapeutics. If HCQ is taken in proper doses, it is a safe drug, although its safety margin is narrow, and a single higher dose might be fatal [17]. Therefore, there is a need for randomized, controlled trials with this drug to prove its efficiency and safety for SLE and RA patients due to the potential for drug-induced toxicity.

This study aimed to develop a controlled drug release system for HCQ, selected as a therapeutic model. At the same time, alginate-based beads were chosen as a carrier system. First, alginate was crosslinked with the presence of calcium ions by a peristaltic pump at room temperature for 1 h. Then, obtained alginate beads were characterized by scanning electron microscopy (SEM), swelling test (S), hydrolytic degradation (weight loss, WL) and Fourier transform infrared-attenuated total reflection (FTIR-ATR). The drug delivery experiments were studied to assure safety and appropriate dose use to include well-designed clinical trials in treating SLE and RA disease.

## MATERIAL AND METHOD

### Materials

Alginic acid sodium salt with medium viscosity (from brown algae) and hydroxychloroquine sulfate were purchased from Sigma-Aldrich (St. Louis, MO, USA). Calcium chloride dihydrate was obtained from Merck (Darmstadt, Germany). All other reagents were analytical grade and obtained from Merck.

### Preparation of HCQ loaded alginate beads

Sodium alginate (1%, w/v) was dissolved in deionized water. The alginate solution was stirred to obtain a homogeneous solution without any bubbles at room temperature. Then, the homogeneous mixture was added dropwise into $CaCl_2$ solution (5%, w/v) via peristaltic pump (1 mL/min, flowrate). The obtained spherical alginate beads were kept in the crosslinking solution for 20 min. After filtering the beads, they were transferred into pure ethanol for post-crosslinking/gelation purposes for 20 min and subsequently washed with deionized water. Finally, spherical alginate beads were placed on petri dishes and dried under two different conditions as room temperature and lyophilization. Drug-loaded alginate beads were prepared via the approach mentioned above with HCQ in feeding solution in different amounts of 0.05, 0.1, and 0.2 g. According to the three different drug content, the alginate beads were labeled as HCQ-AB1, HCQ-AB2 and HCQ-AB3, respectively.

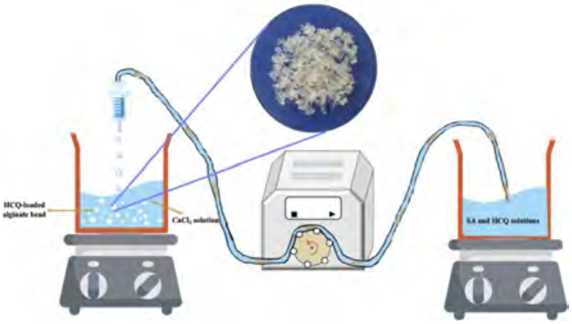

**Figure 1.** Schematic representation for the preparation of HCQ loaded alginate beads.

### Characterization of Alginate Beads

The prepared alginate beads were characterized by the following techniques. The equilibrium swelling degrees of both freeze-dried and air-dried alginate beads were determined by immersing the dried beads (30 mg) into PBS (pH 7.4, 10 mL). The swollen beads were removed from the buffer solution, quickly wiped out with a filter paper, and reweighed ($W_s$) at defined time intervals. The beads weights (dried and wet) were recorded to calculate the percentage swelling rate of beads by the below equation:

$$S\%=[W_s-W_0]x100 \quad (1)$$

Herein, $W_0$ and $W_s$ designated the weights (g) of beads before and after swelling, respectively.

The hydrolytic degradation behavior was also characterized by investigating the weight loss of freeze-dried alginate beads. The initially beads were immersed in PBS (pH 7.4, 10 mL) and incubated by using a temperature-controlled shaking-bath at 37°C at 100 rpm for 8 days. The alginate beads were removed from the PBS and weighted at different intervals. After alginate beads were dried, the hydrolytic degradation behavior was examined. The hydrolytic degradation rate of the developed alginate beads was determined as the percentage of weight loss (WL) by the following equation:

$$WL\%=[(W_0-W_t)/W_0]x100 \quad (2)$$

where $W_0$ is the weight of the initial dry sample and $W_t$ is the weight of the dry sample for a given time t.

To assess the morphology of dried beads, SEM images were obtained with a GAIA3 (Tescan, Czech Republic) utilized from Hacettepe University, Advanced Technologies

Application and Research Center (HUNITEK, Ankara, Turkey). The dried beads were coated with gold and scanned by SEM with different magnifications at a high vacuum. In addition, FTIR-ATR was conducted to characterize the functional groups of alginate beads before and after the degradation process. The FTIR-ATR (Perkin Elmer, Spectrum Two$^{TM}$) spectrum was recorded over the wavenumber range of 4000-400 cm$^{-1}$.

### HCQ encapsulation efficiency

HCQ encapsulation efficiency was investigated by dividing the trapped HCQ amount in the alginate beads by the total amount of HCQ in the alginate solution. The residual HCQ in the $CaCl_2$ gelling and washing solutions was collected and measured by UV/Vis spectrophotometer at 342 nm. HCQ encapsulation efficiency of alginate beads was calculated using the following equation:

$$\text{Encapsulation Efficiency (EE)} = \frac{\text{total HCQ - residual HCQ}}{\text{total HCQ}} \quad (3)$$

### In vitro HCQ release studies

The drug-loaded alginate beads with a different weight (20-50 mg) were placed into a glass bottle containing 4 mL buffer solution in the pH range of 5.0-8.0 and at different temperatures (4-37°C). The drug release studies were performed in an incubator shaker at 100 rpm (JSSB-30T, JSR, Gongju, Korea). At the defined time intervals, 0.4 mL of the buffer solution was taken out and replaced with fresh buffer solution. The released HCQ from the alginate beads was determined at 342 nm using a UV/Vis spectrophotometer (Shimadzu, UV-1280, Tokyo, Japan). For statistical purposes, all the drug release procedures were performed in three replicates to calculate the standard deviation.

## RESULTS AND DISCUSSION

### Characterization studies

Figure 2 shows the swelling ratios of both the freeze-dried and air-dried HCQ-loaded alginate beads in buffer solution at pH 7.4. As shown in the figure, the freeze-dried alginate beads performed higher swelling degrees than the air-dried alginate beads in the equilibrium. The freeze-dried alginate beads showed a moderate swelling degree of 3088% at 6 days, while air-dried alginate beads reached 1142%. These results clearly showed that freeze-dried samples have a higher porosity structure than air-dried alginate beads. In other words, the air-dried alginate beads had a more compact and dense structure than freeze-dried ones. This may be due to the high speed of solvent removal at a high vacuum in the freeze-drying method. In the air-drying method, solvent removal occurs slowly, leading to a less porous structure of the alginate beads [25].

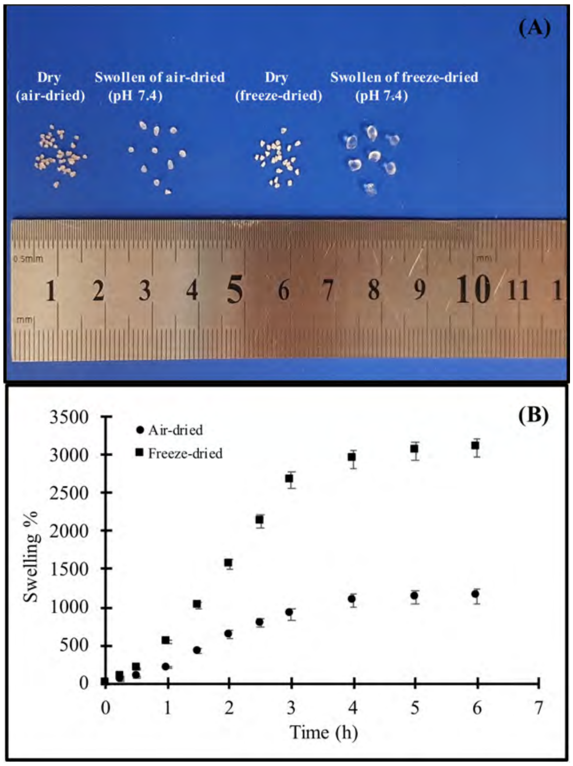

**Figure 2.** Optical images of the prepared dried HCQ-loaded alginate beads (air-dried and freeze-dried) and swollen sizes of air-dried and freeze-dried HCQ-loaded alginate beads in pH 7.4 (A) and swelling degrees of both the freeze-dried and air-dried HCQ-loaded alginate beads in pH 7.4 at 37 °C (B).

To measure the hydrolytic degradation behavior of the freeze-dried HCQ-loaded alginate beads, they were placed in PBS (pH 7.4) at 37 °C for 8 days (Figure 3). The weight loss of alginate beads gradually increased concerning the time as 27.6% after 8 days at pH 7.4 because of the hydrolytic degradation. Thus, it was shown that the freeze-dried HCQ-loaded alginate beads were exhibited a long-term degradation behavior with good stability that makes the prepared alginate beads a good alternative for DDSs.

SEM was used to characterize the morphologies of air and freeze-dried HCQ-loaded alginate beads. The drying method had a significant effect on the beads' regularity and surface morphology. As shown in Figure 4, the air-dried beads (4A) appear more compact, dense, and smoother than freeze-dried beads (4B). Freeze-dried beads had relatively larger sizes and highly porous structures in comparison with air-dried beads due to the lyophilization procedure. The enclosed water in the beads was quickly removed without major deteriorate of the pores during lyophilization. The figure shows that there were relatively rough surfaces and many cavities in the freeze-dried beads integral regions

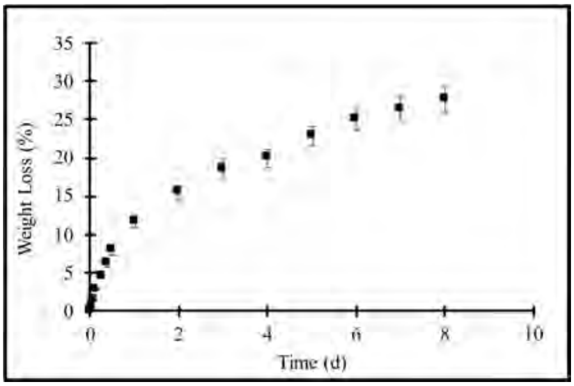

**Figure 3.** Hydrolytic degradation of HCQ-loaded alginate beads in pH 7.4 at 37 °C.

(4D). The porous structure of the freeze-dried beads is suitable for drug delivery due to provide easy penetration of buffer solution into the structure [25,26].

The morphological changes of degraded alginate beads after incubated for 8 days in pH 7.4 at 37°C were also investigated by SEM. There was not any agglomeration in the structure of alginate beads before incubation in pH 7.4 (Figure 5B). The changes of alginate beads structure were observed as soon as incubation was started with the pH 7.4. The morphological changes were observed at alginate beads after 6 h (Figure 5C), 24 h (D) and, 8 days (E, F). As the incubation continued, the rate of degradation was increased, and more conglutination, shrinkages, and the mass loss of the structure of alginate beads were seen (Figure 5E-F). The weight loss of HCQ loaded alginate beads reached 27.6% at 8 days. The SEM images of degraded alginate beads after incubation were evidence of the weight loss results of alginate beads.

Functional groups of HCQ, alginate beads, and HCQ loaded alginate beads were determined using FTIR-ATR spectrometer (Figure 6). The main characteristics bands for HCQ (Figure 6A), -OH stretching peaks were observed at 3200 cm$^{-1}$ and NH deformations bands at approximately 3300 cm$^{-1}$. Moreover, the aromatic C=C stretching bands at 1450 and 1610 cm$^{-1}$ and C-N bands at around 1100 cm$^{-1}$ occurred in the spectrum. Similarly, the C–Cl stretching peak is located between 550 and 850 cm$^{-1}$. The characteristic peaks of HCQ disappear in the HCQ-loaded beads because of the overlap of bands in this region comprising the deformation of -OH, -NH, and -CH. Moreover, there is a decrease in the intensity of 1100 cm$^{-1}$ and 1450 cm$^{-1}$ because of the strong bond stretches of the alginate chain covering the HCQ drug [27]. On the other hand, the spectrum of HCQ loaded alginate beads almost matched up with the spectrum of alginate beads. Only one common peak was detected in HCQ and HCQ-loaded beads different from alginate beads at 1280 cm$^{-1}$, which was exhibited the presence of the C-O stretch. In addition, when the FTIR-ATR spectra of alginate beads were investigated before and after the degradation process (6h, 24h, and 8 days), characteristic peaks intensity was decreased around 1600, 1418, and 1030 cm$^{-1}$, indicating the asymmetric stretching vibration and symmetric stretching vibration of the –COO– group and, C–O–C stretching vibrations, respectively (corresponding figures were also given in Supplementary File, Figure SI-1).

## Encapsulation of Hydroxychloroquine by alginate beads

Encapsulation efficiencies of HCQ loaded alginate beads were calculated by considering the crosslinking and washing processes. The encapsulation efficiencies of HCQ-AB1, HCQ-AB2, and HCQ-AB3 were calculated as 43.98%, 55.77%, 81.22%, respectively. In addition, it was observed an increase in EE with increasing the concentration of HCQ in the alginate beads. In the light of these results, HCQ-AB3 labeled beads was used in all release studies.

## HCQ release studies

For the optimization studies, the effects of medium pH, drug content, beads amount, and temperature were investigated on the alginate beads. The effect of medium pH on HCQ delivery was performed in the appropriate ranges of pH 5.0-8.0, as shown in Figure 7. The release profiles of HCQ from alginate beads exhibited a biphasic delivery system. It was observed to release HCQ at different rates, initial burst release step within 12 hours followed by a constant rate (ideally) and sustained release. As observed in Figure 7., the medium pH significantly affected the HCQ release properties. As seen from Figure 7A, the amount of HCQ released at pH 5.0 was relatively low and only about 9.5%, while this value was 24.5% for pH 7.4 within 60 min. The low drug release ratio is due to the shrinkage and less swelling of the alginate beads in acidic buffer [1]. HCQ release amounts were 14.48%, 17.89%, 23.89%, 42.36%, and 30.92% in 12 h at pH values of 5.0, 6.0, 7.0, 7.4 and 8.0, respectively. After the immediate releasing phase, the cumulative release was 84.38% at pH 7.4 after 192 h.

The cumulative release of HCQ from alginate beads at different amounts of HCQ loadings is seen in Figure 8. It was seen that the cumulative release of HCQ was increased from 38.76 to 84.38% with the increasing amount of HCQ from 50 to 200 mg. Moreover, the release profile of drugs from HCQ-AB3 realized fast and higher release rates about 2.5-fold than HCQ-AB1 within 12 h. The higher drug amount in the alginate beads resulted in the faster diffusion rate of HCQ from the alginate beads, which cause a higher release rate of HCQ, especially in the early stage of the release

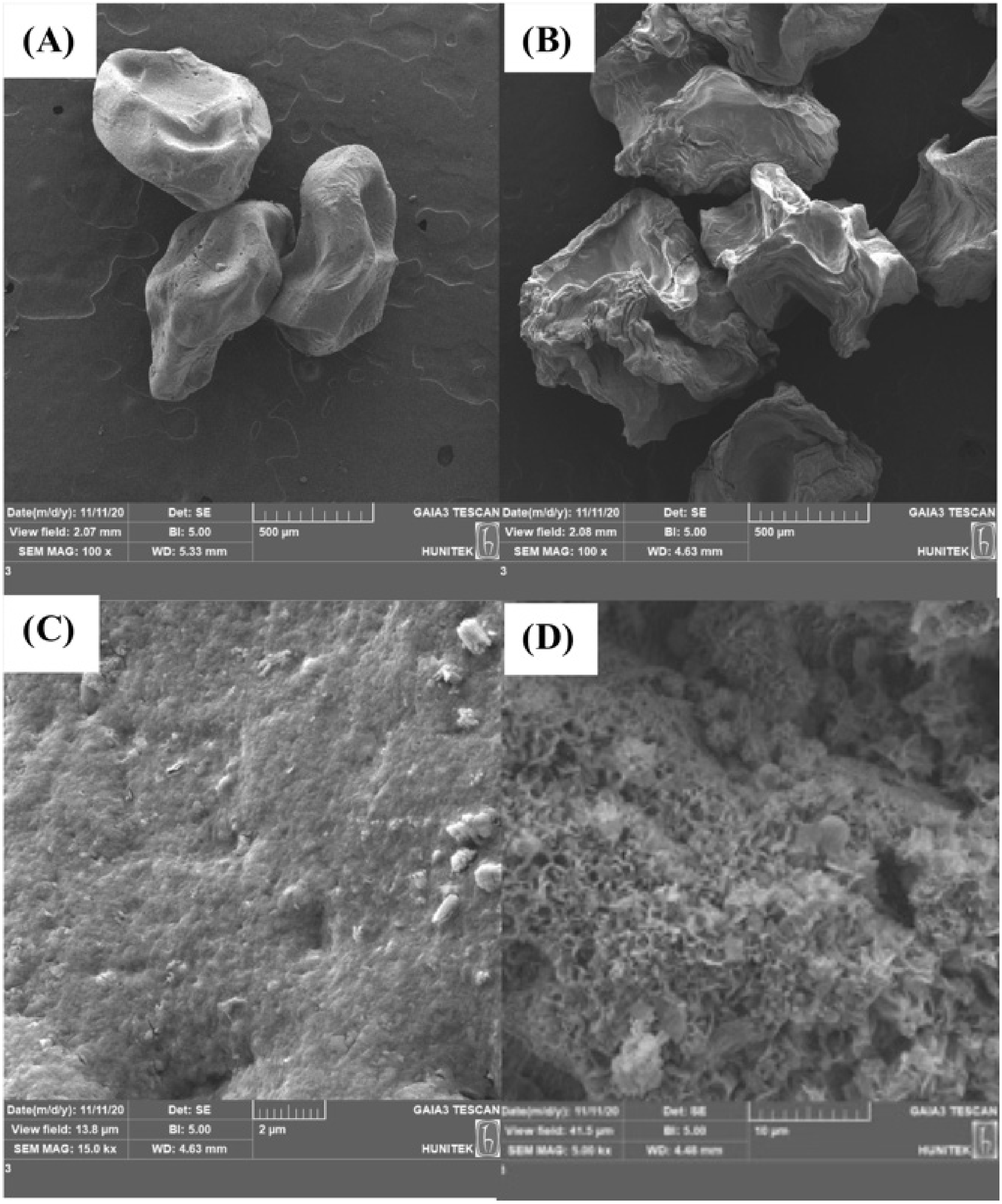

**Figure 4.** SEM images of air-dried (A, C) and freeze-dried HCQ-loaded alginate beads (B, D).

process [28]. Another reason for the increase in the amount of released drugs is that the drug delivery systems are swelling controlled. Therefore, when the alginate begins to absorb water, it causes a more significant amount of drug diffuses in the mass of the swelling bath [29].

The effect of temperature on the HCQ release profile was carried out at 4, 25, and 37°C, and HCQ release data was presented in Figure 9. The HCQ release was 84.38% after 8 days at 37°C, whereas the value was less than 32.52% at 4°C with the same treatment. The increasing temperature promotes the penetration of buffer solution into the beads, which enhances swelling of alginate sites in beads and causes the squeezing out of the drug [30].

The effect of HCQ-AB3 bead amounts on the cumulative release was determined by using various bead amounts (20-50 mg beads). As seen from Figure 10, the maximum

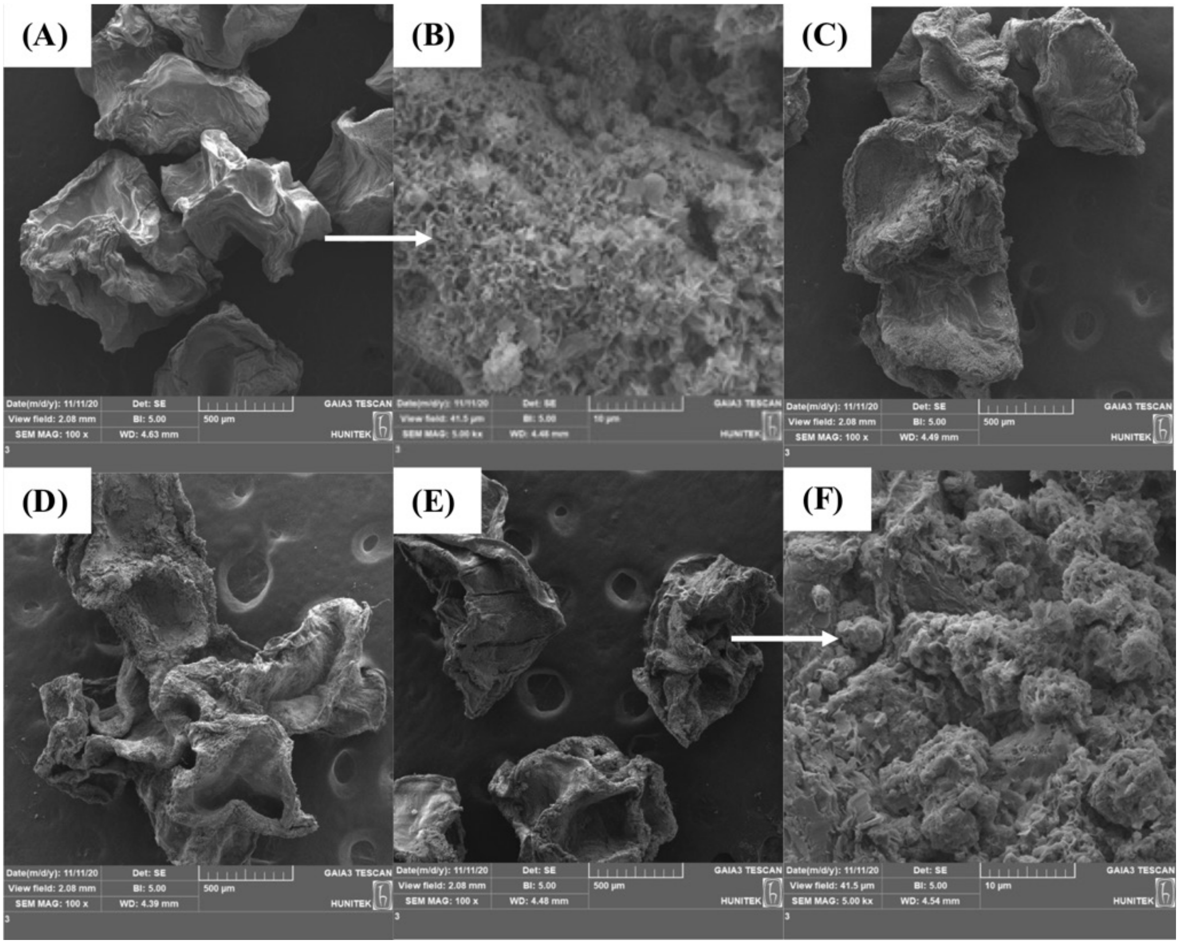

**Figure 5.** SEM images of freeze-dried HCQ loaded alginate beads before and after incubation at 37°C in pH 7.4. Freeze-dried HCQ loaded alginate beads (A, B), after 6 hours (C), after 24 hours (D), after 8 days (E, F).

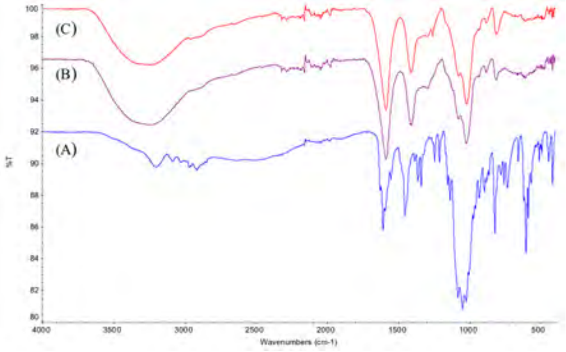

**Figure 6.** FTIR-ATR spectra of HCQ (A), alginate beads (B), and HCQ loaded alginate beads (C).

cumulative release was realized with 30 mg of HCQ-AB3 alginate beads both the first 12 h and 8 days. The lower cumulative releases of HCQ were obtained at high bead amounts. The amount of the beads and the dose of the drug in the beads are significant to show the effect of the released active substance. Undesirable effects may occur when the dose rate falls below the sufficient amount or rises above the toxic level. The result figured out that the amount of beads to be used is significant for controlling the release performances.

## Release kinetic studies of HCQ

To understand the release profile of HCQ from HCQ-Alginate beads, the release data were analyzed using a classic empirical equation:

$$\frac{M_t}{M_\infty}=kt^n \tag{4}$$

where $M_t$ means the amount of drug release at time t, $M_\infty$ describes the amount of drug release at an infinite time, k is the release kinetic constant at the Korsmeyer-Peppas model. The release exponent is n which is related to the geometry of the release system and indicates the release mechanism. The Korsmeyer-Peppas equation can adequately describe the release of drugs from spheres [31,32]. When the value of 0.43 or less than 0.43, the release mechanism is based on diffusion (Fickian diffusion or quasi-Fickian diffusion). If the value of between 0.43 and 0.85, the release mechanism is based on an anomalous diffusion or non-Fickian diffusion (i.e., a mixed diffusion, polymer relaxation). Moreover, the value above 0.85, the release mechanism is based on a Case-

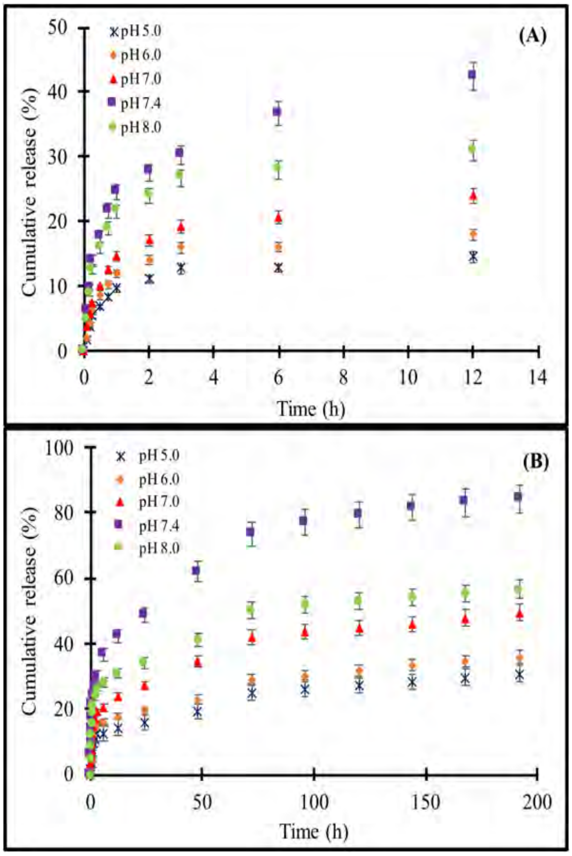

**Figure 7.** SEM images of freeze-dried HCQ loaded alginate beads before and after incubation at 37°C in pH 7.4. Freeze-dried HCQ loaded alginate beads (A, B), after 6 hours (C), after 24 hours (D), after 8 days (E, F).

II transport related to polymer relaxation on the drug molecules movement during gel swelling [33,34]. The correlation coefficient ($R^2$) was used to evaluate the fitness of the model.

Table 1 presented the release exponent (n) values and correlation coefficient ($R^2$) for HCQ-alginate beads. The exponent values ($0.43<n<0.85$) demonstrated that the drug release mechanism was anomalous diffusion for each bead. According to the Korsmeyer-Peppas model, the drug release mechanism of HCQ-Alginate beads observed both diffusion and swelling controlled drug release (anomalous diffusion) [33,35]. In general, the release kinetics of alginate beads fitted well with the Korsmeyer-Peppas model ($R^2 > 0.97$).

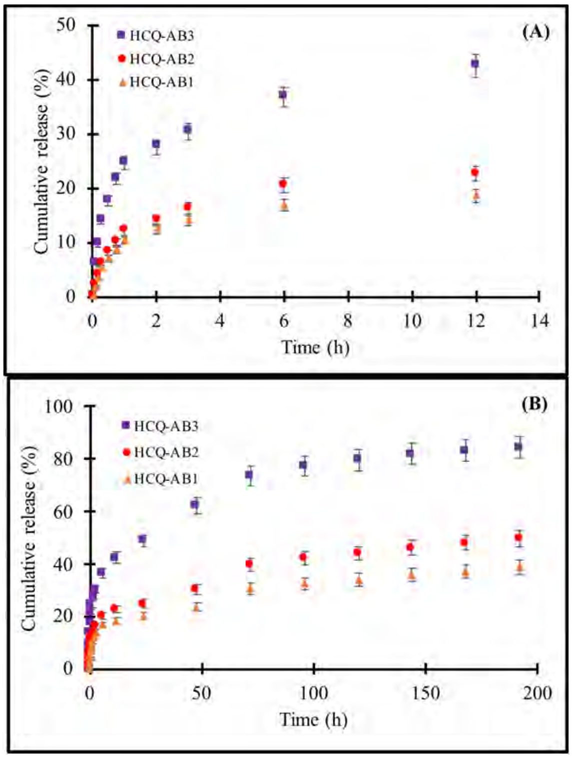

**Figure 8.** Cumulative release of HCQ from alginate beads containing different drug amounts at pH 7.4 at 37 °C. HCQ release (A) for 12 h and (B) for 8 days.

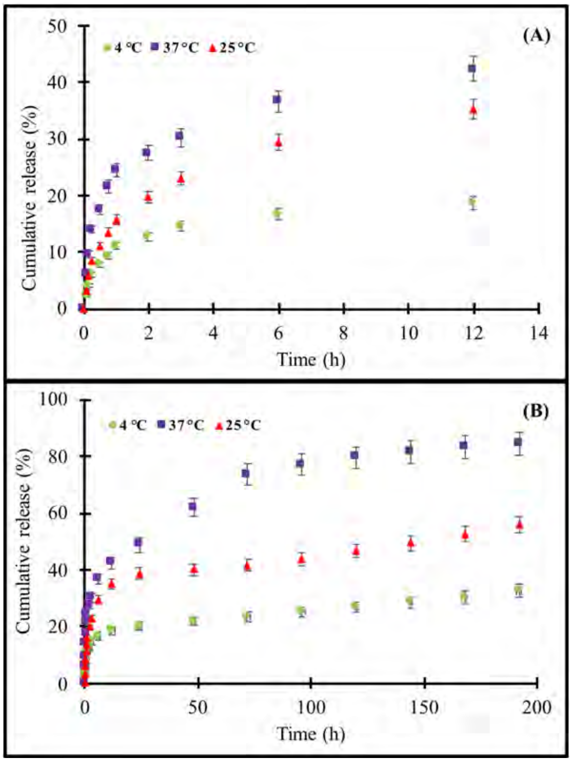

**Figure 9.** Cumulative release of HCQ from HCQ-AB3 at a different temperature at pH 7.4. HCQ release (A) for 12 h and (B) for 8 days.

## CONCLUSIONS

In this study, HCQ was encapsulated in alginate beads to use a controlled drug release system. The obtained data demonstrated a significant effect of the drying method on the characteristics of the prepared alginate beads. The highest HCQ encapsulation efficiency (84.38%) was obtained with the HCQ-AB3 formulation, which exhibited biphasic delivery systems at different rates to assure appropriate dose use and safety. Alginate beads loaded with HCQ showed drug release for 8 days with a moderate burst release of 42.36% within 12 h. Korsmeyer-Peppas model showed that the drug release mechanism was ano-

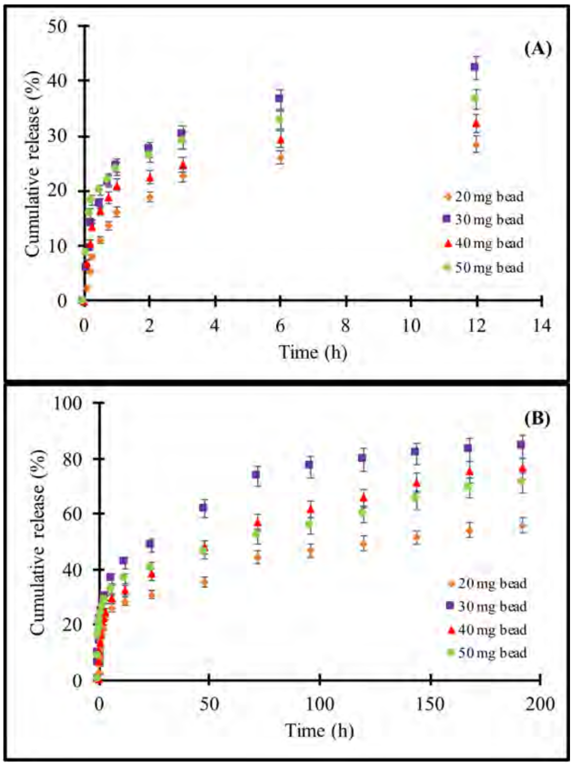

**Figure 10.** Cumulative release of HCQ from HCQ-AB3 at various bead amounts at pH 7.4 at 37 °C. HCQ release (A) for 12 h and (B) for 8 days.

**Table 1.** Values of the release exponent (n) and correlation coefficients ($R^2$) for HCQ-Alginate beads at pH 7.4 at 37 °C.

| Polymer code | n | $R^2$ |
|---|---|---|
| **HCQ-AB1** | 0.7332 | 0.9774 |
| **HCQ-AB2** | 0.6936 | 0.9897 |
| **HCQ-AB3** | 0.5587 | 0.9969 |

malous diffusion, i.e., HCQ could release at pH 7.4 in a controlled manner.

## CONFLICT OF INTEREST

Authors approve that to the best of their knowledge, there is not any conflict of interest or common interest with an institution/organization or a person that may affect the review process of the paper.

## AUTHOR CONTRIBUTION

Sena Piskin: Writing - original draft, Visualization, Investigation. Canan Armutcu: Supervision, Conceptualization, Writing - review & editing.

## References

1. Kaygusuz H, Erim F. Alginate/BSA/montmorillonite composites with enhanced protein entrapment and controlled release efficiency. Reactive & Functional Polymers 73 (2013) 1420-1425.
2. Kaygusuz H, Torlak E, Akın-Evingür G, Özen İ, Von Klitzing R, Erim FB. Antimicrobial cerium ion-chitosan crosslinked alginate biopolymer films: A novel and potential wound dressing. International Journal of Biological Macromolecules 105 (2017) 1161-1165.
3. Tamahkar E, Özkahraman B, Özbaş Z, Izbudak B, Yarimcan F, Boran F, Öztürk AB. Aloe vera-based antibacterial porous sponges for wound dressing applications. Journal of Porous Materials 28 (2021) 741-750.
4. Hussain S, Abid MA, Munawar KS, Saddiqa A, Iqbal M, Suleman M, Hussain M, Riaz M, Ahmad T, Abbas A, Rehman M, Amjad M. Choice of Suitable Economic Adsorbents for the Reduction of Heavy Metal Pollution Load. Polish Journal of Environmental Studies 30 (2021) 1-11.
5. Jayakumar R, Rajkumar M, Freitas H, Selvamurugan N, Nair SV, Furuike T, Tamura H. Preparation, characterization, bioactive and metal uptake studies of alginate/phosphorylated chitin blend films. International Journal of Biological Macromolecules 44 (2009) 107-111.
6. Liu C-m, He X-h, Liang R-h, Liu W, Guo WL, Chen J. Relating physicochemical properties of alginate-HMP complexes to their performance as drug delivery systems. Journal of Biomaterials Science, Polymer Edition 28 (2017) 2242-2254.
7. Alexander BR, Murphy KE, Gallagher J, Farrell GF, Taggart G. Gelation time, homogeneity, and rupture testing of alginate-calcium carbonate-hydrogen peroxide gels for use as wound dressings. Journal of Biomedical Materials Research Part B: Applied Biomaterials 100 (2012) 425-431.
8. Liparoti S, Speranza V, Marra F. Alginate hydrogel: The influence of the hardening on the rheological behaviour. Journal of the Mechanical Behavior of Biomedical Materials 116 (2021) 104341.
9. Gowri M, Latha N, Suganya K, Murugan M, Rajan M. Calcium alginate nanoparticle crosslinked phosphorylated polyallylamine to the controlled release of clindamycin for osteomyelitis treatment. Drug Development and Industrial Pharmacy 47 (2021) 280-291.
10. Lin N, Gèze A, Wouessidjewe D, Huang J, Dufresne A. Biocompatible double-membrane hydrogels from cationic cellulose nanocrystals and anionic alginate as complexing drugs codelivery. ACS Applied Materials & Interfaces 8 (2016) 6880-6889.
11. Pongjanyakul T, Rongthong T. Enhanced entrapment efficiency and modulated drug release of alginate beads loaded with drug–clay intercalated complexes as microreservoirs. Carbohydrate Polymers 81 (2010) 409-419.
12. Alvarez-Lorenzo C, Concheiro A. 15 Review of Smart Materials for Controlled Drug Release. Fundamentals of Smart Materials (2020) 170.
13. Ravi Kumar MN, Kumar § N. Polymeric controlled drug-delivery systems: perspective issues and opportunities. Drug Development and Industrial Pharmacy 27 (2001) 1-30.
14. Cunliffe D, Kirby A, Alexander C. Molecularly imprinted drug delivery systems. Advanced Drug Delivery Reviews 57 (2005) 1836-1853.
15. Lee E, Kim S, Seong K, Park H, Seo H, Khang G, Lee D. A biodegradable and biocompatible drug-delivery system based on polyoxalate microparticles. Journal of Biomaterials Science, Polymer Edition 22 (2011) 1683-1694.
16. da Silva AEA, de Abreu PMB, Geraldes DC, de Oliveira Nascimento L. Hydroxychloroquine: Pharmacological, physicochemical aspects and activity enhancement through experimental formulations. Journal of Drug Delivery Science and Technology 63 (2021) 102512.
17. Ben-Zvi I, Kivity S, Langevitz P, Shoenfeld, Y. Hydroxychloroquine: from malaria to autoimmunity. Clinical Reviews in Allergy &

Immunology 42 (2012) 145-153.

18. Walls AC, Park Y-J, Tortorici MA, Wall A, McGuire AT, Veesler D. Structure, function, and antigenicity of the SARS-CoV-2 spike glycoprotein. Cell 181 (2020) 281-292.
19. Rainsford K, Parke AL, Clifford-Rashotte M, Kean WF. Therapy and pharmacological properties of hydroxychloroquine and chloroquine in treatment of systemic lupus erythematosus, rheumatoid arthritis and related diseases. Inflammopharmacology 23 (2015) 231-269.
20. Jamalipour Soufi G, Iravani S. Potential inhibitors of SARS-CoV-2: recent advances. Journal of Drug Targeting 29 (2021) 349-364.
21. Tan YW, Yam WK, Sun J, Chu JJH. An evaluation of chloroquine as a broad-acting antiviral against hand, foot and mouth disease. Antiviral Research 149 (2018) 143-149.
22. Jorge AM, Melles RB, Zhang Y, Lu N, Rai SK, Young LH, Costenbader KH, Ramsey-Goldman R, Lim SS, Esdaile JM, Clarke AE, Urowitz MB, Askanse A, Aranow C, Petri M, Choi H. Hydroxychloroquine prescription trends and predictors for excess dosing per recent ophthalmology guidelines. Arthritis Research & Therapy 20 (2018) 1-8.
23. McKee DL, Sternberg A, Stange U, Laufer S, Naujokat C. Candidate drugs against SARS-CoV-2 and COVID-19. Pharmacological Research 157 (2020) 104859.
24. Cornet A, Andersen J, Tani C, Mosca M. Hydroxychloroquine availability during COVID-19 crisis and its effect on patient anxiety. Lupus Science & Medicine 8 (2021) e000496.
25. El-Sherbiny IM, Abdel-Mogib M, Dawidar A-AM, Elsayed A, Smyth HD. Biodegradable pH-responsive alginate-poly (lactic-co-glycolic acid) nano/micro hydrogel matrices for oral delivery of silymarin. Carbohydrate Polymers 83 (2011) 1345-1354.
26. George M, Abraham T. pH sensitive alginate–guar gum hydrogel for the controlled delivery of protein drugs. International journal of pharmaceutics 335 (2007) 123-129.
27. Moraes ANF, Silva LAD, de Oliveira MA, de Oliveira EM, Nascimento TL, Lima E M, Torres LMS, Diniz DGA. Compatibility study of hydroxychloroquine sulfate with pharmaceutical excipients using thermal and nonthermal techniques for the development of hard capsules. Journal of Thermal Analysis and Calorimetry 140 (2020) 2283-2292.
28. Çetin K, Alkan H, Bereli N, Denizli A. Molecularly imprinted cryogel as a pH-responsive delivery system for doxorubicin. Journal of Macromolecular Science, Part A 54 (2017) 502-508.
29. Prabhakar S, Bajpai J, Bajpai AK, Tiwari A. Cumulative release of cefotaxim from interpenetrating networks of poly (vinyl alcohol-g-acrylamide) and chitosan-g-polyacrylamide chains. Polymer Bulletin 71 (2014) 977-988.
30. Shi J, Zhang Z, Li G, Cao S. Biomimetic fabrication of alginate/CaCO 3 hybrid beads for dual-responsive drug delivery under compressed CO 2. Journal of Materials Chemistry 21 (2011) 16028-16034.
31. Ritger PL, Peppas NA. A simple equation for description of solute release I. Fickian and non-fickian release from non-swellable devices in the form of slabs, spheres, cylinders or discs. Journal of Controlled Release 5 (1987) 23-36.
32. Sanson C, Schatz C, Le Meins J-F, Soum A, Thévenot J, Garanger E, Lecommandoux S. A simple method to achieve high doxorubicin loading in biodegradable polymersomes. Journal of Controlled Release 147 (2010) 428-435.
33. Pasparakis G, Bouropoulos N. Swelling studies and in vitro release of verapamil from calcium alginate and calcium alginate–chitosan beads. International Journal of Pharmaceutics 323 (2006) 34-42.
34. Ritger PL, Peppas NA. A simple equation for description of solute release II. Fickian and anomalous release from swellable devices. Journal of Controlled Release 5 (1987) 37-42.
35. Peppas N. Analysis of Fickian and non-Fickian drug release from polymers. Pharmaceutica Acta Helvetiae 60 (1985) 110-111.

Hittite Journal of Science and Engineering, 2021, 8 (3) 265–265
ISSN NUMBER: 2148–4171
DOI: 10.17350/HJSE19030000237

# Erratum to: Some Serum Oxidative Parameters in Normoglycemic Rats: Vascular Endothelial Growth Factor (VEGF) Application

**Kaan Kaltalioglu**[1] **Sule Coskun Cevher**[2]
[1]Giresun University, Espiye Vocational School, Giresun, Turkey
[2]Gazi University, Department of Biology, Ankara, Turkey

***Article History:***
*Received: 2021/07/10*
*Accepted: 2021/07/15*
*Online: 2021/09/29*

***Correspondence to**: Sule Coskun Cevher, Gazi University, Science Faculty, Biology Department, 06500, Ankara, Turkey*
*E-Mail: sule@gazi.edu.tr*
*Phone: +90 (312) 202 1196*
*Fax:+90 (312) 202 1171*

## CAUSE OF ERRATUM

After publication of this work [E1], it has come to our attention that there is a typographical error in the section of Material and Methods. Immediately, we requested from the journal for the correction of the error as follows.

## MATERIAL AND METHODS

.........Local Ethics Committee for Animal Experiments (G.Ü. ET-10.118).

## References

E1. Kaltalioglu K, Cevher S. Some Serum Oxidative Parameters in Normoglycemic Rats: Vascular Endothelial Growth Factor (VEGF) Application. Hittite Journal of Science and Engineering 7 (2020): 55-59.

Hittite Journal of Science and Engineering, 2021, 8 (3) 267–272
ISSN NUMBER: 2148–4171
DOI: 10.17350/HJSE19030000238

# Anti-helmintic Activity of *Myrtus communis* L. Fruit Ethanol Extract on Nematodes of *Caenorhabditis elegans* and The Determination of Possible Active Ingredients

**Hulya Ozpinar**
Sivas Cumhuriyet University, Department of Pharmaceutical Botany, Sivas, Turkey

***Article History:***
*Received: 2021/08/17*
*Accepted: 2021/08/26*
*Online: 2021/09/29*

***Correspondence to**: Hulya Ozpinar, Sivas Cumhuriyet University, Faculty of Pharmacy, Department of Pharmaceutical Botany, 58140 Sivas/Turkey*
*E-Mail: hulya1177@yahoo.com.tr*

## ABSTRACT

*Myrtus communis* L. (Myrtaceae) is a plant widely found in the Middle East and Mediterranean region, both naturally grown and cultivated. In our study, *C. elegans* nematodes were used as an anti-helminthic model and by determining the anti-helmintic effect of *Myrtus communis* L. fruit, it was aimed to find the active ingredients with possible anti-helmintic effects by GC-MS analysis. In our study, the anthelmintic effect of the ethanol extract of *Myrtus communis* L. fruit on *C. elegans* was investigated. Ethanol fruit extracts were added to NGM separately at final volume of 10 mg/mL, 5 mg/mL, 2.5 mg/mL, 1.25 mg/mL and experimental groups were formed. When the data were evaluated statistically, the difference between all experimental groups, negative control group and positive control group (pyrantel pamoate), was significant ($p<0.05$). According to the results of GC-MS analysis, the highest detected ingredients were 1,8-Cineole (3.46%), Linalyl acetate (3.06%), and Palmitic acid (2.90%). It was observed that *Myrtus communis* L. fruit extract was more effective on *C. elegans* nematodes than pyrantel pamoate at the same concentration (5 mg/mL), and 20 different active ingredients were determined according to our GC-MS analysis results. By studying the forms of these active ingredients separately or in different combinations, the ingredients and combinations with the strongest anti-helmintic activity can be determined, and it is thought that our findings may lead to further studies.

**Keywords:**
*Myrtus communis* L.; *Caenorhabditis elegans*; anti-helmintic effect; 1,8-Cineole; Linalyl acetate; Palmitic acid

## INTRODUCTION

*Myrtus communis* L. (Myrtaceae) is one of the characteristic representatives of the Mediterranean flora. This species widely found in the Middle East and Mediterranean Region is both naturally grown and cultivated [1]. *Myrtus communis* L. is an evergreen shrub that can grow to 1-5 meters approximately. The oppositely arranged leaves are ovate-lanceolate, 2-5 cm long, coriaceous, glabrous, punctuate-glandular, and entire. The flowering period lasts from June to September. Subglobose to ellipsoid fruits are blue-black (or rarely yellowish-white) when ripe [2]. Different parts of this plant such as fruits, branches, leaves, and seeds have been extensively used in traditional medicine. Traditionally used as an antiseptic, disinfectant, and hypoglycemic agent, its leaves and fruits have been used as an antiseptic drug in villages of Turkey [3]. Similarly, in Italian traditional medicine, the fruit of this plant is used in the treatment of many types of infectious diseases, including diarrhea and dysentery [4]. The leaves are used as an antiseptic and anti-inflammatory agent and as a mouthwash in the treatment of candidiasis [4, 5]. In addition, antibacterial [6], antifungal [7], and antioxidant [8] effects are frequently mentioned in the literature.

Helminthiasis is one of the important parasitic diseases, many of which are zoonotic, especially in developing countries and especially in countries with hot and humid climates. Although not as much as in tropical countries, helminthiasis is quite common in some settlements of Turkey due to insufficient infrastructure and lack of education. Intestinal parasitosis can cause significant manifestations at all levels of the gastrointestinal tract, as well as anemia and growth retardation. Cholecystitis, cholangitis, liver abscess, pancreatitis, ileus, and acute appendicitis are significant complications [9]. In addition, helminth infections are one of the most important causes of growth deficiency and intellectual development retardation in developmental ages [10]. Parasitic diseases cause many problems, especially in children of developmental age, such as malnutrition, developmental retardation, anemia, attention deficit, learning difficulties and consequently decreased success levels. Such health problems observed in primary and secondary education children cause children to lag behind in both physical and psychological development compared to their peers. Studies have mentioned the effects of helminth infections on the school performance of infected children and the future of the country [11]. In addition, it has been reported that these infections may have a detrimental effect on cognition and educational success in terms of intellectual development [11-13]. As a result, people's turn to anthelmintic drugs has also been one of the reasons for the development of resistance [14, 15]. As with many disease agents, the development of resistance to the drug of parasites causes parasitic diseases to be a public health problem and difficulties in their treatment [14, 15]. In recent years, the use of herbal medicines has been increasing exponentially. Many plants are used as a means of treatment for various diseases, and the effects that can replace synthetic drugs are seen. Products obtained from plants have been used since ancient times as a traditional treatment method, especially in the eradication of pathogens that develop drug resistance [16].

Studies on the anthelmintic activities of medicinal plants are very few. One of the reasons is that most of the helminths cannot be cultured in the laboratory environment. Therefore, laboratory animals such as rats or mice are generally preferred as models in such studies. However, animal studies bring many problems such as requiring a lot of labor, shortage of workspace, and being expensive [16]. *Caenorhabditis elegans* (*C. elegans*), Class: Chromadorea, Order: Rhabditida, Family: Rhabditidae, Genus: *Caenorhabditis*, Species: *Caenorhabditis elegans* is a nematode also called threadworm. *C. elegans* can be a good anti-helmintic model, studies have reported [16-18].

In our study, *C. elegans* nematodes were used as an anti-helminthic model and the anti-helminthic effect of *Myrtus communis* L. fruit was determined, and it was aimed to determine the active ingredients with possible anti-helmintic effects by GC-MS analysis.

## MATERIAL AND METHODS

### Plant Material

*The Myrtus communis* L. fruit used in our study was purchased in equal amounts from 10 different vendors sold commercially in Hatay province.

### Preparation of Plant Extracts

*Myrtus communis* L. fruit plant extracts were used in our study. The samples were first washed with tap water and then pure water, then dried on drying paper. Fruits that purchased from different vendors were grounded in equal proportions and homogenized. 100 g was taken from the powdered plant materials. Added 300 mL ethanol on top. It was kept at room temperature in the shaker at 150 rpm for 24 h. At the end of that time, it was filtered twice by the No:1whatman filter payper. Ethanol in the resulting liquid part was completely evaporated in the evaporator (Buchi R-100 equipped with Vacuum Pump V-300 and Control unit I-300).

### GC-MS Analysis

For GC-MS, the HP-5 MS IU capillar column (30 m X 250 μm X 0.25 μm) and the 7890A (Agilent) model GC-MS device with 5975C (Agilent) inert MSD mass detector were used. In GC-MS, an electron ionization system with 70 eV ionization energy and He was used as carrier gas with 99.999% purity. The carrier gas entered the He column with a flow rate of 1.5 mL/min and a starting pressure of 17,897 psi. After keeping the oven temperature at the starting temperature of 50°C for 2 minutes, the rate of temperature rise in all stages was 5°C/min and was increased to 80°C (waiting 2 minutes at this temperature), 100°C (waiting 1 minute at this temperature), 150°C (waiting 1 minute at this temperature), 240°C (waiting 1 minute at this temperature) and 270°C (waiting 7 minutes at this temperature), respectively.

The GC-MS analysis was performed by the Giresun University Central Research Laboratory Application and Research Centre, Giresun, Turkey.

### Anti-helmintic Activity

#### ***Obtaining** C. elegans **Strains***

The strain of wild type *C. elegans* N2 was purchased from the Ceanorhabditis Genetic Center (University of Minnesota, Minneapolis, USA).

#### ***Synchronization of C. elegans nematodes***

About 20 adults *C. elegans* were transferred to the Nematot Growth Media (NGM) petri dish containing E. coli OP50. After laying for 4-6 hours, adults *C. elegans* were removed from the petri dish. These eggs formed synchronized offspring. These were used in the study when it came to adult form at the end of the 3rd day.

This procedure was carried out with 5 petri at the same time to provide sufficient nematodes for the study.

### *Preparation of Nematode Growth Media*

A 2.5 g peptone, 3 g NaCl, and 20 g agar were dissolved in 1 L of distilled water. After autoclaving at 125°C for 15 min, the mixture was cooled to 55°C. Homogenization was obtained by adding 1 mL MgSO4 (1M), 1 mL cholesterol (5 mg/mL), 1 mL CaCl2 (1M), 25 mL KH2PO4 buffer (pH 6), which had been previously prepared and filtered through a 0.2 μm mesh, to the medium. *Myrtus communis* L fruit extracts were added to NGM separately, with final concentrations of 10 mg/mL, 5 mg/mL, 2,5 mg/mL, 1,25 mg/mL and experiment groups were formed. In addition, 10 mL was taken from Kontil (250 mg/5mL), which is used as an antihelmintic drug and whose active ingredient is pyrantel pamoate and dissolved within 100 mL NGM and prepared in a concentration of 5 mg/mL. It formed this positive control group. The negative control group was created only from NGM. NGM was transferred 10 mL each to petri dish and, the prepared *E. coli* OP50 strain was added to NGM.

### *Determination of Anti-helmintic Activity*

In order to determine the anti-helmintic effect of plant extracts on *C. elegans*, 20 synchronized adult *C. elegans* were transferred to NGMs containing plant extracts and *E. coli* OP50. The number of live and dead nematodes was recorded under a stereo microscope every day for 21 days. Each concentration was studied with 5 petri dishes, and the work was repeated 2 times. Nematodes who had completely lost their pharynx pumping movements were considered dead.

### *Statistical analysis*

The data obtained in our study were evaluated in the SPSS (Ver: 22.0) program and the One- Way Anova and Tukey test was used, the level of error was taken as 0.05.

## RESULTS

According to our study results, no adult nematodes were found in the sample of *Myrtus communis* L. fruit extract on the 6th day at all concentrations included in the study. It was found that there are no living nematodes at the end of the second day at the first concentration of the study, 10 mg/mL, at the end of the third day at the concentration of 5 mg/mL, at the end of the fifth day at the concentration of 2.5 mg/mL, and at the end of the 6th day at the concentration of 1.25 mg/mL. According to the data of pyrantel pamoate (5 mg/mL) used as a positive control were examined, the presence of live nematodes was observed until the 10th day. In the negative control group, which was not exposed to any active substance, live nematodes were observed until the 21st day (Fig. 1, Fig. 3, Fig. 4, Table 2). When the data were evaluated statistically, the difference between all experimental groups, negative control group and positive control group (pyrantel pamoate), was significant ($p<0.05$). According to our findings, *Myrtus communis* L. fruit extract was found to be more effective on *C. elegans* nematodes than pyrantel pamoate at the same concentration (5 mg/mL).

The main components determined as a result of GC-MS analysis are shown in Table 1, Figure 2. According to the analysis, the highest detected ingredients were 1,8-Cineole (3.46%), Linalyl acetate (3.06%), and Palmitic acid (2.90%).

## DISCUSSION

In our study, the anti-helmintic activity of *Myrtus communis* L. fruit extract on *C. elegans* nematodes was investigated. Many medicinal effects of *Myrtus communis* L. have been mentioned in the literature [3-7]. In addition, there are studies showing the antiparasitic effect of *Myrtus communis* L. In a study, potent prophylactic effects of essential oils of *Myrtus communis* L. were shown in mice infected with *Toxoplasma gondii*, especially at doses of 200 and 300 mg/kg [19]. Another study was carried out on promastigote and amastigote forms of *Leishmania tropica* and it was shown that the essential oils of *Myrtus communis* L. significantly inhibited their growth

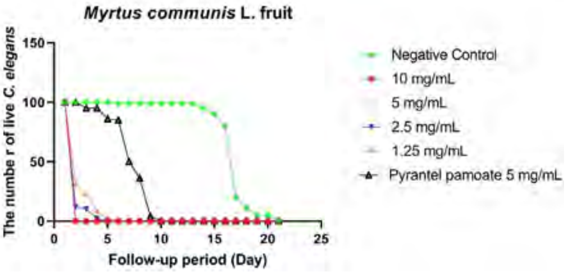

**Figure 1.** Anti-helminthic activity of *Myrtus communis* L. fruit extract on *C. elegans* nematodes

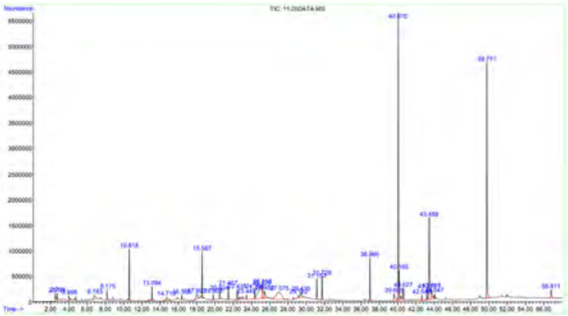

**Figure 2.** GC-MS chromatogram of *Myrtus communis* L. fruit ethanol extract

**Figure 3.** *C. elegans* live nematodes (n: *C. elegans* L4 form, e: egg)

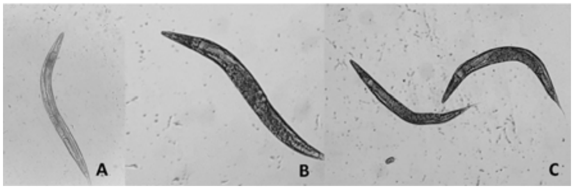

**Figure 4.** *A, B, C Dead nematodes*

**Table 1.** GC-MS results of *Myrtus communis* L. fruit extract

| Bileşen Adı | RT | Ethanol(%) |
|---|---|---|
| Acetic acid | 2.513 | 0.81 |
| 9-Octadecenamide | 2.513 | 0.81 |
| 2-Propenoic acid | 3.995 | 0.45 |
| 2-Heptenal | 8.178 | 0.82 |
| 1,8-Cineole (Eucalyptol) | 10.616 | 3.46 |
| Linalool | 13.093 | 1.37 |
| 4H-Pyran-4-one | 14.713 | 0.78 |
| β-Fenchyl Alcohol | 16.366 | 0.38 |
| 5-Hydroxymethylfurfural | 17.991 | 1.29 |
| Linalyl acetate | 18.586 | 3.06 |
| 2,4-Decadienal | 20.503 | 0.72 |
| Camphene | 21.465 | 0.90 |
| (+)-4-Carene | 21.465 | 0.90 |
| Geranyl acetate | 22.437 | 0.69 |
| trans-Caryophyllene | 23.450 | 0.32 |
| beta-Selinene | 24.360 | 0.77 |
| Palmitic acid | 36.965 | 2.90 |
| 9,12-Octadecadienoic acid | 39.603 | 1.58 |
| Stearic acid | 40.627 | 0.98 |
| D-alpha-Tocopherol | 56.809 | 1.25 |

**Table 2.** Number of live *C. elegans* exposed to different doses of *Myrtus communis* L. fruit ethanol extract

| Days | Control | Pyrantel pamoate 5 mg/mL | 10 mg/mL | 5 mg/mL | 2.5 mg/mL | 1.25 mg/mL |
|---|---|---|---|---|---|---|
| 1 | 100 | 100 | 100 | 100 | 100 | 100 |
| 2 | 100 | 100 | 0 | 1 | 12 | 31 |
| 3 | 100 | 95 | 0 | 0 | 10 | 22 |
| 4 | 100 | 95 | 0 | 0 | 2 | 8 |
| 5 | 100 | 86 | 0 | 0 | 0 | 2 |
| 6 | 99 | 85 | 0 | 0 | 0 | 0 |
| 7 | 99 | 50 | 0 | 0 | 0 | 0 |
| 8 | 99 | 36 | 0 | 0 | 0 | 0 |
| 9 | 99 | 4 | 0 | 0 | 0 | 0 |
| 10 | 99 | 0 | 0 | 0 | 0 | 0 |
| 11 | 99 | 0 | 0 | 0 | 0 | 0 |
| 12 | 99 | 0 | 0 | 0 | 0 | 0 |
| 13 | 99 | 0 | 0 | 0 | 0 | 0 |
| 14 | 95 | 0 | 0 | 0 | 0 | 0 |
| 15 | 90 | 0 | 0 | 0 | 0 | 0 |
| 16 | 80 | 0 | 0 | 0 | 0 | 0 |
| 17 | 20 | 0 | 0 | 0 | 0 | 0 |
| 18 | 11 | 0 | 0 | 0 | 0 | 0 |
| 19 | 5 | 0 | 0 | 0 | 0 | 0 |
| 20 | 5 | 0 | 0 | 0 | 0 | 0 |
| 21 | 0 | 0 | 0 | 0 | 0 | 0 |

in a dose-dependent manner. In a study, The IC50 values of essential oil and methanolic extract were reported as 8.4 and 28.9 μg/mL against promastigotes, and 11.6 and 40.8 μg/mL against amastigote forms, respectively. In addition, it was emphasized in the study that *Myrtus communis* L. was not cytotoxic in the J774 cell line at the working concentrations [20]. In addition to these studies, the anti-parasitic effects of *Myrtus communis* L. on *Giardia lamblia* [21] and *Trichomonas vaginalis* [22,23] protozoa were also mentioned. In the literature review, there were not enough studies on the anti-helmintic activity of *Myrtus communis* L. fruits. In a study, water and ethanol extracts of the leaves of *Myrtus communis* L. investigated for the anti-helminthic activity on cattle strongyles nematodes, and this effect was evaluated by egg screening test and larval mortality test. It was determined that *Myrtus communis* L. leaf water and ethanol extracts have a potential anthelmintic activity on cattle strongyles parasite larvae [24].

As a result of GC-MS analysis, 1,8-Cineole (Eucalyptol), the oxygenated monoterpenes that we detected with the highest rate, were also detected at high rates in the essential oils of *Artemisia lancea* (34.56%), *Piper aduncum* (55.8%), and *Rosmarinus officinalis* (42.11%). It was observed that essential oils of these species show high ovicidal and larvicidal activity on *H. contortus* [25-27].

Compounds such as beta-seline, palmitic acid, 9,12-Octadecadienoic acid, and camphene, which we determined as a result of GC-MS analysis of *Myrtus communis* L. fruit ethanol extract, were found in many plants have anthelmintic effects [28-34].

In a study by Taur et al. [35], the anti-helmintic activity of essential oil isolated from *Eucalyptus globulus* on the adult Indian worms *Pheretima posthuma*, which is anatomically and physiologically similar to human intestinal worm parasites, was investigated. As a result of this study, it was concluded that *E. globulus* oil has anthelmintic potential due to the presence of borneol, linalool, cineol, geranyl acetate, anethole, and saffron. The presence of these herbal components, linalool and geranyl acetate, in the fruit extract of *Myrtus communis* L., was determined as a result of our GC-MS analysis.

The active ingredients in herbal extracts sometimes act alone or sometimes in combination with several active ingredients. There are studies using some of these active ingredient combinations to prove anti-helmintic activity. For example, in a study with fatty acids such as palmitic acid and stearic acid as a result of GC-MS analysis, it was determined that some combinations of palmitic acid and stearic acid prevented the hatch rate of *H. contortus* species by 100%. Likewise, as a result of GC-MS analysis, the highest rate of linalyl acetate (3.06%), which we determined highest than the 1,8-Cineole (3.46%) in the fruit extract of *Myrtus communis* L., was different combinations of α-pinene, p-cymene, thymol octanoate, and thymol acetate compounds were tested on pigs infected with *Ascaris suum* eggs, and the combination of α-pinene, linalyl acetate, p-cymene, and thymol octanoate was found to be quite effective [36].

In a study conducted by Matos-Rocha et al. [37], the schistosomicidal activity of sesquiterpenes such as alpha-humulene and trans-caryophyllene in adult individuals of *Schistosoma* mansoni was evaluated in vitro and it was found that sesquiterpenes at non-lethal concentrations reduce the egg production and motor activity of the worms and cause death in some way depending on the concentration (100 and 200 α/4g/mL). Trans-caryophyllene is one of the ingredient that we detected as a result of GC-MS analysis in our study.

## CONCLUSSIONS

In our study, the anti-helmintic activity of *Myrtus communis* L. fruit extract on *C. elegans* nematodes was investigated, and it was found that *Myrtus communis* L. fruit extract was more effective on *C. elegans* nematodes than pyrantel pamoate at the same concentration (5 mg/mL). According to our GC-MS results of *Myrtus communis* L. fruit extract, 20 different active ingredients were found. In the literature reviews, it has been shown in previous studies that some compounds such as 1,8-Cineole (Eucalyptol), linalool, geranyl acetate, linalyl acetate, and trans-caryophyllene have shown anti-helmintic activity. The presence of these active ingredients supports our experimental results. Via studying the forms of these active ingredients separately or in different combinations, the ingredients and combinations with the strongest anti-helmintic activity can be found, and our findings may pave the way for further studies.

## CONFLICT OF INTEREST

The author declares no financial, or otherwise, conflicts of interest.

## References

1. Traveset A, Riera N, Mas RE. Ecology of fruit-colour polymorphism in Myrtus communis and differential effects of birds and mammals on seed germination and seedling growth. Journal of Ecology (2001) 749-760.
2. Morel J-P, Mercuri AM. Plants and Culture: seeds of the cultural heritage of Europe: Centro Europeo per. I Beni Culturali Ravello Edipuglia (2009) 1-284.
3. Baytop T. Therapy with medicinal plants in Turkey (Past and Present). Publication of the Istanbul University, Istanbul, 1999.
4. Aleksic V, Knezevic P. Antimicrobial and antioxidative activity of extracts and essential oils of Myrtus communis L. Microbiological Research 169 (2014) 240-254.
5. Gortzi O, Lalas S, Chinou I, Tsaknis J. Reevaluation of bioactivity and antioxidant activity of Myrtus communis extract before and after encapsulation in liposomes. European Food Research And Technology 226 (2008) 583-590.
6. El Hartiti H, El Mostaphi A, Barrahi M, Ben Ali A, Chahboun N. Chemical composition and antibacterial activity of the essential oil of Myrtus communis leaves. Karbala International Journal of Modern Science 6 (2020) 249-258.
7. Sadeghi Nejad B, Erfani Nejad M, Yusef Naanaie S, Zarrin M. Antifungal efficacy of Myrtus communis Linn. Jentashapir Journal of Health Research 5 (2014) e21879.
8. Tuberoso CIG., Rosa, A., Bifulco E, Melis MP, Atzeri A, Pirisi FM, & Dessì MA. Chemical composition and antioxidant activities of Myrtus communis L. berries extracts. Food Chemistry 123 (2010) 1242-1251.
9. Gul C, Nazligul Y. A Current Approach to Helminthiasis. Dirim Medical Journal 83 (2008) 40-48.
10. Bethony J, Brooker S, Albonico M, Geiger, SM, Loukas A, Diemert D, & Hotez PJ. Soil-transmitted helminth infections: ascariasis,

trichuriasis, and hookworm. The Lancet 367 (2006) 1521-1532.

11. Drake L, Bundy D. Multiple helminth infections in children: impact and control. Parasitology 122 (2001) 73-81.

12. Gatti S, Lopes R, Cevini C, Ijaoba, B, Bruno A, Bernuzzi AM, Scaglia M. Intestinal parasitic infections in an institution for the mentally retarded. Annals of Tropical Medicine & Parasitology 94 (2000) 453-460.

13. Tappeh KH, Mohammadzadeh H, Rahim RN, Barazesh A, Khashaveh S, Taherkhani H. Prevalence of intestinal parasitic infections among mentally disabled children and adults of Urmia, Iran. Iranian Journal of Parasitology 5 (2010) 60-64.

14. Kaminsky R, Ducray P, Jung M, Clover R, Rufener L, Bouvier J & Mäser P. A new class of anthelmintics effective against drug-resistant nematodes. Nature 452 (2008) 176-181.

15. Smout MJ, Kotze AC, McCarthy JS, Loukas A. A novel high throughput assay for anthelmintic drug screening and resistance diagnosis by real-time monitoring of parasite motility. Plos Neglected Tropical Diseases 4 (2010) e885.

16. Ozpınar N. A model Organism for Antihelminthic Activity: Caenorhabditis elegans and Nigella sativa. Turkish Journal of Parasitology 44 (2020) 31.

17. Hernando G, Turani O, Bouzat C. Caenorhabditis elegans muscle Cys-loop receptors as novel targets of terpenoids with potential anthelmintic activity. Plos Neglected Tropical Diseases 13 (2019) e0007895.

18. Kaewintajuk K, Cho PY, Kim SY, Lee ES, Lee HK, Choi EB, & Park, H. Anthelmintic activity of KSI-4088 against Caenorhabditis elegans. Parasitology Research 107 (2010) 27-30.

19. Shaapan RM, Al-Abodi HR, Alanazi AD, Abdel-Shafy S, Rashidipour M, Shater AF, & Mahmoudvand H. Myrtus communis Essential Oil; Anti-Parasitic Effects and Induction of the Innate Immune System in Mice with Toxoplasma gondii Infection. Molecules 26 (2021) 819.

20. Mahmoudvand H, Ezzatkhah F, Sharififar F, Sharifi I, Dezaki ES. Antileishmanial and cytotoxic effects of essential oil and methanolic extract of Myrtus communis L. The Korean Journal of Parasitology 53 (2015) 21-27.

21. Abdalla SF, Ramadan NI, Mohamed AA, El-Deeb HK, Al-Khadrawy FM, Badawy AF. A study on the effect of Myrtus communis and Olibanum on Giardia lamblia infection in Egypt. Parasitologists United Journal 4 (2011) 89-100.

22. Azadbakht M, Ziaiye H, Abdollahi F, Shabankhani B. Effect of Methanolic essence and extract of Myrtus communis on Trichomonas vaginalis. Journal of Guilan University of Medical Sciences 12 (2004) 8-13.

23. Abdollahy F, Ziaei H, Shabankhani B, Azadbakht M. Effect of essential oils of Artemisia aucheri Boiss. Zataria multiflora Boiss, and Myrtus communis L. on Trichomonas vaginalis. Iranian Journal of Pharmaceutical Research (2010) 35.

24. Moussouni L, Besseboua O, Abdelhanine A. Anthelmintic activity of aqueous and ethanol extracts of Urtica dioica L. and Myrtus communis L. leaves on bovine digestive strongyles: in-vitro study. Ataturk University Journal of Veterinary Sciences 14 (2019) 273-283.

25. Vickers NJ. Animal communication: when I'm calling you, will you answer too? Current Biology 27 (2017) 713-715.

26. Oliveira GL, Vieira TM, Nunes VF, Ruas MDO, Duarte ER, Moreira DDL, & Martins ER. Chemical composition and efficacy in the egg-hatching inhibition of essential oil of Piper aduncum against Haemonchus contortus from sheep. Revista Brasileira de Farmacognosia 24 (2014) 288-292.

27. Pinto, N. B., Castro, L. M. D., Azambuja, R. H. M., Capella, G. D. A., Moura, M. Q. D., Terto, W. D., ... & Leite, F. P. L. Ovicidal and larvicidal potential of Rosmarinus officinalis to control gastrointestinal nematodes of sheep. Revista Brasileira de Parasitologia Veterinária 28 (2019) 807-811.

28. Pessoa L, Morais S, Bevilaqua C, Luciano J. Anthelmintic activity of essential oil of Ocimum gratissimum Linn. and eugenol against Haemonchus contortus. Veterinary Parasitology 109 (2002) 59-63.

29. Malheiros DF, Sarquis IR, Ferreira IM, Mathews PD, Mertins O, Tavares-Dias M. Nanoemulsions with oleoresin of Copaifera reticulata (Leguminosae) improve anthelmintic efficacy in the control of monogenean parasites when compared to oleoresin without nanoformulation. Journal of Fish Diseases 43 (2020) 687-695.

30. Lalthanpuii PB, Lalchhandama K. Phytochemical analysis and in vitro anthelmintic activity of Imperata cylindrica underground parts. BMC Complementary Medicine and Therapies 20 (2020) 1-9.

31. Lalthanpuii P, Zokimi Z, Lalchhandama K. The toothache plant (Acmella oleracea) exhibits anthelmintic activity on both parasitic tapeworms and roundworms. Pharmacognosy Magazine 16 (2020) 193-198.

32. Hernandez PM, Salem AZ, Elghandour MM, Cipriano-Salazar M, Cruz-Lagunas B, Camacho LM. Anthelmintic effects of Salix babylonica L. and Leucaena leucocephala Lam. extracts in growing lambs. Tropical Animal Health and Production 46 (2014) 173-178.

33. Panda SK, Das R, Mai AH, De Borggraeve WM, Luyten W. Nematicidal Activity of Holigarna caustica (Dennst.) Oken Fruit Is Due to Linoleic Acid. Biomolecules 10 (2020) 1043-1054.

34. Štrbac F, Bosco A, Amadesi A, Rinaldi L, Stojanović D, Simin N, Orčić D, Pušić I, Krnjajić S, Ratajac R. In vitro ovicidal activity of two chemotypes of the yarrow (Achillea millefolium L.) essential oil against sheep gastrointestinal nematodes. Archives of Veterinary Medicine 13 (2020) 59-76.

35. Taur D, Kulkarni V, Patil R. Chromatographic evaluation and anthelmintic activity of Eucalyptus globulus oil. Pharmacognosy Research 2 (2010) 125-127.

36. Kaplan RM, Storey BE, Vidyashankar AN, Bissinger BW, Mitchell SM, Howell SB, Mason ME, Lee MD, Pedroso AA, Akashe A, Skrypec DJ. Antiparasitic efficacy of a novel plant-based functional food using an Ascaris suum model in pigs. Acta Tropica 139 (2014) 15-22.

37. Matos-Rocha TJ, dos Santos Cavalcanti MG, Barbosa-Filho JM, et al. In vitro evaluation of schistosomicidal activity of essential oil of Mentha x villosa and some of its chemical constituents in adult worms of Schistosoma mansoni. Planta Medica. 79 (2013) 1307-1312.

Hittite Journal of Science and Engineering, 2021, 8 (3) 273–277
ISSN NUMBER: 2148–4171
DOI: 10.17350/HJSE19030000239

# Protection of copper from corrosion with nicotinamide inhibitor

**Gulden Asan**
Hitit University, Department of Occupational Health and Safety, Corum, Turkey

***Article History:***
*Received: 2021/08/21*
*Accepted: 2021/09/27*
*Online: 2021/09/29*

***Correspondence to****: Gulden Asan, Hitit University, Vocational School of Technical Sciences, Occupational Health and Safety Program, Corum/Turkey*
*E-Mail: guldenasan@hitit.edu.tr Phone: +90 (507) 923 8341*
*Fax:*

## ABSTRACT

Copper is used extensively in industry since its superior metallic properties. Since the corrosion resistance of copper is low in acidic media, it is important to apply corrosion prevent methods. In this study, the environmentally friendly nicotinamide compound was used as an inhibitor to protect copper from corrosion. In this study, firstly, the Cyclic Voltammetry Technique was used to determine the electrochemical behavior of copper in 0.1 M HCl acid solution. Then, Tafel polarization method was applied to determine the corrosion behavior of copper in 0.1 M HCl acid solution in the absence of nicotinamide inhibitor and in the presence of 500 ppm, 750 ppm, 1000 ppm nicotinamide. The optimum time was determined for each concentration by keeping the inhibitor at these 3 different concentrations for 0, 15, 30, 45 and 60 minutes. The highest inhibition efficiency was obtained as 95.3% in 1000 ppm nicotinamide concentration in 30 minutes residence time, and the best corrosion potential was -0.145 V in 1000 ppm nicotinamide concentration in 45 minutes residence time. 750 ppm inhibitor concentration can be used in cases where the duration is not important, as the inhibition efficiency value is reached as 94.6% in a 60 minutes residence time at a 750 ppm nicotinamide concentration.

**Keywords:**
Copper; Corrosion; Tafel Polarization; Nicotinamide; Inhibitor

## INTRODUCTION

Copper is one of the first minerals to be mined and processed in human history. Although gold first attracted the attention of human beings, copper has been widely used by human beings because it can be found in every part of the world and can be easily processed. B.C. Bronze is a copper-tin alloy that gives its name to the period between 3000-1800 (Bronze Age). Copper has found a wide range of uses because it is the metal that conducts electricity the best after silver and makes alloys of industrial importance. Depending on the economic development, the usage areas of copper are increasing day by day. It is so important to protect such an important metal from corrosion [1]. Corrosion causes billions of dollars in economic loss, terrible safety hazards and environmental pollution each year [2,3]. While copper has high corrosion resistance in neutral and slightly alkaline media, it is not resistant to corrosion in acidic media [4,5]. Acid solutions are widely used in industry. These solutions are generally corrosive. Therefore, inhibitors are widely used to reduce the corrosive effect on metallic material [6]. Different methods such as suitable design, use of alloys, changing the media, surface coatings and use of inhibitors are used to protect metals from corrosion [7]. We can classify the applied methods as electrochemical methods, chemical methods and surface coating. Electrochemical methods; can be counted as cathodic protection and anodic protection. The use of inhibitor applied in this study is a corrosion protection method applied in chemical methods [8]. We can divide the inhibitors used in corrosion protection as inorganic inhibitors and organic inhibitors. Inhibitors generally adsorb to the surface to form a protective film on the metal surface, thus providing protection against corrosion [9,10]. In organic inhibitors; Heteroatoms such as nitrogen, sulphur and phosphorus increase the corrosion inhibitory effectiveness [11,12]. The electron donating atoms of heteroatoms such as nitrogen, sulfur and phosphorus in the organic compound and the d orbitals on the copper atom form coordinated bonds and work as corrosion inhibitors for copper [13,14]. When the use of inhibitors in corrosion protection finds application, the aim is more effective protection, but today, only corrosion protection is not sufficient. Because many of the inhibitors are expensive and threaten the environment and human health with their toxic effects [15]. Today, an environment-friendly inhibitor called green inhibitor has been investigated [16,17]. The nicotinamide used in this study is vitamin B3. For this reason, nicotinamide inhibitor is an environmentally friendly chemical that is not harmful to human health and even beneficial [18,19]. This situation increases the importance of the study. Our previous study also proved that nicotinamide is an effective inhibitor in protecting aluminum from corrosion [20]. In this study, the inhibition efficiency of nicotinamide on copper corrosion in acidic medium was investigated.

## MATERIAL AND METHODS

In the experiments, corrosion resistance of copper in 0.1 M HCl acid medium and after the addition of nicotinamide at different concentrations was measured with the Ivium Technologies De Regent 178 5611 HW Eindhoven model device using Cyclic Voltammetry Method and Tafel Polarization Method. As it is known, corrosion occurs when two electrochemical reactions between the metal and the solution medium come into equilibrium. One of these reactions is the anodic reaction and is formed by the dissolution of the metal. The other reaction is the cathodic reaction that occurs with the reduction of $O_2$ or $H^+$ in the solution. In the Tafel Polarization Method, anodic and cathodic Tafel curves are obtained for the corroded metal, and the linear parts of them are extended and the corrosion rate ($I_{cor}$) and corrosion potential ($E_{cor}$) for that system are found from the cut points. Measurements were carried out in a three-necked corrosion cell. A copper electrode embedded in polyester resin and a surface area of 1 $cm^2$ was used as the working electrode, a Pt plate as the counter electrode, and a saturated calomel electrode placed in the lugin as the reference electrode. Before each measurement, the surface of the working electrode was cleaned with 4000 grit sandpaper. Then it was made ready for use by passing through pure water and ethyl alcohol. The acid solution was prepared using Merck brand 37% Hydrochloric Acid solution and distilled water. As an inhibitor, Nicotinamide (Sigma Aldrich) was added to the solution at different concentrations and measurements were taken. The molecular structure of nicotinamide is shown in Figure 1.

## RESULTS AND DISCUSSION

To determine the electrochemical behavior of copper in 0.1 M HCl acid solution, cycling voltammograms were taken between -1.0 V and +0.2 V at a scanning rate of 200 mV/s. With cyclic voltammetry, information about reduction/oxidation events on the electrode surface, whether it is reversible, diffusion or adsorption can be obtained [21,22]. Figure 2 shows the CV of copper in 0.1 M hydrochloric acid solution. In the forward potential scanning, anodic current started to pass after –0.5 V and there was no increase in this current until -0.1 V. That is, the metal is in a passive state. However, after this potential, copper is oxidized by giving electrons. By reverse polarization the reduction peak of the oxidized copper is seen after -0.12 V.

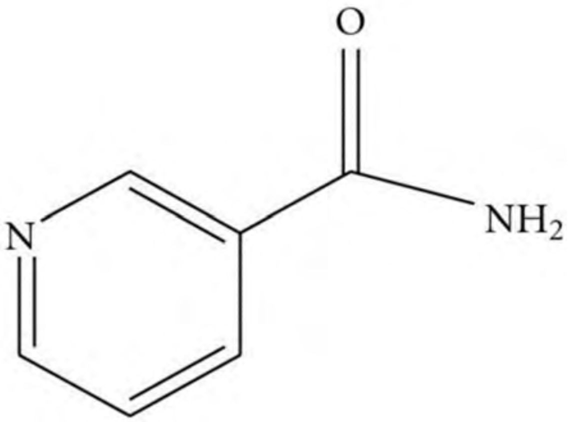

**Figure 1.** Molecular structure of Nicotinamide.

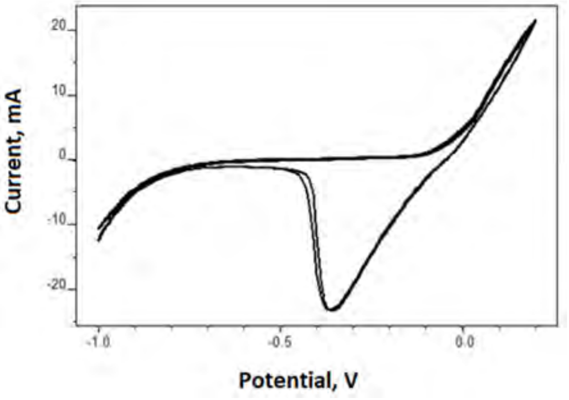

**Figure 2.** Electrochemical behavior of copper in 0.1 M Hydrochloric acid solution

The addition of an organic corrosion inhibitor provides a protective layer that prevents corrosion on the copper surface by adsorption of inhibitor molecules in a corrosive media [23]. Nicotinamide, used as an inhibitor, was first added to the solution at 500 ppm, and the Tafel polarization curve was taken without waiting, and this was called 0 minute measurement. Then, Tafel polarization curves of the copper electrode were taken after waiting for 15, 30, 45 and 60 minutes in order to see the effect of the holding time on the inhibition efficiency. A decrease in the corrosion rate is expected with increasing the holding time of the electrode in the solution containing the inhibitor [24]. It is expected that the corrosion rate will decrease, that is, an increase in the inhibitor's effectiveness, since the inhibitor has been given the opportunity to adhere to the surface by increasing the holding time. These measured values are given in Table 1.

Tafel polarization curves taken at different residence

**Table 1.** Effect of Residence Time on Copper Corrosion in 0.1 M HCl Solution Containing 500 ppm Nicotinamide

| Concentration, ppm | Residence time, minutes | $E_{cor}$, V | $I_{cor}$, (µA) | Corrosion Rate, mm/y | Inhibition Efficiency % |
|---|---|---|---|---|---|
| 0 | 0 | -0.403 | 12.74 | 0.148 | --- |
| 500 | 0 | -0.351 | 2.72 | 0.032 | 78.7 |
| | 15 | -0.327 | 1.69 | 0.020 | 86.8 |
| | 30 | -0.258 | 1.59 | 0.018 | 87.5 |
| | 45 | -0.181 | 1.28 | 0.015 | 90.0 |
| | 60 | -0.189 | 1.02 | **0.012** | **92.0** |

times were superimposed and given in Figure 3. As can be seen from the Figure 3 and the Table 1, the corrosion potential shifted to positive values when the residence time of the copper electrode increased in the media included nicotinamide. This is desirable situation and this demonstrates that copper resists corrosion up to a higher potential [25]. Table 1 shows that although the best corrosion potential seems to have been obtained in 45 minutes of residence time, almost the same potential curves were observed in 60 minutes and in 45 minutes of residence time. The minimum corrosion rate and the inhibition efficiency was determined respectively 0.01183 mm/year and 92.0% in the 60 minutes residence time.

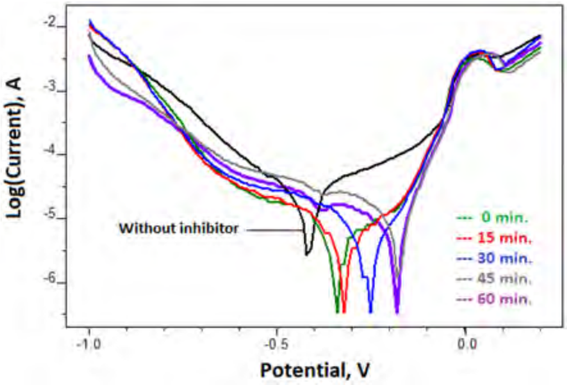

**Figure 3.** Tafel Polarization curves obtained for Copper at different residence times in 0.1 M HCl solution containing 500 ppm nicotinamide

In order to investigate the effect of nicotinamide concentration on copper corrosion, after 500 ppm nicotinamide was added, 750 ppm and 1000 ppm nicotinamide were added to 0.1 M HCl solution. Then, the determination of the optimum residence time was made at all concentrations. It is seen at Table 2 and Figure 4, the best corrosion potential and the lowest corrosion rate were obtained in 60 minutes holding. An increase in inhibition efficiency was observed compared to 500 ppm nicotinamide.

**Table 2.** Effect of Residence Time on Copper Corrosion in 0.1 M HCl Solution Containing 750 ppm Nicotinamide

| Concentration, ppm | Residence time, minutes | $E_{cor}$, V | $I_{cor}$, (µA) | Corrosion Rate, mm/y | Inhibition Efficiency % |
|---|---|---|---|---|---|
| 0 | 0 | -0.403 | 12.74 | 0.148 | --- |
| 750 | 0 | -0.332 | 1.77 | 0.021 | 86.1 |
| | 15 | -0.286 | 1.22 | 0.014 | 90.4 |
| | 30 | -0.221 | 0.96 | 0.011 | 92.6 |
| | 45 | -0.206 | 0.88 | 0.010 | 93.1 |
| | 60 | -0.180 | 0.69 | **0.008** | **94.6** |

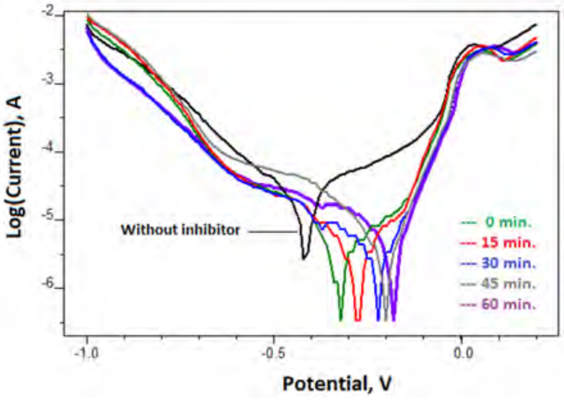

**Figure 4.** Tafel Polarization curves obtained for Copper at different residence times in 0.1 M HCl solution containing 750 ppm nicotinamide

Since the inhibition efficiency increased with the increase in the nicotinamide concentration from 500 ppm to 750 ppm, the optimum time was determined by adding 1000 ppm nicotinamide to the 0.1 M HCl solution. Table 3 and Figure 5 show that the best corrosion potential and the lowest corrosion rate were obtained in 30 minutes of waiting. The lowest corrosion rate was 0.007 mm/year and the inhibition efficiency was 95.3% in the 30 minutes residence time. A temporal advantage was achieved as the lowest corrosion rate was reached in 30 minutes.

**Table 3.** Effect of Residence Time on Copper Corrosion in 0.1 M HCl Solution Containing 1000 ppm Nicotinamide

| Concentration, ppm | Residence time, minutes | $E_{cor}$, V | $I_{cor}$, (µA) | Corrosion Rate, mm/y | Inhibition Efficiency % |
|---|---|---|---|---|---|
| 0 | 0 | -0.403 | 12.74 | 0.148 | --- |
| 1000 | 0 | -0.237 | 1.33 | 0.015 | 89.9 |
| | 15 | -0.188 | 1.05 | 0.012 | 91.9 |
| | 30 | -0.168 | 0.58 | **0.007** | **95.3** |
| | 45 | -0.145 | 0.93 | 0.011 | 92.6 |
| | 60 | -0.157 | 1.57 | 0.018 | 87.8 |

## CONCLUSION

As a result, nicotinamide proved to be an effective inhibitor in protecting copper from corrosion. Figure 6 shows that the corrosion potential after 60 minutes of waiting at 500 ppm nicotinamide concentration is -0.189 V, and

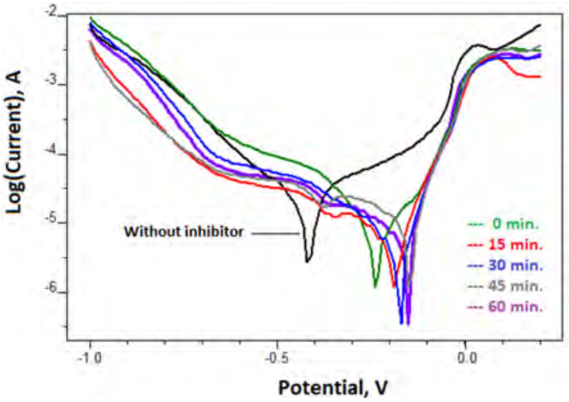

**Figure 5.** Tafel Polarization curves obtained for Copper at different residence times in 0.1 M HCl solution containing 1000 ppm nicotinamide

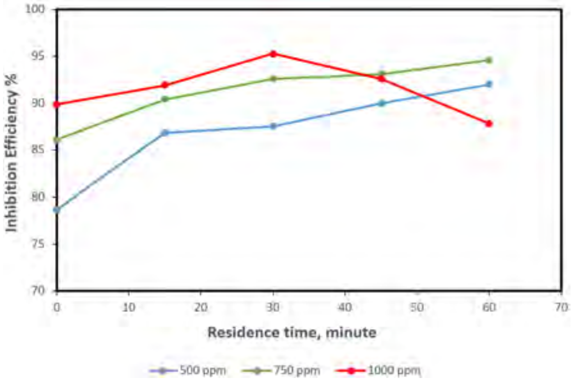

**Figure 6.** Tafel Polarization curves obtained for Copper at different residence times in 0.1 M HCl solution containing different concentration (500 ppm, 750 ppm and 1000 ppm) nicotinamide

the inhibition efficiency is 92.0%. After 60 minutes of soaking at 750 ppm nicotinamide concentration, the corrosion potential increased to -0.180 V and the inhibition efficiency increased to 94.6%. This showed us that the adsorption to the surface is not sufficient at 500 ppm concentration, but when the concentration is increased to 750 ppm, the inhibition efficiency increases with the increase in surface adhesion. When the concentration increased to 1000 ppm, the lowest corrosion rate was reached in 30 minutes and thus the residence time was halved. Inhibition efficiency of 95.3% was obtained at 1000 ppm nicotinamide concentration in 30 minutes residence time. At 1000 ppm nicotinamide concentration, a decrease in inhibition efficiency was observed when the 30 minutes residence time was exceeded. When the concentration was increased more than the molecules to be adsorbed, that is, if there were more inhibitor molecules in the media, the corrosion rate was negatively affected. It can be thought that when the protective layer becomes thicker in adsorption, permeability may increase by forming defects on the surface, which leads to a decrease in corrosion resistance. The corrosion potential shifted to more positive values at all three concentrations, thus providing an advantage in corrosion protection. It is advantageous to use 750 ppm nicotinamide concentration when there is no time restriction, and to use 1000 ppm nicotinamide concentration when it is desired to provide faster protection. Nicotinamide has proven that it can be used safely in the protection of copper from corrosion due to its environmental friendliness and high corrosion inhibitory effectiveness.

## CONFLICT OF INTEREST

Author approve that to the best of their knowledge, there is not any conflict of interest or common interest with an institution/organization or a person that may affect the the review process of the paper.

## References

1. A. Fateh, M. Aliofkhazraei, A.R. Rezvanian, Review of corrosive environments for copper and its corrosion inhibitors, Arabian Journal of Chemistry. 13 (2020) 481–544. https://doi.org/10.1016/j.arabjc.2017.05.021.
2. R. Javaherdashti, How corrosion affects industry and life, Anti-Corrosion Methods and Materials. 47 (2000) 30–34. https://doi.org/10.1108/00035590010310003.
3. X.F. Zhang, Y.Q. Chen, J.M. Hu, Robust superhydrophobic SiO2/polydimethylsiloxane films coated on mild steel for corrosion protection, Corrosion Science. 166 (2020). https://doi.org/10.1016/j.corsci.2020.108452.
4. G. Tansuğ, T. Tüken, E.S. Giray, G. Findikkiran, G. Siğircik, O. Demirkol, M. Erbil, A new corrosion inhibitor for copper protection, Corrosion Science. 84 (2014) 21–29. https://doi.org/10.1016/j.corsci.2014.03.004.
5. G. Moretti, F. Guidi, Tryptophan as copper corrosion inhibitor in 0.5 M aerated sulfuric acid, Corrosion Science. 44 (2002) 1995–2011. https://doi.org/10.1016/S0010-938X(02)00020-3.
6. Q.B. Zhang, Y.X. Hua, Corrosion inhibition of mild steel by alkylimidazolium ionic liquids in hydrochloric acid, Electrochimica Acta. 54 (2009) 1881–1887. https://doi.org/10.1016/j.electacta.2008.10.025.
7. R. Natarajan, F.S. Zahir Said Al Shibli, Synthesis of biomass derived product from Ziziphus spina-christi and application for surface protection of metal under acidic environment- Performance evaluation and thermodynamic studies, Chemosphere. 284 (2021) 131375. https://doi.org/10.1016/j.chemosphere.2021.131375.
8. J.M. Gaidis, Chemistry of corrosion inhibitors, Cement and Concrete Composites. 26 (2004) 181–189. https://doi.org/10.1016/S0958-9465(03)00037-4.
9. C.N. Hippolyte, B.Y. Serge, A. Sagne, J. Creus, T. Albert, Nicotinamide Inhibition Properties for Copper Corrosion in 3.5% NaCl Solution: Experimental and Theorical Investigations, Journal of Materials Science and Chemical Engineering. 06 (2018) 100–121. https://doi.org/10.4236/msce.2018.63008.
10. H. Gerengi, H.I. Ugras, M.M. Solomon, S.A. Umoren, M. Kurtay, N. Atar, Synergistic corrosion inhibition effect of 1-ethyl-1-methylpyrrolidinium tetrafluoroborate and iodide ions for low carbon steel in HCl solution, Journal of Adhesion Science and Technology. 30 (2016) 2383–2403. https://doi.org/10.1080/01694243.2016.1183407.
11. A. Asan, M. Kabasakaloğlu, M. Işiklan, Z. Kiliç, Corrosion inhibition of brass in presence of terdentate ligands in chloride solution, Corrosion Science. 47 (2005). https://doi.org/10.1016/j.

corsci.2004.07.031.

12. R. Natarajan, F. Al Shibli, Corrosion inhibition of aluminum under basic conditions using Medicago sativa L. extract — thermodynamic studies, Korean Journal of Chemical Engineering. 38 (2021) 1–10. https://doi.org/10.1007/s11814-021-0851-z.
13. M.M. Antonijevic, M.B. Petrovic Mihajlovic, Copper Corrosion Inhibitors. Period 2008-2014. A Review, International Journal of Electrochemical Science. 10 (2015) 1027–1053. http://electrochemsci.org/papers/vol10/100201027.pdf.
14. B. Tan, S. Zhang, Y. Qiang, W. Li, H. Li, L. Feng, L. Guo, C. Xu, S. Chen, G. Zhang, Experimental and theoretical studies on the inhibition properties of three diphenyl disulfide derivatives on copper corrosion in acid medium, Journal of Molecular Liquids. 298 (2020) 111975. https://doi.org/10.1016/j.molliq.2019.111975.
15. M. Bethencourt, F.J. Botana, J.J. Calvino, M. Marcos, M.A. Rodríguez-Chacón, Lanthanide compounds as environmentally-friendly corrosion inhibitors of aluminium alloys: A review, Corrosion Science. 40 (1998) 1803–1819. https://doi.org/10.1016/S0010-938X(98)00077-8.
16. P.B. Raja, M.G. Sethuraman, Natural products as corrosion inhibitor for metals in corrosive media - A review, Materials Letters. 62 (2008) 113–116. https://doi.org/10.1016/j.matlet.2007.04.079.
17. P. Mourya, S. Banerjee, M.M. Singh, Corrosion inhibition of mild steel in acidic solution by Tagetes erecta (Marigold flower) extract as a green inhibitor, Corrosion Science. 85 (2014) 352–363. https://doi.org/10.1016/j.corsci.2014.04.036.
18. S. Bashir, V. Sharma, S. Kumar, Z. Ghelichkhah, I.B. Obot, A. Kumar, Inhibition performances of nicotinamide against aluminum corrosion in an acidic medium, Portugaliae Electrochimica Acta. 38 (2020) 107–123. https://doi.org/10.4152/pea.202002107.
19. X. Liu, X. Pan, M. Lu, Y. Sun, Z. Wang, Y. Zheng, Nicotinic acid derivatives as corrosion inhibitors for mild steel in hydrochloric acid solutions: an experimental and computational chemistry study, Journal of Adhesion Science and Technology. 35 (2021) 63–80. https://doi.org/10.1080/01694243.2020.1787934.
20. G. Asan, A. Asan, H. Çelikkan, The effect of 2D-MoS2 doped polypyrrole coatings on brass corrosion, Journal of Molecular Structure. 1203 (2020). https://doi.org/10.1016/j.molstruc.2019.127318.
21. M. Okutan, Electrochemical determination of ascorbic acid with thermally reduced graphene oxide, Journal of the Faculty of Engineering and Architecture of Gazi University. 35 (2020) 1589–1601. https://doi.org/10.17341/gazimmfd.645284.
22. T.T. Calam, Investigation of the electrochemical behavior of phenol using 1H-1, 2, 4-triazole-3-thiol modified gold electrode and its voltammetric determination, Journal of the Faculty of Engineering and Architecture of Gazi University. 35 (2020) 835–844. https://doi.org/10.17341/gazimmfd.543608.
23. R. Ravichandran, N. Rajendran, Electrochemical behaviour of brass in artificial seawater: Effect of organic inhibitors, Applied Surface Science. 241 (2005) 449–458. https://doi.org/10.1016/j.apsusc.2004.07.046.
24. G. Moretti, F. Guidi, G. Grion, Tryptamine as a green iron corrosion inhibitor in 0.5 M deaerated sulphuric acid, Corrosion Science. 46 (2004) 387–403. https://doi.org/10.1016/S0010-938X(03)00150-1.
25. T. Ohtsuka, Corrosion protection of steels by conducting polymer coating, International Journal of Corrosion. 2012 (2012). https://doi.org/10.1155/2012/915090.